NMR STUDIES OF ADVANCED THERMOELECTRIC MATERIALS AND TOPOLOGICAL CHALCOGENIDES

A Dissertation

by

YEFAN TIAN

Submitted to the Office of Graduate and Professional Studies of
Texas A&M University
in partial fulfillment of the requirements for the degree of

DOCTOR OF PHILOSOPHY

Chair of Committee,	Joseph H. Ross, Jr.
Committee Members,	Donald G. Naugle
	Valery Pokrovsky
	Patrick Shamberger
Head of Department,	Grigory Rogachev

May 2021

Major Subject: Physics

ABSTRACT

In this dissertation, NMR techniques combined with various experimental and computational techniques were applied to investigate materials systems including advanced thermoelectric materials and topological chalcogenides. Among thermoelectric materials, substituted half-Heuslers $Nb_{1-x}Ti_xFeSb$ ($0 \leq x \leq 0.3$), pure half-Heuslers NbCoSn, ZrCoSb and TaFeSb, as well as $CoSb_3$-based skutterudites are studied. Magnetic measurements, combined with an observed Schottky anomaly and changes in the NMR line width indicate the presence of a 0.2% concentrated native magnetic defect in stoichiometric NbFeSb samples. To further understand this system, I have done NMR and Mössbauer studies combined with DFT calculations of $Nb_{1-x}Ti_xFeSb$ ($0 \leq x \leq 0.3$). These studies provide local information about defects and electronic configurations in these heavily *p*-type materials. I also investigated ^{59}Co, ^{93}Nb, and ^{121}Sb NMR spectroscopy on an additional series of half-Heusler semiconductors, including NbCoSn, ZrCoSb, TaFeSb and NbFeSb, to better understand their electronic properties and general composition-dependent trends. Significant results of these studies include evidence for non-conductive states in more heavily substituted compositions, and for an enhancement of the orbital susceptibility connected with electron-electron interactions. I have additionally applied ^{59}Co NMR and transport measurements to probe the electronic behavior of *n*-type filled skutterudites $Ba_xYb_yCo_4Sb_{12}$ and $A_xCo_4Sb_{12}$ (A = Ba, Sr). The results demonstrate consistently that a shallow defect level near the conduction band minimum dominates the electronic behavior, in contrast to the behavior of unfilled $CoSb_3$.

Studies of the topological chalcogenides $ZrTe_5$ and $ZrTe_2$ are also described here. NMR and magnetic measurements can reveal the magnetic properties of the defects states in the samples. NMR is specialized to provide information of band structure close to Fermi level, which gives a better understanding of electronic structures of materials. For topological materials included here, NMR is also able to detect the Dirac Fermions and then show interesting topological features of them. I carried out ^{125}Te NMR measurements of the topological quantum material $ZrTe_5$. Spin-lattice relaxation results, well-explained by a theoretical model of Dirac electron systems,

reveal that the topological characteristic of $ZrTe_5$ is T-dependent, changing from weak topological insulator to strong topological insulator as temperature increases. Finally, NMR studies of the transition metal dichalcogenide $ZrTe_2$ were completed. The measured NMR shift anisotropy reveals a quasi-2D behavior connected to a topological nodal line close to the Fermi level.

DEDICATION

To my parents

who love and support me all the time.

ACKNOWLEDGMENTS

First, I would like to express my sincere gratitude to my advisor Dr. Joseph H. Ross, Jr., for all his support, encouragement and patience during these years. I enjoyed all the work and discussions we had during my graduate study. I'd like to thank all my colleagues in Dr. Ross's group: Dr. Ali A. Sirusi, Laziz Saribaev, Dr. Nader Ghassemi, Emily Conant, and Rui Li. It was a great pleasure to work with all of them and I really appreciate all their help and suggestions.

Many thanks to the members of my committee member Dr. Donald G. Naugle, Dr. Valery Pokrovsky, and Dr. Patrick Shamberger for their time and suggestions. I would like to thank all the collaborators of my projects from University of Houston, University of Michigan, Pennsylvania State University, Turkey and Japan. Besides the Ph.D. program of physics, I have also joined D^3EM program and worked with a great cohort of colleagues. I want to thank Dr. Raymundo Arróyave D^3EM, the PI of D^3EM and Dr. Yuhao Wang, my teammate of D^3EM project. We have worked together on materials design project over a year and successfully published the work.

Very special recognition to all my friends in both U.S. and China for all the encouragement and support through all these years, especially Dr. Yuhao Wang and Dr. Yu Liu. All of they made these several years more meaningful and enjoyable. Last but not least, I am grateful to all my family for their love and selfless support.

CONTRIBUTORS AND FUNDING SOURCES

Contributors

This work was supported by a dissertation committee consisting of Professors Joseph H. Ross, Jr. [advisor], Donald G. Naugle and Valery Pokrovsky of the Department of Physics and Astronomy and Professor Patrick Shamberger of the Department of Materials Science and Engineering.

The half-Heuslers in Chapters 4-6 were prepared by Professor Zhifeng Ren's group at University of Houston. Mössbauer measurements in Chapter 5 were done by Dr. Farit G. Vagizov at Kazan Federal University, Russia. The skutterudites in Chapter 7 were prepared by Professor Ctirad Uher's group at University of Michigan. Skutterudites data in Chapter 7 were partially measured by my former labmate Dr. Ali A. Sirusi at TAMU. All DFT calculations were conducted by my former labmate Dr. Nader Ghassemi at TAMU. All magnetic, XRD and MAS measurements were performed using external user facilities.

All other work conducted for the dissertation was completed by myself independently.

Funding Sources

Graduate study was supported by the Robert A. Welch foundation, the College of Science Strategic Transformative Research Program at Texas A&M University, the Department of Physics and Astronomy of Texas A&M University.

NOMENCLATURE

NMR	Nuclear Magnetic Resonance
STI	Strong Topological Insulator
WTI	Weak Topological Insulator
DFT	Density Functional Theory
RF	Radio Frequency
MAS	Magic-Angle Spinning
EFG	Electric Field Gradient
FWHM	Full Width at Half Maximum
VB	Valence Band
CB	Conduction Band
DOS	Density of States
K	Knight Shift
σ	Chemical Shift
CVT	Chemical Vapor Transport
T_1	Spin-lattice Relaxation Rate
S	Seebeck Coefficient
zT	Thermoelectric Figure of Merit
TMDC	Transition Metal Dichalcogenide
SQUID	Superconducting Quantum Interference Device
XRD	X-ray Powder Diffraction
C	Specific Heat
H_{HF}	Hyperfine Field

EPMA	Electron Probe Microanalysis
μ	Chemical Potential

TABLE OF CONTENTS

Page

LIST OF FIGURES

FIGURE Page

LIST OF TABLES

TABLE Page

1. INTRODUCTION AND LITERATURE REVIEW

1.1 Advanced Thermoelectric Materials

In 1823, the German physicist Thomas J. Seebeck discovered in experiments that there is a voltage drop between the ends of a sample with a high temperature gradient. This effect became the theoretical foundation of the design of thermocouples to directly convert heat energy to electrical energy, which is called the Seebeck effect. When an electric current is passed through a circuit of a thermocouple, heat is evolved at one junction and absorbed at the other junction. This effect is called the thermoelectric cooling effect or Peltier effect, named after French physicist Jean Charles Athanase Peltier, who discovered it in 1834, which is a reverse effect of the Seebeck effect.

The Seebeck effect is the build up of an electric potential across a temperature gradient, which is a classic example of an electromotive force (EMF). In general, the Seebeck effect is described locally by the creation of an electromotive field

$$\mathbf{E}_{\text{emf}} = -S\nabla T, \tag{1.1}$$

where S is the Seebeck coefficient and ∇T is the temperature gradient. If the system reaches a steady state, where $\mathbf{J} = 0$ (the ohmic current compensates the thermoelectric current), then the voltage gradient is given simply by the EMF: $\nabla V = S\nabla T$. The Peltier effect can be considered as the back-action counterpart to the Seebeck effect. The close relationship between Peltier and Seebeck effects can be seen in the direct connection between their coefficients $\Pi = TS$.

The use of materials with a high Seebeck coefficient is one of many important factors for the efficient behavior of thermoelectric generators and thermoelectric coolers. Fig. 1.1 shows both thermoelectric generator and cooler. Based on the Seebeck coefficient, the usefulness of a material in thermoelectric systems is determined by the device efficiency. These are determined by the material's electrical conductivity, thermal conductivity, Seebeck coefficient which change with temperature. The maximum efficiency of the energy conversion process (for both power generation

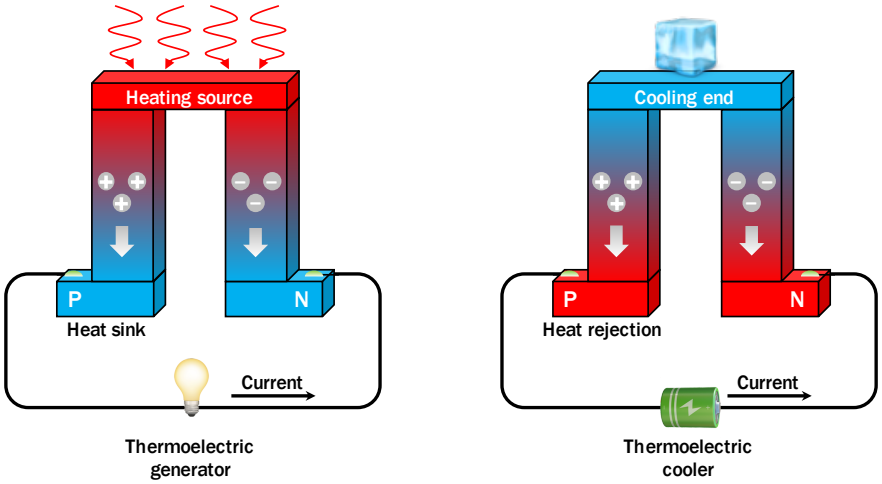

Figure 1.1: Schematics of both thermoelectric generator and cooler are shown.

and cooling) at a given point in the material is determined by the thermoelectric materials figure of merit zT, given by

$$zT = \frac{\sigma S^2 T}{\kappa} \tag{1.2}$$

which contains the Seebeck coefficient S, thermal conductivity κ, electrical conductivity σ, and temperature T. The thermal conductivity is $\kappa = \kappa_{\text{ph}} + \kappa_{\text{el}}$, where κ_{ph} and κ_{el} are the phonon and electron contributions, respectively. Additionally, often the thermoelectric power factor is reported for a thermoelectric material, defined as σS^2 which represents the efficiency of generating energy.

In the following 100 years, the research on thermoelectric materials was mainly carried out for metallic materials. The conversion efficiency is low, so the research and applications of thermoelectric materials and thermoelectric conversion devices had been progressing slowly. In the 1950s, Abram Ioffe discovered that the thermoelectric conversion efficiency of semiconductor materials is much better than that of metal materials, with an enhancement of an order of magnitude. As a result, the use of semiconductor thermoelectric materials has led to an increasing number of practical thermoelectric devices. In recent years, with the increasingly serious environmental pollution and energy crisis around the world, the need of further development of advanced thermoelectric is also increasing.

The half-Heusler family, as one of the most fascinating intermetallic systems, has gained considerable attention in recent decades due to their unique transport and magnetic behaviors. These materials have general formula XYZ (X and Y representing transition metals, Z a tetrel or pnictogen element) [1–3], and can be formally derived from the cubic Heusler phases X_2YZ by removing one of the two equivalent X atoms, leading to a structural vacancy. The ideal valence electron concentration (VEC) of half-Heusler compounds is 8 or 18 electrons per formula unit [4–8], with VEC $= 8$ for those cases (not discussed here) where X and Y are main-group elements, and with semiconducting or semimetallic behavior often observed with VEC $= 18$ [2–5, 9] in transition-metal half-Heuslers. With a rich combination of chemical elements stablized in this structure, this feature leads to interesting properties, from nonmagnetic semiconductors to ferromagnetic half metals, as well as other anomalous behavior, including strongly correlated electrons and topological insulator behavior [10–12].

To better understand the mechanism and further improve thermoelectric performance, the NMR technique can be used as a local probe to reveal information about electronic properties, phonon behavior and native defects [13–15]. For half-Heusler materials, there have been several previous works applying NMR. In Fig. 1.2, a summary of known half-Heuslers is shown, with NMR studies of half-Heusler materials also shown. Fig. 1.2 was assembled from multiple published works on half-Heuslers. Among these the existing NMR studies are shown, with some specified as having non-trivial topological features, all of which are band inverted semimetals [11, 12, 16, 17]. Other NMR studies shown in Fig. 1.2 are Ref. [15, 18–28]. The half-Heusler compositions studied in the dissertation (shown by stars) are transition-metal or rare-earth half-Heuslers which follow the 18-electron stability rule.

Within the half-Heusler system, NbFeSb has recently been of particular interest due to its excellent thermoelectric performance for high-temperature applications and since its composition places it within the realm of earth abundant thermoelectric materials [29]. In substituted compositions such as $Nb_{1-x}Ti_xFeSb$ ($x = 0.05$, 0.1, 0.2, 0.3), NbFeSb-based semiconductors can exhibit a large power factor, above 100 $\mu W\,cm^{-1}\,K^{-2}$ [29–31]. Substituted elements can control the carrier

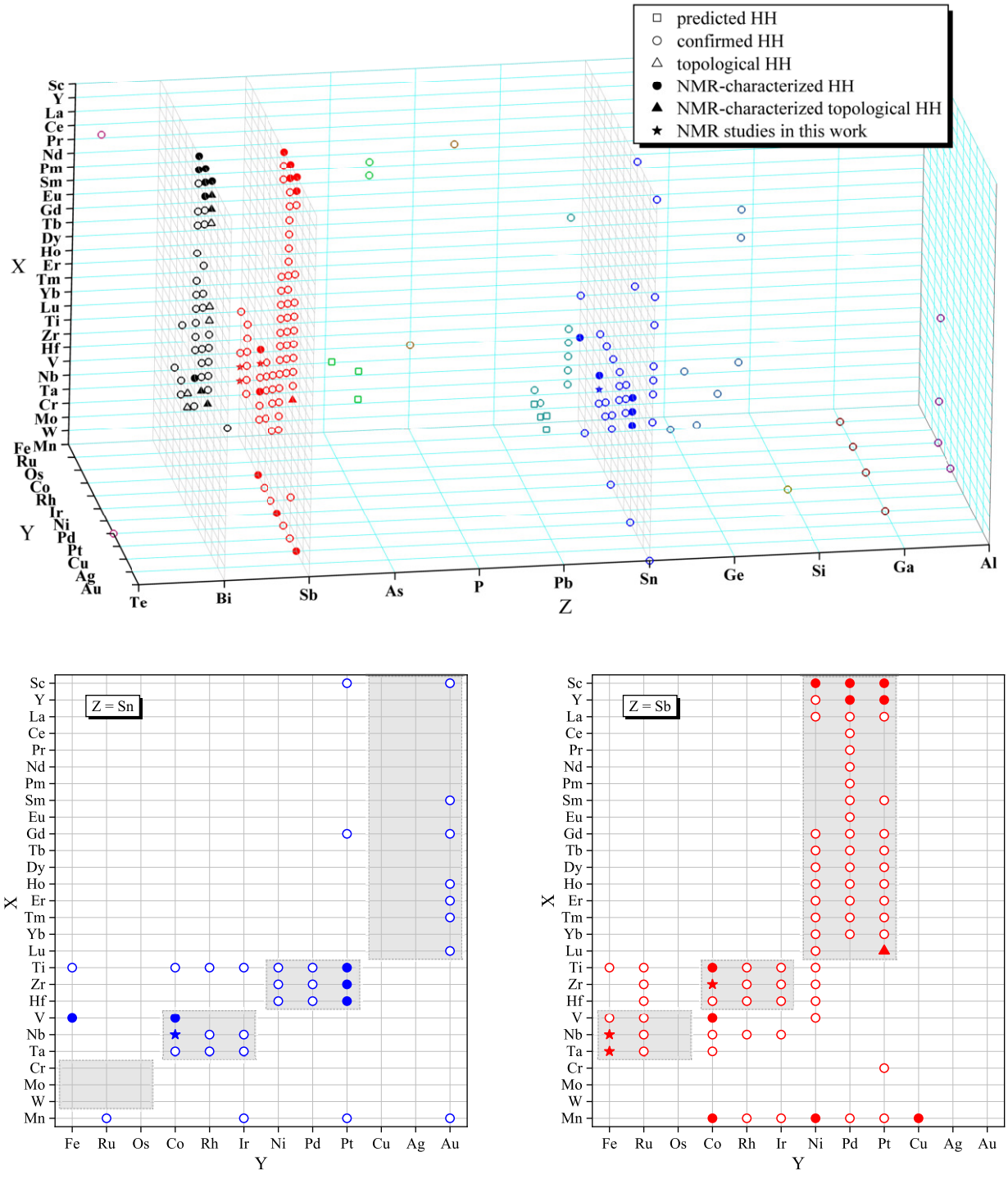

Figure 1.2: Summary of NMR studies of half-Heusler materials with *XYZ* composition. Existing and predicted compositions shown, with materials studied here shown by star symbols. Lower panels show Sn and Sb compositions. 18-electron compositions are boxed in.

density, for example Ti which changes the total electron count in NbFeSb, allowing the transport properties to be tuned, thus enabling the electronic behavior to be optimized. A number of different types of half-Heusler alloys have been designed with multiple elemental substitutions and shown to have high figures of merit ($zT > 1.5$) [32–35]. Based on these alloys, thermoelectric generators thus have the potential to reach a high power-conversion efficiency [34–36], enhancing the prospect of future thermoelectric applications. However, native defects can also counteract the desired effects or otherwise degrade the electronic response. The nature of these defects has been explored experimentally for several compounds, such as ZrNiSn and TiCoSb [37–39].

Besides NbFeSb-related half-Heuslers, there have been other half-Heusler materials drawing great attention due to their excellent thermoelectric performance. TaFeSb has been recently reported as a stable thermoelectric candidate and shown promising thermoelectric properties [35]. ZrCoSb-based materials have also been widely studied and shown promising zT values and low thermal conductivity [40].

Similar to the half-Heusler system, skutterudites are another family of materials which are excellent candidate thermoelectric materials. Filled skutterudites $M_zT_4X_{12}$, where M is a guest atom such as Ba or Yb, T represents a transition metal (Co, Rh, Ir or Fe), and X is a pnicogen or chalcogenide, have gained considerable attention due to their outstanding thermoelectric performance, as well as superconductivity, magnetic ordering, unusual metal-insulator transitions, and heavy fermion behavior [41–46] with NMR studies summarized in Ref. [47]. Many of the semiconducting filled skutterudites obey the phonon-glass electron-crystal concept explaining the significant reduction in thermal conductivity [48]. This behavior was first experimentally observed by Morelli *et al.* [49], as a lattice thermal conductivity decreases due to loosely bonded Ce guests in $FeSb_3$. Although the guest atoms act as dopants in addition to inducing low thermal conductivity, they can also modify the electronic behavior, for example, $4f$ states of elements such as Ce can introduce flat bands and lower the carrier mobility.

Recently, filled $CoSb_3$-based materials have been studied intensely due to their excellent thermoelectric response [50–53]. Although the filler atoms occupy the guest positions in these skut-

terudite materials, as shown here the rattling behavior does not play a large role for these compositions. On the other hand, the native electronic defects in these skutterudites have been particularly interesting because of their crucial importance for improving thermoelectric efficiency [54–59]. In the work described below, NMR studies combined with transport measurements have been used to address such electronic properties.

1.2 Topological Chalcogenides

One of the most important research areas of condensed matter physics is to discover new states of matter. The common solid, liquid and gas states in daily life are three different states of matter. Conductive metals *vs* non-conductive insulators is another way to classify the physical states of matter. The energy band theory of solids tells us that this is determined by the arrangement of electrons in solids. In this theory which applies if electron-electron interactions are not too strong, electron states form an energy band structure in a periodic solid, and the Pauli exclusion principle makes each state only contain up to two electrons with opposite spins. According to Aufbau principle, electrons fill energy bands in the order of energy level. If a certain energy band happens to be filled, and there is a finite energy gap between the lowest unoccupied energy band, it is an insulator; if there is an energy band that is not filled and partly occupied, that is metal.

With the help of the topological classification methods for closed curved surfaces in mathematics, topological invariants of electronic energy band structures have been introduced to further classify insulators into ordinary insulators and topological non-trivial insulators, that is, topological insulators (TIs). For TIs, there has been a few decades since people started to work on related problems. Time-reversal symmetry-protected two-dimensional edge states were first predicted by A. Volkov and O. Pankratov [60, 61] leading to the start of topological insulators. Afterwards, the 2D topological insulator or the quantum spin Hall state was predicted by C. Kane and E. Mele [62], and A. Bernevig and S.-C. Zhang [63]. The concept then soon developed to 3D topological insulator by J. Moore and L. Balents [64]. Besides those, there has been also many other critical problems being addressed, such as topological phase transition in two-dimensional systems by M. Kosterlitz and D. Thouless [65].

According to different topological invariants, topological insulators have been then further classified into integer Hall effect states, Z_2 topological insulators [62], and topological crystalline insulators [66]. These non-trivial topological states have attracted great attention due to their novel edge states. Although the bulk state is not conductive, unlike ordinary insulators there is a conductive state protected by the topological characteristics on the edges of a TI, which could thus be used in ideal current-carrying devices without energy dissipation, and this has huge potential for future application. Also, spintronic devices based on spin-momentum coupling are also promising, as well as advanced magnetoelectronic and optoelectronic devices. With research on topological insulators progressing, there will be a natural question being asked: do metals also have a topological classification of topological metals and ordinary metals?

To answer this question, the starting point is Dirac equation proposed by Paul Dirac [67] describing electronic states with relativistic effects. Later Weyl pointed out that the massless solution of the Dirac equation described a pair of new particles. This pair of new particles has opposite chirality, wherein each is a Weyl fermion. The massless Dirac electron is a simple superposition of Weyl fermions with opposite chirality, which is found in Dirac semimetals. In 2012 and 2013, Na_3Bi [68] and Cd_3As_2 [69] were predicted to be Dirac semimetals whose Fermi surfaces are composed of overlapping Weyl fermion pairs and protected by lattice symmetry. In 2014, those theoretical predictions were verified by experiments and this was therefore the first discovery of a three-dimensional version of graphene [70, 71]. From then on, the Dirac semimetals have been attracting great attention, and have formed a current research hotspot in the field of condensed matter physics. Besides Dirac semimetals, there are also Weyl semimetals and nodal-line semimetals. Possible energy dispersions for these are shown in Fig. 1.3.

$ZrTe_5$ has attracted great interest as an exotic quantum material due to observations such as the chiral magnetic effect [73] and 3D quantum Hall effect [74]. Initially, monolayer $ZrTe_5$ was predicted to be a 2D topological insulator (TI) [75], with bulk $ZrTe_5$ argued to be either a weak TI (WTI) or strong TI (STI) [75], where the latter implies a more robust protection of topological surface states from disorder, along with presence of a bulk gap. The STI state possesses helical

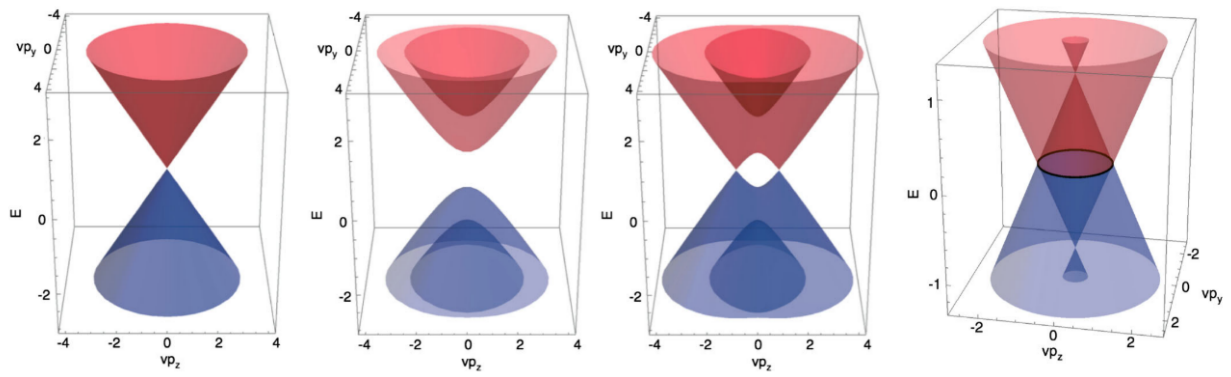

Figure 1.3: Energy dispersion characteristics of Dirac semimetal, normal semiconductor, Weyl semimetal and nodal-line semimetal. Reused with the permission from Ref. [72]. Copyright (2018) American Physical Society.

Dirac surface states which might be utilized along with the proximity effect as the basis for devices for quantum computation [76]. It was further predicted that a topological phase transition separates these TI states [77,78] with a temperature-driven valence and conduction band inversion associated with the topological phase transition [77].

Since these predictions were made, the topological nature of $ZrTe_5$ has remained controversial. Angle-resolved photoemission spectroscopy (ARPES) studies [73,79] and the observed chiral magnetic effect [73] indicate a 3D Dirac semimetal state, also suggested by infrared [80], magneto-optical [81], and transport [82] measurements. Based on high-resolution ARPES, however, it was concluded that $ZrTe_5$ should be a 3D WTI at low temperatures [83]. Scanning tunneling microscopy [84, 85] and Shubnikov-de Haas results [86] also support a WTI interpretation, while other probes of the metallic surface states argued that $ZrTe_5$ is a low-T STI [77,87]. Regarding the topological phase transition, a recent infrared [88] study suggested that $ZrTe_5$ transits from WTI to STI with temperature decreasing, with the Dirac semimetal state appearing at the transition, while ARPES results [89] have shown the gap remaining open and the sample a WTI over the measured temperature range. Besides these topological features in $ZrTe_5$, the Dirac dispersion can also lead to other extreme quantum behaviors in relatively weak magnetic fields because of the large Fermi velocity and corresponding Landau level splitting.

In recent years, there has been great interest in layered transition metal dichalcogenides (TMDCs), with MX_2 composition and comprised of a wide range of transition metal (M = Mo, W, Ta, Zr, Hf, *etc.*) and chalcogen (X = S, Se, or Te) elements. The TMDC family offers platforms for exploring striking physical phenomena and exotic electronic device applications [90]. Among TMDCs, $ZrTe_2$ has been relatively little investigated; however, recent work [91–93] has indicated interesting topological features in this material both in the normal state and as a doped superconductor. Also, other zirconium tellurides have been of considerable interest. For instance, as described above, $ZrTe_5$ shows interesting topological properties and unique physical properties such as the chiral magnetic effect [73] and three-dimensional quantum Hall effect [74], as well as quantum thermoelectric behavior [94] and distinctive optical behavior [95]. $ZrTe_5$ also exhibits a topological phase transition separating the strong and weak topological insulator states [77, 78, 96] with a temperature-driven valence and conduction band inversion associated with this topological phase transition [77]. Other Zr-Te materials include the layered material $ZrTe_3$ which has also been long studied due to interesting behavior such as a charge density wave phase transition [97]. Recently, theoretical calculations indicate distinctive topological behavior in ZrTe, which possesses triple-point fermions coming from the three-fold degenerate crossing points formed by the crossing of a double-degeneracy band and a nondegeneracy band [98].

Regarding $ZrTe_2$, the theoretical predictions from several groups give rather different results [91–93,99–101], leading to the importance of determining its topological nature. Although several theoretical reports [91, 99] predicted $ZrTe_2$ to be a simple metal, there is no direct experimental evidence supporting this result. However, recent ARPES studies [93] present evidence of massless Dirac fermions observed in the $ZrTe_2$ bulk phase, while the DFT calculations [92, 93] also support the topological semimetal prediction. As a topological semimetal candidate from the layered TMDC family, $ZrTe_2$ may show attractive electrical transport phenomena and promising prospects for quantum device applications.

As a powerful experimental technique, NMR can provide useful insights on different perspectives of various topological materials. In particular, NMR is uniquely sensitive to the behavior

and dynamics of carriers very close to the Fermi level, the understanding of which is essential for the understanding of Dirac and Weyl semimetals, as demonstrated in this dissertation. In other work on topologically inverted materials, NMR shifts have been shown to be good indicators of the band inversion in half-Heusler bismuthides, such as YPdBi and YPtBi [11, 16], although the reason behind this is still unclear. NMR has also been applied to investigate the Weyl semimetals, such as TaP [102] and TaAs [103]. Ref. [103] showed that Landau diamagnetism can be a unique fingerprint for 3D topological semimetals. NMR has also been utilized in studying organic materials, such as electronic correlations in α-(BEDT-TTF)$_2$I$_3$ [104]. Besides the topological semimetals, NMR has also been previously used to study topological insulators, for example materials prepared as nanomaterials so that the surface resonance could be detected. In Ref. [105], NMR was shown to be an efficient method to detect the Dirac states in such materials. Also Ref. [106] demonstrated the NMR signals of protected TI surface states with magnetic shielding that is influenced by the Dirac electrons.

2. SOLID STATE NMR THEORY AND TECHNIQUES

Nuclear magnetic resonance was first described and measured in molecular beams by Isidor Rabi in 1938 [107], and in 1944, Rabi was awarded the Nobel Prize in Physics for this work. In 1946, Felix Bloch and Edward Mills Purcell applied the NMR technique for use on liquids and solids, for which they shared the Nobel Prize in Physics in 1952 [108, 109]. Since then, NMR technique has been further developed and expanded. In the current research community, NMR is widely used in many fields including physics, chemistry, biology, and medical research to provide great assistance on studying materials and health-related topics.

2.1 Basic Principles in NMR

Most nuclei have a spin $\mathbf{I}$ and a magnetic moment $\boldsymbol{\mu} = \gamma_n \hbar \mathbf{I}$, where γ_n is the nuclear gyromagnetic ratio. The Hamiltonian of a nucleus in an external magnetic field $\mathbf{H}$ due to the Zeeman effect is

$$\mathcal{H} = -\boldsymbol{\mu} \cdot \mathbf{H}. \tag{2.1}$$

With the magnetic field $\mathbf{H} = H_0 \hat{z}$, the corresponding eigenvalues are

$$E = -m\gamma_n \hbar H_0, \qquad m = I, ..., -I. \tag{2.2}$$

Due to the existence of the energy difference between energy levels, it is possible to observe an absorption spectrum by applying a RF pulse with a proper frequency ω_0 that satisfies $\hbar\omega_0 = \Delta E = \gamma_n \hbar H$, where $H = H_0 + H_{\text{loc}}$ includes both the external field and local environment.

2.2 Equations of Motion

Applying an external magnetic field $\mathbf{H}$ to a nuclear spin system, with a magnetization $\mathbf{M}$, will produce a torque $\mathbf{M} \times \mathbf{H}$ to force $\mathbf{M}$ to precess around $\mathbf{H}$. Writing the equation of motion in the

laboratory frame and including exponential relaxation processes, we obtain

$$\frac{dM_z}{dt} = \gamma_n(\mathbf{M} \times \mathbf{H})_z - \frac{M_z - M_0}{T_1}, \tag{2.3a}$$

$$\frac{dM_{x,y}}{dt} = \gamma_n(\mathbf{M} \times \mathbf{H})_{x,y} - \frac{M_{x,y}}{T_2}, \tag{2.3b}$$

where M_0 is the equilibrium magnetization, T_1 is spin-lattice relaxation time and T_2 is the spin-spin relaxation time. From an analysis of the T_1 and T_2, it is possible to quantify the atomic motion or even transport properties.

2.3 Knight Shift and Korringa Relation

The Knight shift is named after Walter Knight, who first observed the phenomenon in ^{63}Cu NMR for metallic copper, where the shift is an order of magnitude larger than the chemical shifts. Later, this was found to be typical for metallic materials. Considering the interaction between a nucleus and a free electron, there are three terms that need to be considered: the Fermi contact interaction, magnetic dipole interaction and orbital angular momentum interaction. The Hamiltonian describing the interactions between the nucleus and conduction electrons can be expressed as:

$$\mathcal{H} = -2\mu_B\gamma_n\hbar\mathbf{I} \cdot \left\{ \frac{8\pi}{3}\mathbf{S}\delta(\mathbf{r}) + \left[\frac{3\mathbf{r}(\mathbf{r}\cdot\mathbf{S})}{r^5} - \frac{\mathbf{S}}{r^3}\right] - \frac{\mathbf{r}\times\mathbf{p}}{r^3} \right\} \tag{2.4}$$

where μ_B is the Bohr magneton, γ_n is the gyromagnetic ratio, $\mathbf{I}$ and $\mathbf{S}$ are the nuclear spin and electron spin, respectively, and $\mathbf{r}$ is the radius vector of the electron with the nucleus at the origin.

The first term of Eq. 2.4 is the Fermi contact term, which is usually used to explain Knight shifts in a simple metal. The second term describes the spin-dipole interaction, a source for NMR line shape broadening for powders which can also produce a shift in some cases. The last term represents the spin-orbit interaction, which is usually important in transition metals and contributes to the anisotropic Knight shift.

If we just consider *s*-state electrons, only the Fermi contact term will survive after taking an average over the electron wave function. By assuming the external field is in the z direction, the

effective Fermi contact interaction can be written as

$$\mathcal{H} = -\gamma_n \hbar I_z \left(\frac{8\pi}{3} \langle |\Psi_s(0)|^2 \rangle_{E_F} \right) \chi_P H_0, \tag{2.5}$$

where χ_P is the Pauli paramagnetic spin susceptibility and $\Psi_s(0)$ is the electron wave function measured at the nucleus. This energy can be treated as a small perturbation of the external field (ΔH) and will lead to a small resonance frequency shift, called the Knight shift, as below:

$$K = \frac{\Delta H}{H_0} = \frac{8\pi}{3} \langle |\Psi_s(0)|^2 \rangle_{E_F} \chi_P. \tag{2.6}$$

If one expresses the relationship between the experimental resonance frequency ν_m in a metal and the resonance frequency ν_d in a diamagnetic reference as

$$\nu_m = \nu_d + \Delta\nu, \tag{2.7}$$

we can find the connection that $\Delta\nu/\nu_d = H_{\mathrm{HF}} \chi_P / \mu_B$, where H_{HF} is the hyperfine coupling field. For Fermi contact interaction, the following results are typically observed: (1) $\Delta\nu$ is always positive in simple metals. (2) $\Delta\nu/\nu_d$ is unaffected by external field change. (3) $\Delta\nu/\nu_d$ is nearly temperature independent. (4) $\Delta\nu/\nu_d$ increases with increasing nuclear charge. However, in this dissertation, most cases are not simple metal cases dominated by *s* electrons and core polarization plays a more significant role contributing to the Knight shift.

For metallic materials, conduction electrons will control the relaxation mechanism and only electrons at the Fermi level need to be considered. In this case, the Korringa relation can be derived from the Fermi contact interaction and gives an expression

$$K^2 T_1 T = \frac{\hbar}{4\pi k_B} \frac{\gamma_e^2}{\gamma_n^2}, \tag{2.8}$$

where γ_e is the electron gyromagnetic ratio and k_B is the Boltzmann constant. Note that this is only

correct for metallic materials, and the relationship is more complicated for semiconductors. The Korringa ratio can also be affected by a number of sources, such as electron-electron interactions, and exchange enhancement. So, although a constant behavior can be observed, the K^2T_1T value is not necessary to be exactly the same as calculated from the equation above.

2.4 Chemical Shift

Nuclei are always surrounded by an electron cloud which interacts with the nuclear spin angular momentum. The surrounding electrons will build up a modified magnetic field around their nuclei and affect the spin energy levels by a small amount. The change of nuclear magnetic resonance frequencies for the same kind of nucleus, due to variations in the electron distribution, is called the chemical shift. The Hamiltonian term associated with this chemical shift is simply a Zeeman operator,

$$\mathcal{H}_{\mathrm{CS}} = -\mathbf{I} \cdot \boldsymbol{\sigma} \cdot \mathbf{B}, \tag{2.9}$$

where $\boldsymbol{\sigma}$ is the chemical shift tensor.

For solid state environments, the Hamiltonian for axial conditions is

$$\mathcal{H}_{\mathrm{CS}} = -\sigma_i \omega_0 I_z - \frac{3\cos^2\theta - 1}{2}(\sigma_{zz} - \sigma_i)\omega_0 I_z, \tag{2.10}$$

where $\sigma_i = (\sigma_{xx} + \sigma_{yy} + \sigma_{zz})/3$ is the isotropic chemical shift given by the diagonal sum of the shift tensor $\boldsymbol{\sigma}$, and θ is the polar angle between the polarizing field direction and the principal axis of $\boldsymbol{\sigma}$.

Knight shifts tend to be an order of magnitude larger than the small paramagnetic chemical shift for metallic materials, so that if high accuracy is not required, we can often pick a standard reference and define the Knight shift in percentage as

$$K = \frac{\nu_m - \nu_{\mathrm{ref}}}{\nu_{\mathrm{ref}}} \times 100\%, \tag{2.11}$$

where ν_m and ν_{ref} are the measured resonance frequencies for the object and the reference under

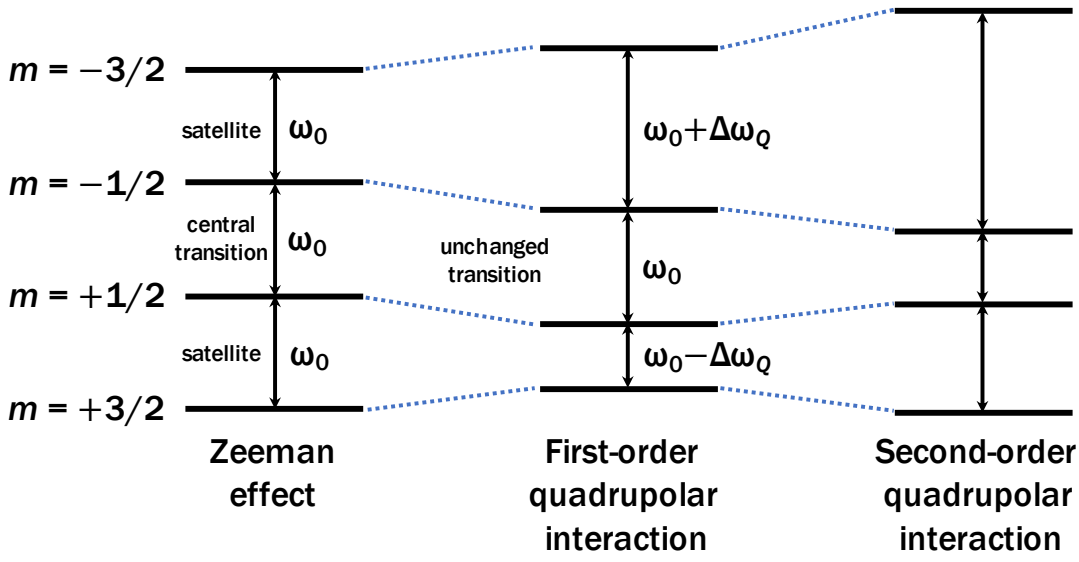

Figure 2.1: Zeeman levels due to magnetic-only interaction, and with the addition of first and second order quadrupole interaction. The central transition splitting does not change due to the first order quadrupole interaction in contrast to the satellite transition.

the same external field. In other cases, such as described in Chapter 5 below, the Knight shift and chemical shift must be carefully separated in order to probe the underlying electronic features.

2.5 Quadrupole Interaction

The quadrupole interaction needs to be taken into consideration for nuclei with $I > 1/2$. (For $I = 1/2$, the average quadrupole interaction is zero.) For $I > 1/2$, the charge distribution is non-spherical, which interacts with an electric field gradient to produce a change in the energy levels in addition to the Zeeman effect, as shown in Fig. 2.1. The interaction energy E of a charge distribution of density ρ with a potential V can be expressed as

$$E = \int \rho V d\tau, \tag{2.12}$$

and the leading term in its expansion gives the the effective quadrupolar Hamiltonian $\mathcal{H}_Q$,

$$\mathcal{H}_Q = \frac{eQ}{6I(2I-1)} \sum_{\alpha\beta} V_{\alpha\beta} \left[\frac{3}{2}(I_\alpha I_\beta + I_\beta I_\alpha) - \delta_{\alpha\beta} I^2 \right], \tag{2.13}$$

where $V_{\alpha\beta}$ is the field gradient and Q is the quadrupole moment of the nucleus.

The frequency shift of NMR transitions can also be calculated from Eq. 2.13 as a series of perturbations for the case that the eigenvalues of Eq. 2.13 are small compared to $\hbar\omega_0$. For example, the first order quadrupolar effect for high symmetry systems gives

$$\nu(m \leftrightarrow m-1) = \nu_0 + \frac{\nu_Q(3\mu^2-1)(m-1/2)}{2}, \tag{2.14}$$

where m is the energy level, $\mu = \cos\theta$ and $\nu_Q = \frac{3e^2qQ}{2I(2I-1)h}$ is the pure quadrupolar $2I(2I-1)h$ frequency with $eq = V_{zz} = \partial^2 V/\partial z^2$, the z-z principal value of the EFG, with z defined as the direction with largest principal value. This indicates that the central transition ($m = 1/2$) will not be shifted by the first order quadrupole effect. But higher order quadrupolar effects, most importantly the second order, will still bring additional changes to the frequency shift. For the cases with axial symmetry or higher, the effect gives a net NMR shift described as

$$\begin{aligned}\nu(m \leftrightarrow m-1) = \nu_0 + \frac{\nu_Q(3\mu^2-1)(m-1/2)}{2} + \frac{\nu_Q^2}{32\nu_0}(1-\mu^2)\times \\ \{[102m(m-1) - 18I(I+1) + 39]\mu^2 - [6m(m-1) - 2I(I+1) + 3]\}.\end{aligned} \tag{2.15}$$

2.6 Dipole Coupling

In solid state NMR, dipolar coupling and quadrupolar interactions are also important. The dipolar coupling describes the interaction between the dipole moments of different nuclei. The Hamiltonian of the interaction between two magnetic dipoles can be written as

$$\mathcal{H} = -\frac{\mu_0}{4\pi r_{jk}^3}[3(\mathbf{m_j}\cdot\mathbf{e_{jk}})(\mathbf{m_k}\cdot\mathbf{e_{jk}}) - \mathbf{m_j}\cdot\mathbf{m_k}], \tag{2.16}$$

where $\mathbf{e_{jk}}$ is a unit vector parallel to the line joining the center of the two dipoles, $\mathbf{r_{jk}}$ is the distance between two dipoles, $\mathbf{m_k}$ and $\mathbf{m_j}$. For two interacting nuclear spins, this can be expressed by

$$\mathcal{H} = -\frac{\mu_0}{4\pi}\frac{\gamma_j\gamma_k\hbar^2}{r_{jk}^3}[3(\mathbf{I_j}\cdot\mathbf{e_{jk}})(\mathbf{I_k}\cdot\mathbf{e_{jk}}) - \mathbf{I_j}\cdot\mathbf{I_k}], \tag{2.17}$$

where γ_j and γ_k are gyromagnetic ratios of the two nuclei with spin $\mathbf{I_j}$ and $\mathbf{I_k}$.

The direct dipole coupling is useful for structural studies. Estimation of this coupling provides a direct spectroscopic route to the distance between nuclei and hence the geometrical form of the molecule, or additionally also on intermolecular distances in the solid state leading to NMR crystallography notably in amorphous materials. Although internuclear magnetic dipole couplings contain a great deal of structural information, in isotropic solutions, they average to zero as a result of rotational diffusion. In addition, the pseudo-dipolar interaction often can be large, which may need further consideration.

2.7 NMR Pulse Sequences

The most commonly used NMR pulse sequences in my measurements are shown in Fig. 2.2. With proper combinations of multiple spin-echo sequences and variable parameters, we can construct T_1 and T_2 sequences to obtain relaxation properties. We can use a RF pulse sequence (180° - T_{wait} - 90° - T_{delay} - 180°) to measure the spin-lattice relaxation time T_1. Comparing to spin-echo sequence (90° - T_{delay} - 180°), there is another 180° pulse placed at a time T_{wait} before it. The 180° pulse tips magnetization to the $-z$ direction in the rotating frame. The spin systems will return to equilibrium with the characteristic time T_1. The spin-echo amplitude measured by 90° - T_{delay} - 180° sequence thus depends on the time T_{wait}. By repeating such a spin-echo sequence (180° - T_{wait} - 90° - T_{delay} - 180°) with different T_{wait}, a magnetization recovery curve can be constructed to reveal the value of T_1. For nuclei with spin 1/2, like Te, the central transition recovery curve for the magnetic contribution is given as

$$\frac{M(T_{\mathrm{wait}})}{M(\infty)} = 1 - \alpha e^{-\frac{T_{\mathrm{wait}}}{T_1}}, \tag{2.18}$$

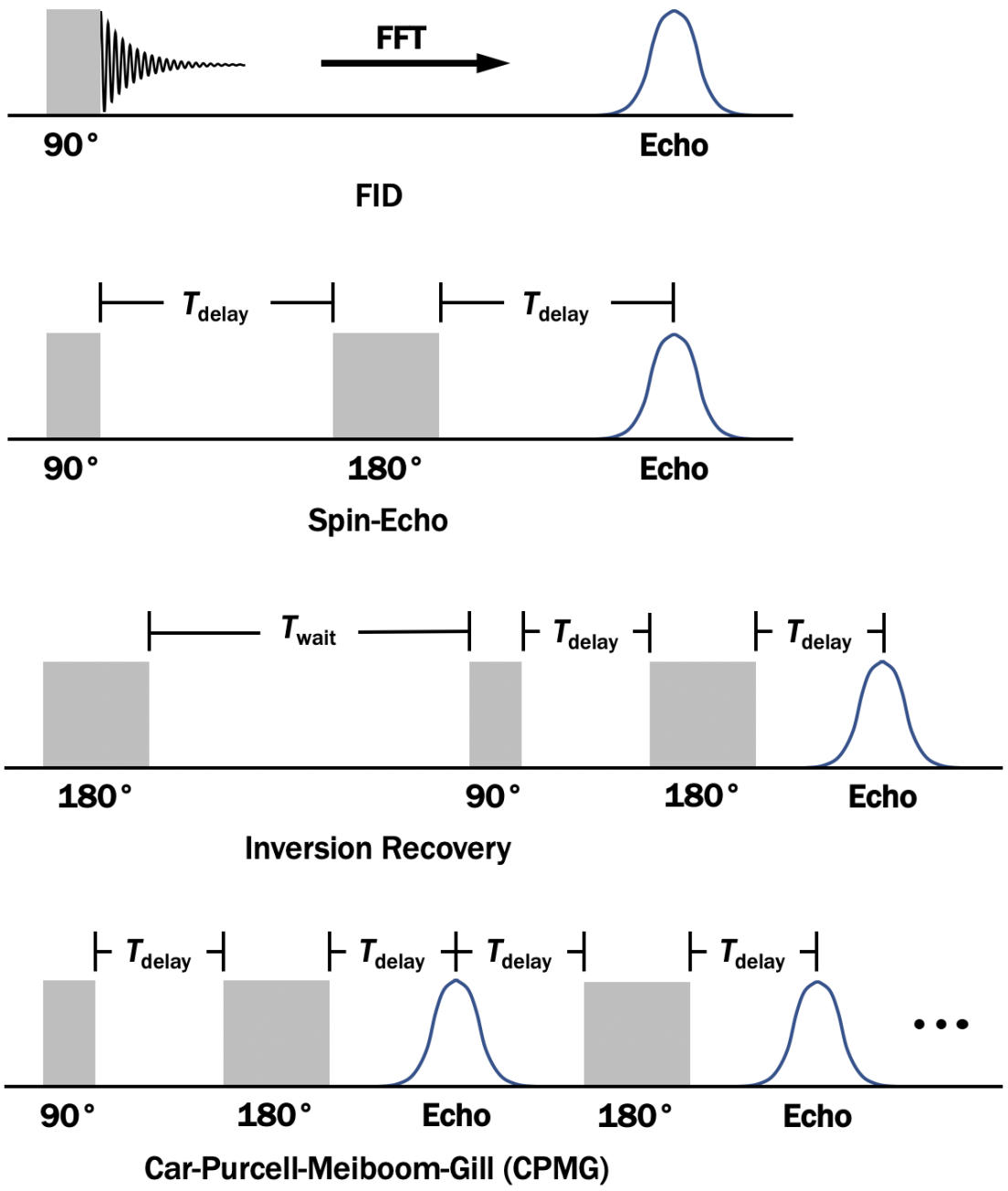

Figure 2.2: Free induction decay (FID), spin echo, inversion recovery, and CPMG sequences.

and for nuclei with spin > 1/2, the effect is more complicated, for example, for spin 9/2, such as ^{93}Nb, the corresponding recovery curve is given as

$$\frac{M(T_{\text{wait}})}{M(\infty)} = 1-\alpha\Big(0.152e^{-\frac{T_{\text{wait}}}{T_1}}+0.14e^{-\frac{6T_{\text{wait}}}{T_1}}+0.153e^{-\frac{15T_{\text{wait}}}{T_1}}+0.192e^{-\frac{28T_{\text{wait}}}{T_1}}+0.363e^{-\frac{45T_{\text{wait}}}{T_1}}\Big), \tag{2.19}$$

where $M(\infty)$ is the saturating magnetization and α is a fitted amplitude. Note that this is for the case that satellites are well separated from central transition and the saturation pulse affects only the central line.

2.8 Magic Angle Spinning NMR

Magic angle spinning (MAS) was first described by Andrew, Bradbury, and Eades in 1958 [110] and independently by Lowe in 1959 [111]. This technique is to make the broad lines narrower in order to increase the resolution of NMR spectrum. In regular NMR measurements, the sample is fixed in the sample coil which lies perpendicularly to the external magnetic field. The nuclear spins will experience multiple orientation-dependent interactions, such as dipole-dipole coupling, anisotropic chemical shifts and quadrupole interactions, which will lead to broadening of the NMR lines. The dipole-dipole and first order quadrupole interactions have an angular dependence $(3\cos^2\theta - 1)$ connected to the second rank spherical harmonic. To more precisely identify the signals, we can manually set $3\cos^2\theta - 1 = 0$, giving the magic angle of $\theta = 54.7°$. In the MAS technique, a rapid spin for the sample about an axis at this magic angle to the external field can average out most of these interactions and make the NMR lines narrower. Also note that for large quadrupole splitting, MAS may not give any significant broadening, so this technique was only used for specific cases in this dissertation.

3. EXPERIMENTAL APPARATUS AND COMPUTATIONAL METHODS

3.1 NMR Spectrometer

All NMR experiments in this dissertation except for MAS measurements were performed using a home-built NMR pulse spectrometer and a set of customized NMR probes which cover a temperature range from 4.2 K to 350 K. The major components of our NMR spectrometer include a superconducting magnet, a pulse sequence generator (PSG), a radio frequency (RF) synthesizer, transmitters, signal receivers, a detecting probe, a cryostat system and a controlling system based on a LabVIEW program. A block diagram of this spectrometer is illustrated in Fig. 3.1.

While executing a certain pulse sequence, the RF is produced by a frequency synthesizer, and the PSG is used to control the pulses. The transmitter is used to deliver the RF radiation to the sample to perturb the nuclear spin system from its equilibrium state. During the relaxation process of the spin system, an electric signal can be recorded from the pick-up coil. The receiver detects, amplifies, and digitally records the signal. Normally the voltage induced in the pick-up coil is as low as one microvolt, and it has to be amplified before being digitally recorded by the computer.

The circuit of the probe is basically a tunable LC circuit, and the sample coil serves as the inductor of the LC circuit. It is used to excite and detect NMR signals from the sample inside the coil. There is a general requirement that all components must be non-magnetic. There are also many other add-ons to the probe for additional functions. A platinum thermometer is attached inside the sample can for temperature detection from 4.2 K to room temperature. A home-made resistance heater, a Cu-Ni wire, is attached to the sample can of the probe for temperature adjustment. A cryostat system is needed to perform low-temperature NMR. In our case, liquid nitrogen was used to perform measurements from 77 K to room temperature, while liquid helium was used for the range from 4.2 K to 77 K.

To measure NMR shifts of different nuclei, the corresponding references are also needed. For ^{93}Nb, standard reference $NbCl_5$ in acetonitrile was used. For ^{121}Sb, standard reference $KSbCl_6$ in

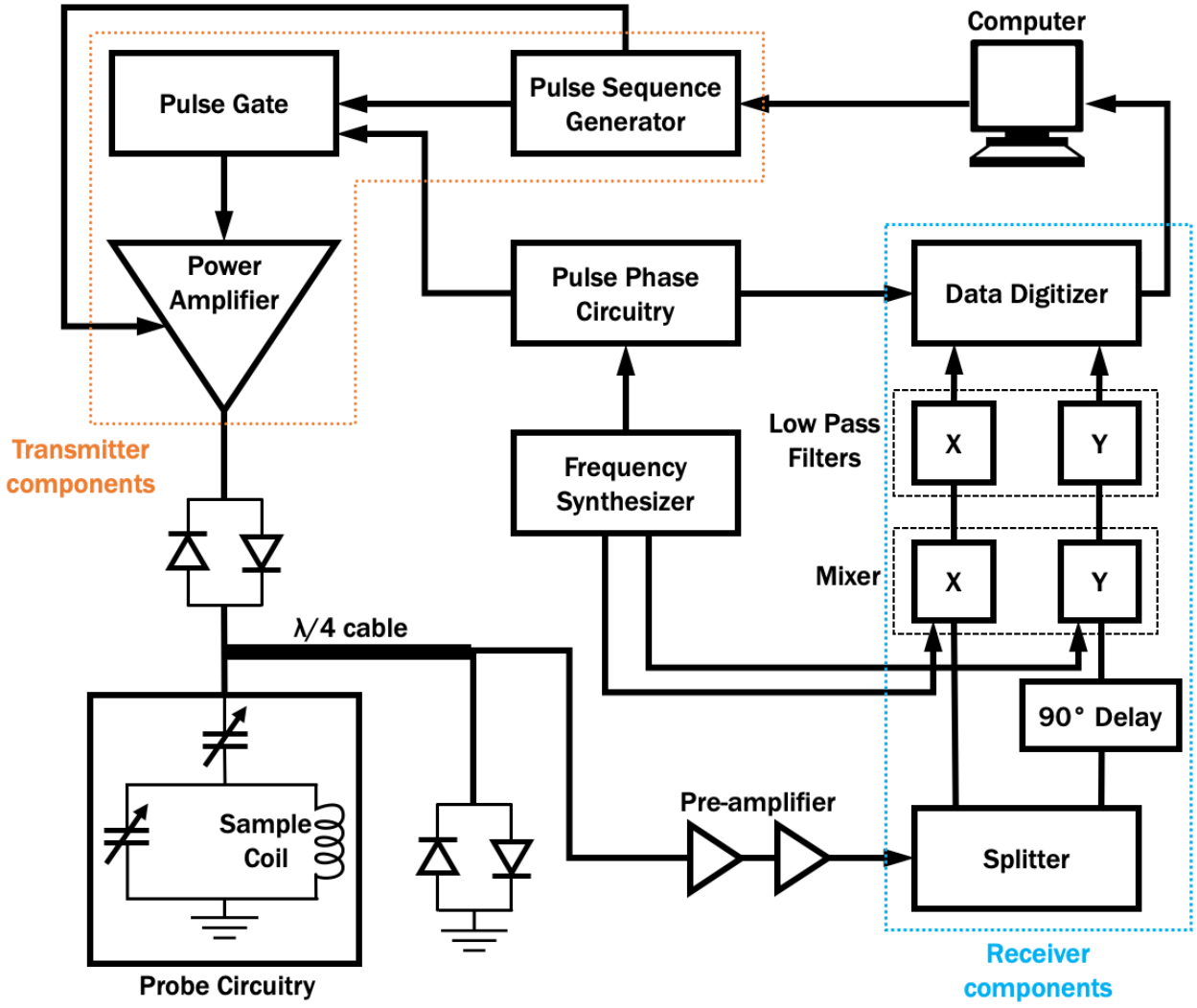

Figure 3.1: Block diagram of the NMR system.

acetonitrile was used. For ^{59}Co, $K_3Co(CN)_6$ was used as reference. For ^{125}Te, $Te(OH)_6$ was used as reference. Magic Angle Spinning (MAS) measurements on ^{93}Nb based samples were performed at the NMR facility in the Chemistry Department, using a Bruker Avance 400 MHz NMR instrument with $NbCl_5$ in acetonitrile as reference. All NMR measurements except for MAS were done by myself.

3.2 PPMS, SQUID, Mössbauer, XRD, and WDS

High-resolution powder X-ray diffraction (XRD) data were collected at the Advanced Photon Source, Argonne National Laboratory. Rietveld refinements (a technique described by Hugo Rietveld for use in the characterisation of crystalline materials) were performed using the Crystallography Data Analysis Software (GSAS-II) package [112] by myself. Wavelength dispersive spectroscopy (WDS) measurements were performed on multiple points on the samples using a Cameca SXFive Electron Microprobe. Hall coefficient and heat capacity measurements were conducted in a Quantum Design Physical Property Measurement System (PPMS) and these data were also analyzed by myself. A Quantum Design superconducting quantum interference device magnetometer (SQUID) was used to measure magnetic properties. All these measurements were carried out in user facilities.

3.3 Computational Packages

DFT calculations on density of states, band structures, optimized structures, electric field gradients and many other properties were carried out using in the WIEN2K package [113]. I have utilized XCRYSDEN package [114] to plot Fermi surfaces. All crystal structures in this dissertation are displayed using VESTA package [115]. DFT work in this dissertation was carried out by my labmate Dr. Nader Ghassemi.

3.4 Sample Preparation

In this dissertation, all half-Heusler samples were prepared by Prof. Zhifeng Ren's group. Skutterudites were prepared by Dr. Ballikaya and Prof. Uher at University of Michigan. Topological chalcogenides $ZrTe_5$ and $ZrTe_2$ were prepared by myself using chemical vapor transport (CVT)

method.

4. ADVANCED THERMOELECTRIC HALF-HEUSLER NbFeSb*

4.1 Introduction

In this chapter, to analyze the underlying electronic and magnetic properties of NbFeSb, I perform a series of measurements aimed at better understanding and eventual utilization of these materials. All half-Heusler samples were prepared by Dr. Ren's group at University of Houston. The DFT was conducted by my labmate Dr. Nader Ghassemi and I measured all the experimental results. In results from magnetic, NMR and specific heat measurements, I demonstrate the presence of several native defects in NbFeSb resulting in its very low native mobility and an enhanced carrier density above room temperature due to an impurity band.

4.2 Sample Preparation

Three samples with nominal composition NbFeSb were prepared by an arc melting, ball milling, and hot pressing process. Stoichiometrically weighed raw elements were melted several times in an Ar-protected chamber to form homogeneous ingots. These were loaded into an Ar-filled stainless steel jar and ball milled for 3 h. The ball milled powder was finally consolidated into 13 mm diameter disks via hot pressing. The hot pressing temperatures were 1050, 1000, and 900 °C with holding for 2 min. Here I denoted these samples as NbFeSb-1050, NbFeSb-1000, and NbFeSb-900 respectively.

4.3 Experimental Methods

High-resolution powder X-ray diffraction (XRD) data were collected at the Advanced Photon Source, Argonne National Laboratory using an X-ray wavelength of 0.412703 Å. NbFeSb-1050 results are shown in Fig. 4.1. Rietveld refinements were performed using the GSAS-II software package, and the lattice constant 5.9497 Å was obtained, with identical results for the other two samples within 0.0001 Å. This is close to the value 5.9522 Å reported in other work [116]. The

*Part of this chapter is reprinted from Ref. [15] (Y. Tian, H. Zhu, W. Ren, N. Ghassemi, E. Conant, Z. Wang, Z. Ren, and J. H. Ross, Jr., "Native defects and impurity band behavior in half-Heusler thermoelectric NbFeSb," Phys. Chem. Chem. Phys., vol. 20, no. 34, pp. 21960–21967, 2018) with permission from the PCCP Owner Societies.

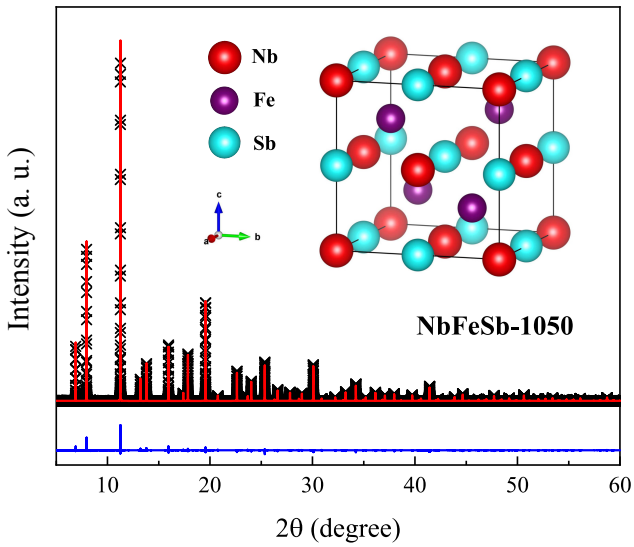

Figure 4.1: Powder XRD results for NbFeSb-1050 sample at 295 K with Rietveld refinement and difference plots. The half-Heusler structure is also shown superposed.

XRD results showed no sign of secondary phase.

Magnetic measurements were performed using a Quantum Design MPMS superconducting quantum interference device magnetometer. Specific heat and transport measurements were conducted using a Quantum Design Physical Property Measurement System. ^{93}Nb NMR experiments were carried out by applying a custom-built pulse spectrometer at a fixed magnetic field of about 9 T using shift standard $NbCl_5$ in acetonitrile, with positive shifts here denoting paramagnetic sign. Magic angle spinning (MAS) NMR measurements were performed using a Bruker Advance 400 spectrometer. To avoid multi-exponential effects due to quadrupole splitting, NMR T_1 measurements were performed using a saturating comb of pulses.

Resistivity and Hall measurements were performed at 300 K, on a piece of the NbFeSb-1050 sample cut into a Hall bar. The measured resistivity is 0.2 Ω cm, with Hall results corresponding to a hole density of 9×10^{19} cm^{-3}, assuming no compensation effects. This indicates a very small room-temperature hole mobility of about 0.3 cm^2 V^{-1} s^{-1}, considerably smaller than found in Ti-substituted NbFeSb [29]. A very small mobility was previously noted for unsubstituted NbFeSb [117, 118], apparently due to nearness to a localization transition. For example, assuming

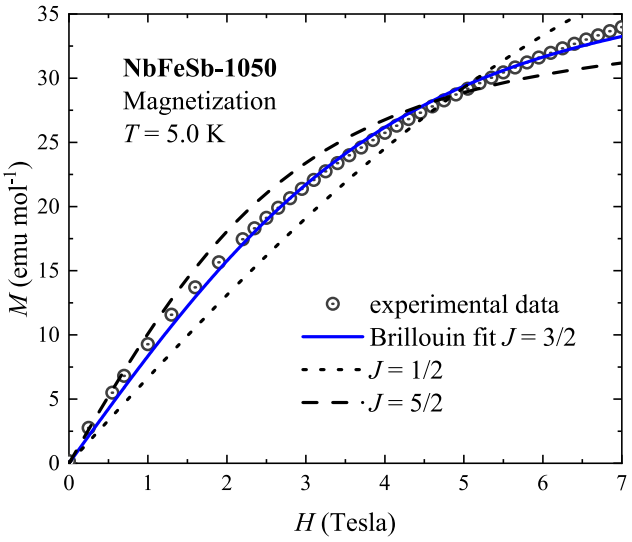

Figure 4.2: Sample NbFeSb-1050 magnetization *vs* magnetic field measured at 5 K. Brillouin function fit is shown with $J = 1/2$ and $J = 5/2$ curves for comparison. Error bars are too small to be seen.

a hole effective mass of $2\,m_e$ [119] and a dielectric constant $\epsilon = 30$ similar to that of TiNiSn [120], the Mott condition ($a_B n_c^{1/3} \approx 0.25$) [121] corresponds to a carrier density $n_c = 3 \times 10^{19}$ cm^{-3}.

4.4 Results and Analysis

4.4.1 Magnetic measurements

Magnetization *vs* T results proved difficult to separate from a small ferromagnetic response, likely due to a surface oxide, even though representing a several orders of magnitude smaller moment density than the defects discussed below. However, M *vs* H measurements revealed dilute paramagnetic defects, as shown at $T = 5$ K for NbFeSb-1050 in Fig. 4.2. To analyze for the local magnetic moments, data were fit to

$$M = N_A c g J \mu_B B_J(x), \tag{4.1}$$

where N_A is Avogadro's constant, c is the concentration of defects, and $B_J(x)$ is a Brillouin function with $x = \frac{g\mu_B JB}{k_B T}$. Assuming $g = 2$, expected for transition ions, the fitted $J = 1.53$ indicates a single, dominant type of defect with $J = 3/2$. Fixing $J = 3/2$, the fit gave $c = 0.00221$ per for-

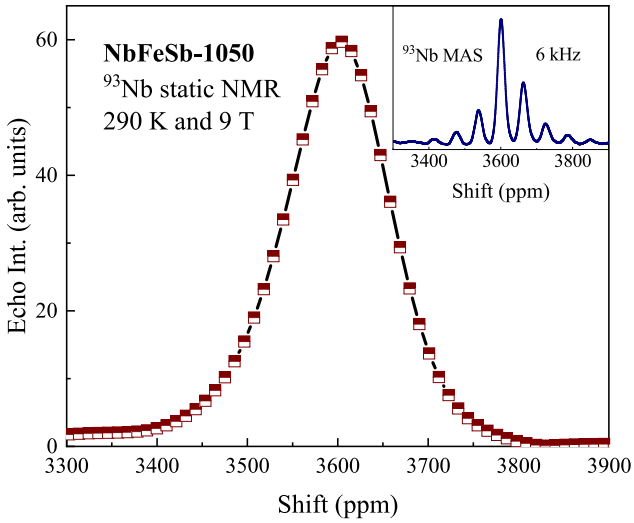

Figure 4.3: ^{93}Nb static NMR spectrum of NbFeSb-1050 at 290 K. Inset: Magic angle spinning spectrum with rotation speed 6 kHz.

mula unit with $g = 2.026$. The corresponding effective moment is $p_{\text{eff}} = g\sqrt{J(J+1)}\mu_B = 3.923$ μ_B.

4.4.2 NMR measurements

4.4.2.1 NMR line shape

The static (stationary sample) 290 K ^{93}Nb NMR spectrum shown in Fig. 4.3 demonstrates a very large shift of 3600 ppm for NbFeSb-1050, which is outside the typical range of Nb chemical shifts [122], presumably due to a large paramagnetic response of Nb *d* orbitals appearing in both the valence and conduction bands. The inset of Fig. 4.3 shows room temperature MAS results, indicating a narrow intrinsic line with no sign of splitting or inhomogeneous broadening, an indication that the site occupations are well ordered, with few local atomic interchanges [21, 123, 124]. To further examine whether there could be a small peak within the observed resonance, corresponding to additional local Nb environments such as reported for Mg on octahedral sites in half-Heusler MgAgAs in Ref. [124], I examined the first moment of the static line measured in the MAS probe. Its position is identical to that of the MAS isotropic peak, to less than the 1 ppm first moment uncertainty. Thus there is no evidence for any significant population of Nb atoms located on such

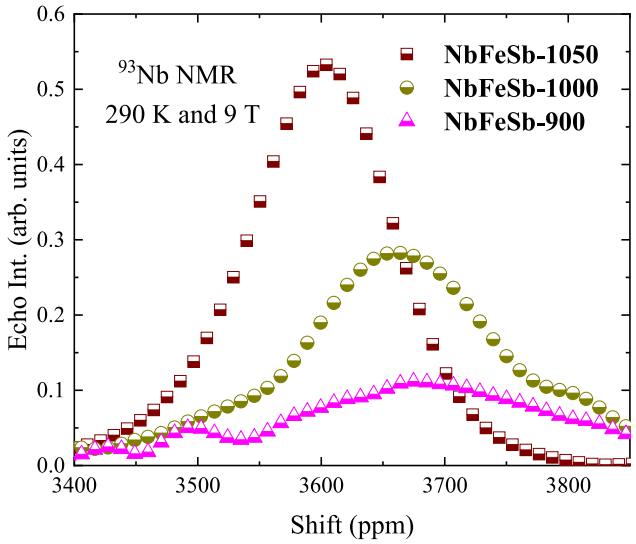

Figure 4.4: ^{93}Nb static NMR spectra of NbFeSb samples prepared in hot pressing temperatures 1050, 1000, and 900 °C, normalized to sample mass.

additional sites, with a detection limit for these measurements on order of 1%.

Line shapes of all samples are shown in Fig. 4.4 with shifts increasing to 3680 ppm for NbFeSb-900. The inset of Fig. 4.5 shows the center of mass shift *vs* T for the NbFeSb-1050 sample. At low temperatures there is a decrease corresponding to the interaction of carriers with the localized defects, and at high temperatures the increase corresponds to an enhanced Knight shift (see Discussion section).

In cubic NbFeSb, I expect no quadrupole shifts for an ideal crystal. However, spectral amplitudes at 290 K vary considerably between samples (Fig. 4.4), with the observed NbFeSb-900 line smaller by a factor 4.8 (scaled according to sample mass) than for NbFeSb-1050. This is close to the factor of $[I(I+1)+1/4]^{1/2} = 5$ for the central transition ($m = 1/2$ to -1/2) for I = 9/2 ^{93}Nb, as the quadrupole satellite resonances collapse toward the central transition; see for example Ref. [125]. This indicates that random electric field gradients due to lattice strains are significantly reduced in sample NbFeSb-1050.

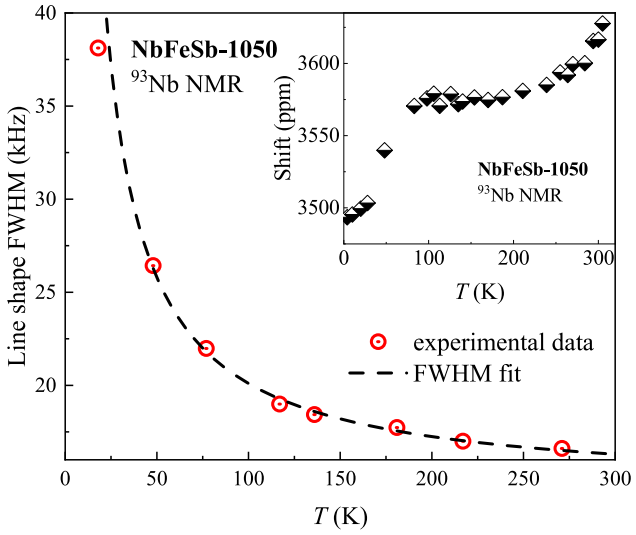

Figure 4.5: Variation of ^{93}Nb FWHM line width *vs* temperature for NbFeSb-1050. Dashed line: Curie-like function fitted as described in the text. Inset: shift *vs* temperature.

4.4.2.2 NMR line width

The low-temperature broadening of the ^{93}Nb NMR lines also supports the magnetic defect picture described above. To probe this behavior, the full width at half maximum (FWHM) was recorded *vs* temperature. The results correspond to a Curie-type behavior as shown in Fig. 4.5. With no associated Curie-law shifts, this corresponds to the effect of dilute paramagnetic defects.

Walstedt *et al.* [126] calculated such effects. For the case where fluctuation of the impurity spins is rapid compared with the NMR splittings, the line width is proportional to the average spin moment. According to this theory, substitutional defects having spin quantum number J and concentration c will produce a FWHM, $\Delta\nu$, which can be expressed [126, 127],

$$\Delta\nu = \frac{2}{9\sqrt{3}} \frac{c\gamma_n g\mu_B}{V} \langle S_z(T)\rangle, \tag{4.2}$$

where $\langle S_z(T)\rangle = \frac{g^2 J(J+1)\mu_B B}{3k_B T}$ is the average spin component in the field direction, and V is the volume per formula unit. I used $g = 2$ and $J = 3/2$, obtained from magnetic measurements. The fit *vs* T, shown in Fig. 4.5, yields an impurity concentration of 0.0022 with a T-independent background 14.4 kHz. These results are consistent with results from the other methods, and confirm

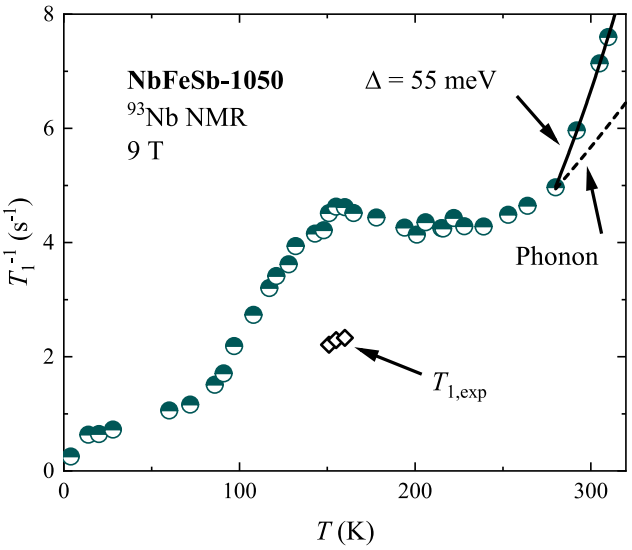

Figure 4.6: Temperature dependence of ^{93}Nb spin-lattice relaxation rates, along with $T_{1,\mathrm{exp}}$ obtained as described in the text. Error bars are approximately the size of the symbols.

that the defects are randomly distributed in the sample.

4.4.2.3 Spin-lattice relaxation

T_1^{-1} results from saturation-recovery experiments are shown in Fig. 4.6, obtained from fitting a recovery curve $M(t) \propto e^{-(t/T_1)^\beta}$, setting $\beta = 1$. Alternatively, allowing β to vary yielded $\beta \approx 1$ near room temperature and at low temperatures, but smaller values in the vicinity of the peak, for example $\beta = 0.85$ at 155 K. This result is consistent with a contribution due to fluctuating defects, with the peak occurring when the maximum in the fluctuation spectrum matches the NMR frequency, as also observed in other Fe-containing Heusler alloys [128].

If nuclear spin-diffusion is not important, relaxation due to uncorrelated local moments is found to approach a stretched exponential, $M(t) \propto e^{(-t/\tau_1)^{1/2}}$. This occurs because of an inhomogeneous distribution of local relaxation rates. For a concentration c per unit volume of effective moments p, the exponential factor is [129],

$$\tau_1^{-1/2} = 4.7 \frac{p\mu_B\gamma_n c}{\sqrt{\omega}} \left(\frac{\omega\tau_c}{1+\omega^2\tau_c^2} \right)^{1/2}, \tag{4.3}$$

where ω is the NMR frequency, and a single Debye-type correlation time τ_c has been assumed to apply to the local moments. When $\omega = \tau_c^{-1}$, a maximum of τ_1^{-1} is reached,

$$(\tau_1^{-1})_{\max} = 11.05\frac{p^2\mu_B^2\gamma_n^2c^2}{\omega}. \tag{4.4}$$

For the concentration 0.0022 per formula unit of defects detected here, this yields, $(\tau_1^{-1})_{\max} = 1.5$ s^{-1}.

Since the paramagnetic fluctuation peak sits atop an overall increase in T_1^{-1} *vs* T, I assumed a relaxation function for each T given by $M(t) = M_0 \exp(-t/T_{1,\exp}) \sum_i c_i \exp[-t/(T_{1s})_i]$, where $\exp(-t/T_{1,\exp})$ is the overall exponential relaxation function, c_i and $(T_{1s})_i$ represent a continuous distribution generating the stretched function $\exp[-(t/\tau_1)^{1/2}]$. I obtained a numerical summation equivalent to the latter distribution, scaled by a single parameter corresponding to τ_1, and fitted the relaxation data to obtain $T_{1,\exp}$ and τ_1 near the observed peak (See Appendix A). Results agree with the calculated $\tau_1^{-1} = 1.5$ s^{-1} within experimental error, so to better identify the underlying exponential behavior I fixed $\tau_1^{-1} = 1.5$ s^{-1}, and fitted for $T_{1,\exp}$ at three temperatures close to the maximum position. This yielded the results 2.21(11), 2.29(16) and 2.33(12) s^{-1}, at 151, 155 and 160 K respectively, also plotted in Fig. 4.6. As described in the Discussion, these agree with a Korringa process for the overall relaxation term, as expected in the case of sufficient carrier density to produce metallic behavior.

At the upper end of the temperature range, both K and T_1^{-1} show a rapid increase. Normally, due to phonons, T_1^{-1} approaches a T^2 behavior [130] (dashed curve in Fig. 6), with little effect on the NMR shift. Instead, the T_1^{-1} data could be fitted to

$$T_1^{-1} = CT^2e^{\Delta/k_BT}, \tag{4.5}$$

with $\Delta = 55$ meV. Setting $\Delta = E_g/2$, this is the expected function [131] for an intrinsic semiconducting regime, however this assumes a gap (E_g) much larger than kT, with the chemical potential (μ) close to the mid-gap. Starting in the metallic regime with μ at the band-edge, Δ

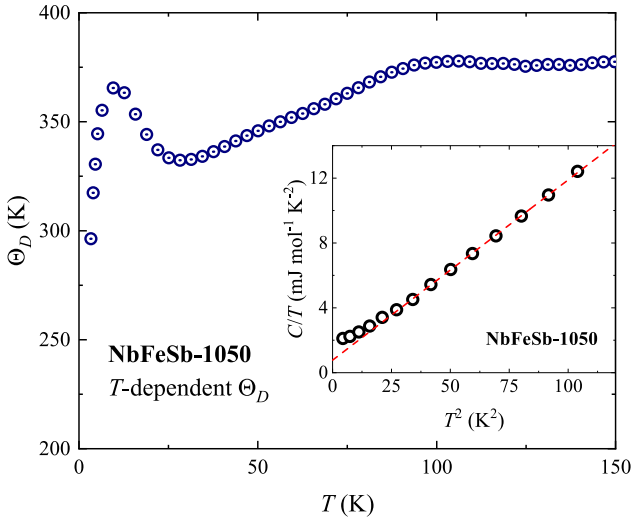

Figure 4.7: Debye temperature extracted from NbFeSb-1050 specific heat, for $H = 0$ T. Inset: C/T *vs* T^2 between 2 and 10 K, with fit described in the text.

should be closer to E_g, and in numerical simulations for various band-edge effective masses the observed steep rise in T_1^{-1} was consistent with E_g of approximately 0.03 eV. With computed band gaps [6, 29, 119, 132–134] in the range 0.51-0.78 eV, and an activated electrical conductivity corresponding to $E_g = 0.51$ eV identified above 600 K [29], it is unlikely that the NMR result corresponds to the entire gap. Therefore, I conclude that this activation energy corresponds to an isolated impurity band within the NbFeSb gap.

4.4.3 Specific heat

Specific heats of the NbFeSb-1050 and NbFeSb-900 samples were measured from 1.8-300 K in magnetic fields H = 0, 5 and 9 T. The zero-field C/T *vs* T^2 below 11 K for NbFeSb-1050, shown in the inset of Fig. 4.7, shows linear behavior with a small upturn at low temperature. The upturn may be due to local moment interaction with carriers. A fit to $C/T = \gamma + \beta T^2$ yields $\gamma = 0.77$ mJ mol^{-1} K^{-2} and $\beta = 0.11$ mJ mol^{-1} K^{-4}. The Debye temperature obtained from $\Theta_D = (12nR\pi^4/5\beta)^{1/3}$, where n is the number of atoms per formula unit and R is the ideal gas constant, is $\Theta_D = 375$ K. A similar fit for NbFeSb-900 yields $\gamma = 1.21$ mJ mol^{-1} K^{-2}.

Fig. 4.7 shows the Debye temperature fitted by solving the standard integral equation,

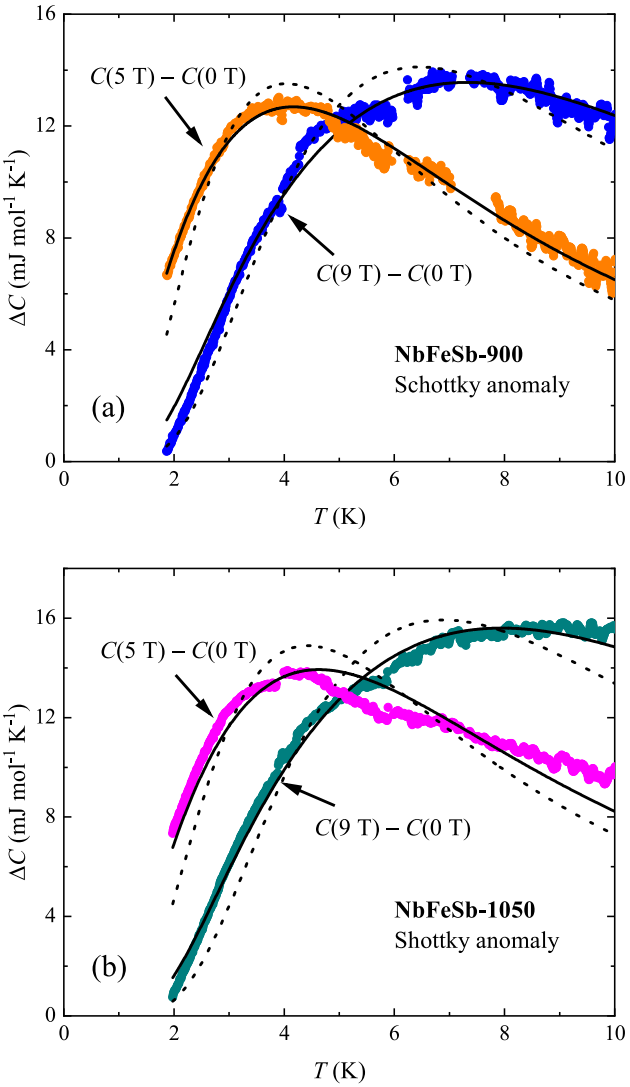

Figure 4.8: (a) NbFeSb-900 and (b) NbFeSb-1050 specific heat differences *vs* T. Solid curves: H = 5 and 9 T $J = 3/2$ multilevel Schottky anomalies; dotted curves: $J = 1/2$ fits for comparison.

$$C = 9nR\left(\frac{T}{\Theta_D}\right)^3 \int_0^{\Theta_D/T} \frac{x^4 e^x}{(e^x - 1)^2} dx, \tag{4.6}$$

As shown, there is a plateau of Θ_D about 375 K, consistent with the low-temperature results and other reports [118].

Field-dependent results for NbFeSb-900 and NbFeSb-1050 yield a small low-temperature difference shown in Fig. 4.8(a) and 4.8(b), subtracting the 0 T from 5 T and 9 T data. For independent moments with $J \neq 1/2$, the corresponding specific heat anomaly is generalized to the multilevel

Table 4.1: Specific heat fitting parameters, with $J = 3/2$, and c per formula unit.

NbFeSb	ΔC	g-factor	c
1050	C(5 T) − C(0 T)	2.159 ± 0.007	0.00225 ± 0.00005
1050	C(9 T) − C(0 T)	2.058 ± 0.003	0.00253 ± 0.00003
900	C(5 T) − C(0 T)	1.941 ± 0.003	0.00205 ± 0.00002
900	C(9 T) − C(0 T)	1.897 ± 0.004	0.00219 ± 0.00003

Schottky function [135]:

$$C_m = cR\left[\frac{x^2 e^x}{(e^x-1)^2} - \frac{[(2J+1)x]^2 e^{(2J+1)x}}{(e^{(2J+1)x}-1)^2}\right], \tag{4.7}$$

where $x = \frac{g\mu_B H}{k_B T}$. With $J = 3/2$, this function provided good agreement. Curves for $J = 1/2$ corresponding to a standard two-level Schottky function are also shown in Fig. 4.8, however the goodness of fit is not as favorable. Fitted results are shown in Table 4.1.

4.5 Discussion

According to first principles band structure calculations, NbFeSb is predicted to be a narrow-gap semiconductor, with an indirect gap in the range 0.51-0.78 eV [6, 29, 119, 132–134], up to 1.77 eV reported by Çoban *et al.* [136]. The properties observed here can be interpreted by the following picture: the as-grown material is nonmagnetic with a 0.2% paramagnetic defects per formula unit in a *p*-type matrix. A consistent measurement of the defect concentrations is provided by different methods, as summarized in Table 4.2. The transport properties observed here are similar to those of the unsubstituted material reported in Ref. [118], and thus I expect that this behavior is typical for native defects in NbFeSb.

The narrow observed NMR line widths, and collapse of the quadrupole-split satellites in the highest-temperature processed sample NbFeSb-1050, demonstrate that samples prepared this way are very well ordered. The unchanging lattice constant *vs* processing conditions indicates little

Table 4.2: Summary for NbFeSb-1050 by different methods.

method	defect concentration (per formula unit)
Magnetization	0.00221
NMR FWHM	0.00223
Specific heat[1]	0.00253

[1]From $C(9\text{ T}) - C(0\text{ T})$.

or no variation in composition, while the NMR quadrupole broadening process is very sensitive to site-occupation disorder. As shown above, the NMR shift results indicate a single local environment for Nb, precluding the presence of a large concentration of Nb antisites or similar defects. This also agrees with results [118] limiting NbFeSb to a narrow composition region of the ternary phase diagram, and with stabilization according to the 18-electron rule for half-Heusler compounds [4–8].

To better understand the temperature-dependence of the NMR results identified for NbFeSb-1050, note that the NMR shift (inset of Fig. 4.5) consists of a sum of the chemical shift (δ), due to the orbital susceptibility, and the Knight shift (K), connected to the paramagnetic spin susceptibility [137], with K the most important source of T dependence. With the valence band (VB) edge dominated by Fe and Nb *d* orbitals [119,132,133], K would be due to core-polarization, with a negative sign [138] for Nb. Based on the linear heat capacity at low temperatures, the degenerate statistics result [139] $\gamma = \frac{\pi^2}{3} k_B^2 g(\epsilon_F)$ gives a Fermi level density of states $g(\epsilon_F)$ = 0.33 states/eV per formula unit. Using the room-temperature Hall-derived hole density $n_h = 9 \times 10^{19}$ cm^{-3}, and an effective mass approximation [139] for which $g(\epsilon_F) = \frac{3}{2}(n_h/\epsilon_F)$ and $\epsilon_F = \frac{\hbar^2}{2m^*}(3\pi^2 n_h)^{2/3}$, I obtain $m^* = 3.4\, m_e$ and a Fermi temperature $T_F = 250$ K. The effective mass is close to computed values, for example 4.5 m_e based on mBJ-based DFT [119], distributed among 4 degenerate VB maxima at the L position in *k*-space and out results (4.9 m_e) described in Chapter 5.

In absence of correlation effects, in terms of the Pauli susceptibility (χ_P), the Knight shift

is given by $K = H_{\rm HF}\chi_P/\mu_B = H_{\rm HF}\mu_B g\epsilon_F$. Here $H_{\rm HF}$ is the hyperfine field, assumed equal to -21 T for ^{93}Nb polarization [138]. Also for degenerate carriers in a Fermi gas picture, the Korringa relation [137], $\kappa_{\rm KP} \equiv K^2T_1T = (\hbar\gamma_e^2)/(4\pi k_B\gamma_n^2)$, can be used to obtain T_1, where γ_e and γ_n are the electron and nuclear gyromagnetic ratios, respectively. This yields $K = -400$ ppm, and $1/(T_1T) = 0.052$ s^{-1} K^{-1}. Comparing the latter value to $1/(T_{1,\rm exp}T) = 0.015$ s^{-1} K^{-1} for $T \approx 155$ K as described above, this implies that approximately (0.015/0.052)$^{1/2}$ = 50% of the total Fermi level density of states resides in Nb *d* orbitals. DFT calculations [119, 132] display an orbital projection at the VB edge more heavily dominated by Fe-based states, however the result obtained here appears reasonable, and a small enhancement of T_1^{-1} relative to the Korringa relation is not surprising. By contrast, for carriers confined to a separate impurity band, much larger departures from Korringa behavior would be expected [140], with the electronic contribution to the specific heat not expected to be consistent with an effective mass picture. Thus this provides strong evidence that the native holes reside at the VB edge at these temperatures. This is inconsistent with a low-carrier compensated model for NbFeSb, however given the observed mobility, it is likely that there would be a large energy-dependence to the electron scattering rate. This situation can lead to sign changes in the Seebeck coefficient [141], such as have been observed in NbFeSb [117, 118], thus not requiring changes in carrier type.

Scaled according to the Korringa relation, $T_{1,\rm exp}$ derived for 155 K corresponds to $K = -212$ ppm (using $\kappa_{\rm KP} = 3.05 \times 10^{-6}$ s K for ^{93}Nb). Assuming the corresponding chemical shift, $\delta = 3790$ ppm is temperature independent, I obtain K *vs* temperature shown as the absolute value in Fig. 4.9. Also shown in this figure is the quantity and $(\kappa_{\rm KP}/T_1T)^{1/2}$, which tracks K when the Korringa relation holds. This occurs for temperatures below 80 K where the additional dilute paramagnetic contribution to T_1^{-1} disappears, although below 20 K the curves diverge, with T_1^{-1} assuming an approximate $T_1^{1/2}$ behavior. The latter is consistent with Kondo interactions above the Kondo temperature [142, 143], thus it appears that the low-temperature behavior is dominated by carriers interacting with the observed local moments.

Note that based on an extrapolation of results from Ti$_x$-substituted materials (Chapter 5), I ob-

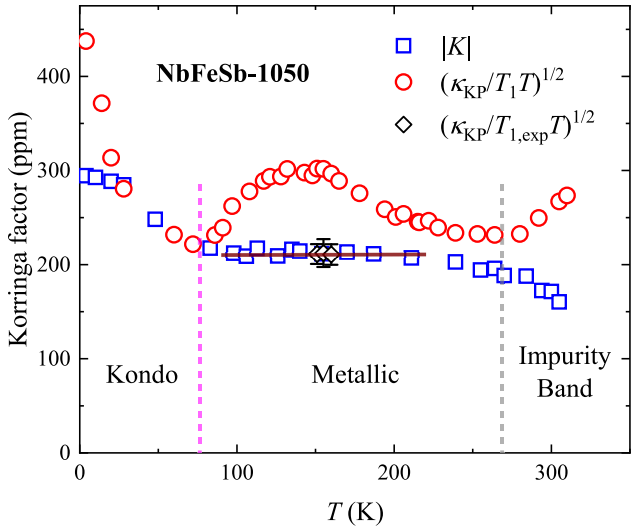

Figure 4.9: Dimensionless Korringa factor *vs* T for sample NbFeSb-1050, with $\kappa_{\rm KP}$ denoting the theoretical Korringa product.

tained a slightly larger $\delta \cong 4020$ ppm. Thus, the assumption used here of an unmodified Korringa product yields a somewhat reduced K, but aside from this difference the general results obtained by these methods are consistent.

As noted above, the activated upturn in T_1^{-1} above 280 K must be associated with an impurity band. In the low-temperature regime, since the Fermi level is located in the VB, this impurity band is empty. With the enhancement of thermopower between 300 and 600 K indicating additional holes excited into the VB [29], the impurity band thus must be located just above the VB maximum. The positive sign of the increased NMR shift at these temperatures is presumably due to impurity band defects having Nb s-character, given the positive Fermi contact hyperfine field [144].

Considering the nature of the observed defects, Fe antisites on Nb sites appear to be a likely explanation for the observed dilute magnetic defects: the smaller Fe ion has 3 electrons beyond the 5 needed for hybridization on that site. According to crystal field theory, the spin-only magnetic moment of Fe in tetrahedral environment adopts a high-spin $\mu_{\rm so} = \sqrt{4S(S+1)}\mu_B = 3.87\ \mu_B$ with $S = 3/2$. However, this defect would be charge-neutral, so that other defects are needed to explain the observed hole doping. As shown in Ref. [144], an impurity band due to Ni interstitials can explain the gap anomaly in 18-electron ZrNiSb, and by analogy it may be that Fe on the half-

Heusler interstitial sites form a separate impurity band giving the observed $\sim$0.03 eV activation gap. This band can provide more carriers with increasing temperature, thus explaining the sharp increase of Seebeck coefficient above room temperature [29]. The other likely defect candidate is Nb antisites on Fe sites. Since Nb has 3 fewer valence electrons, and could thus act as a triple acceptor, and such acceptors can pull the chemical potential into the VB and lead to *p*-type metallic behavior at low temperatures. The high resistivity and low mobility of unsubstituted NbFeSb [117, 118] can thus be explained by scattering from Nb antisites resonant with the VB.

4.6 Summary

In this chapter, various techniques including ^{93}Nb NMR, magnetic and specific heat measurements were applied to measure the half-Heusler semiconductor NbFeSb. The results show a high degree of atomic order, with defects limited to a small density, including a 0.2% uniformly distributed native magnetic defect in NbFeSb samples, likely due to Fe antisites on Nb sites. The NMR shift and spin-lattice relaxation results are consistent with heavily doped *p*-type behavior at low temperatures. The results include a Korringa-type NMR response below 200 K, with constant Knight shift, and a Kondo-related behavior below 80 K due to the interaction of carriers and local moments. Above 280 K, the enhanced Knight shift and T_1^{-1} indicate increased carrier density across a very small gap of about 0.03 eV. Based on this and previously reported transport results, it can be concluded that this response is associated with an empty impurity band due to acceptor states located a small distance above the valence band maximum, with native *p*-type doping giving the low-temperature metallic behavior.

5. THERMOELECTRIC HALF-HEUSLERS $Nb_{1-x}Ti_xFeSb$*

5.1 Introduction

In this chapter, to analyze the underlying electronic and magnetic properties of $Nb_{1-x}Ti_xFeSb$ as Ti(x) ($x = 0.05, 0.1, 0.2, 0.3$), ^{93}Nb and ^{121}Sb NMR and ^{57}Fe Mössbauer measurements were done as local probes for all sites aiming at a better understanding of these materials. All half-Heusler samples were prepared by Dr. Ren's group at University of Houston. The DFT was conducted by my labmate Dr. Nader Ghassemi and I measured all the experimental results.

5.2 Sample Preparation

Raw elements (Nb pieces, 99.9%, and Sb broken rods, 99.9%, Atlantic Metals & Alloy; Fe granules, 99.98%, and Ti foams, 99.9%, Alfa Aesar) were weighed stoichiometrically, and arc melted multiple times to form uniform ingots. The ingots were then ball milled (SPEX 8000M Mixer/Mill) for 3 h under Ar protection to produce nanopowders. The powders were then consolidated into disks via hot pressing at 80 MPa for 2 min at 1373 K. This process has been shown to yield uniform samples with high power factors [29]. In this work, I denote $Nb_{1-x}Ti_xFeSb$ as Ti(x) ($x = 0.05, 0.1, 0.2, 0.3$), the same samples as prepared in Ref. [29]. I also studied an unsubstituted sample, which is one of the samples described previously in Ref. [15] (Chapter 4), annealed at 1323 K (sample NbFeSb-1050).

5.3 Experimental and Computational Methods

Substitution fractions, actual compositions and carrier concentrations of all samples are listed in Table 5.1. Half-Heusler materials normally follow an 18-electron stability rule, and NbFeSb satisfies this criterion and is found to be a semiconductor. Cation substitution in the range ($Nb_{1-x}Ti_x$) leads to heavily p-type samples because Ti lacks one electron compared with Nb. In these samples, room-temperature carrier concentrations were determined by Hall measurements [29] and shown

*Part of this chapter is reprinted from Ref. [145] (Y. Tian, F. G. Vagizov, N. Ghassemi, W. Ren, H. Zhu, Z. Wang, Z. Ren, and J. H. Ross, Jr., "Defect charging and resonant levels in half-Heusler $Nb_{1-x}Ti_xFeSb$," Mater. Today Phys., vol. 16, p. 100278, 2021.) with permission from Elsevier.

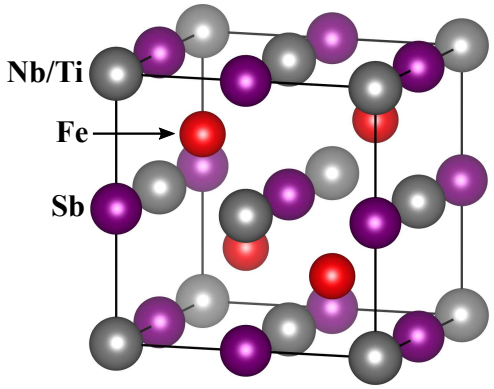

Figure 5.1: Crystal structure of Ti-substituted half-Heusler $Nb_{1-x}Ti_xFeSb$, showing site occupations.

Table 5.1: $Nb_{1-x}Ti_xFeSb$ nominal substitution fraction x, sample label used in the text, actual composition from microprobe analysis, measured room-temperature hole concentration (p) from Hall measurements and theoretical hole concentration (p_{theo}) along with their ratio.

x	label	Actual composition	p (10^{20} cm^{-3})	p_{theo} (10^{20} cm^{-3})	p/p_{theo}
0	NbFeSb-1050	NbFeSb[1]	0.9[1]	-	-
0.05	Ti(0.05)	$Nb_{0.94}Ti_{0.05}Fe_{1.01}Sb_{0.99}$[2]	8.1[2]	9.5	0.85
0.1	Ti(0.1)	$Nb_{0.89}Ti_{0.1}Fe_{1.00}Sb_{0.99}$[2]	15.2[2]	19	0.80
0.2	Ti(0.2)	$Nb_{0.8}Ti_{0.2}Fe_{1.02}Sb_{0.99}$[2]	25.7[2]	38	0.68
0.3	Ti(0.3)	$Nb_{0.69}Ti_{0.3}Fe_{1.02}Sb_{0.98}$[2]	30.3[2]	57	0.40

[1]From Ref. [15]. (Chapter 4)
[2]From Ref. [29].

to be *p*-type as expected, with larger hole concentration for larger *x*; however, the ratio of the measured charge density to the theoretical charge density becomes smaller with larger *x* as further discussed below.

Magnetic measurements were performed using a Quantum Design MPMS superconducting quantum interference device magnetometer. ^{93}Nb and ^{121}Sb NMR experiments were carried out by applying a custom-built pulse spectrometer at a fixed magnetic field 9 T using shift standards $NbCl_5$ and $KSbF_6$ in acetonitrile respectively, with positive shifts here denoting paramagnetic sign. Shift is calculated by $\Delta\nu/\nu_0$ where $\Delta\nu = \nu - \nu_0$ is the deviation from the standard reference frequency, ν_0, determined by the shift standard. Mössbauer spectra were measured in the temperature range 7-323 K on a conventional constant acceleration spectrometer (WissEl) equipped with a Co-57 source in rhodium matrix 35 mCi in activity. Samples were prepared from fine powders, mixed with BN powder and uniformly distributed as a thin layer with density 18 mg of NbFeSb per cm^2 (3.12 mg of Fe per cm^2) over an MB-PAH-1 sample holder (WissEl) for room-temperature measurements. Above and below room temperature, a boron nitride MBF-BND sample holder (WissEl) was used with identically prepared samples, while above room temperature, the sample had a slightly smaller powder density ($\sim$13 mg of NbFeSb per cm^2). For low-temperature measurements, the samples were mounted on the cold finger of a helium continuous-flow cryostat (CFICEV-MOSS, ICE Oxford, UK), with temperatures controlled within ± 0.5 K over the whole temperature range. Above room temperature MBF-1100 Mössbauer furnace (WissEl) was used. Isomer shifts are referred to α-Fe at room temperature.

Density functional theory (DFT) calculations were performed with WIEN2k [113] using the Perdew, Burke, and Ernzerhof (PBE) exchange-correlation potential, a k-point grid of $10 \times 10 \times 10$, and lattice constants from experimental values [15]. In calculations not including spin-orbit coupling, a semiconducting gap of 0.54 eV was obtained for NbFeSb. This can be compared to 0.51 eV obtained from high-temperature transport measurements [29]. For the VB maximum at the L point, I also obtained an effective mass $m_{\text{eff}} = 4.9\, m_e$ by fitting the calculated density of states within 0.1 eV of the band edge. For ^{93}Nb NMR chemical shifts the zero offset was calibrated by

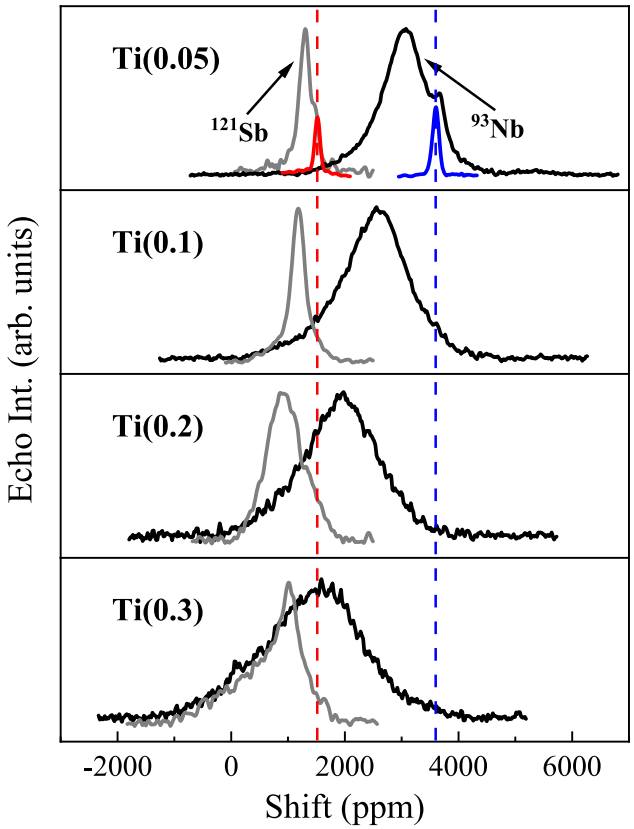

Figure 5.2: Room-temperature ^{93}Nb (black) and ^{121}Sb (gray) NMR line shapes for Ti(x) ($x = 0.05, 0.1, 0.2, 0.3$) samples. The previously reported ^{93}Nb spectrum of NbFeSb (sample NbFeSb-1050) [15] is shown as a solid curve for comparison, and ^{121}Sb spectrum is also shown for the same sample, with dashed lines indicating the center positions.

a separate shift calculation for $LaNbO_4$ and for $YNbO_4$, and then adjusted based on the previously reported shifts [146] to the standard reference ($NbCl_5$ in acetonitrile). Since chemical shift are less well studied for ^{121}Sb, we did not find a comparable solid compound with which to calibrate the computational ^{121}Sb zero offset. We also performed similar calculations with spin-orbit coupling included, giving relative little change in the results – for example, the effective mass increases from 4.9 to 5.0 m_e, while the calculated ^{93}Nb chemical shifts changed by less than 60 ppm.

5.4 Experimental Results

5.4.1 NMR measurements

5.4.1.1 Line shapes

Fig. 5.2 shows ^{93}Nb and ^{121}Sb NMR line shapes for the Ti(x) samples obtained from the fast Fourier transform using a standard spin echo sequence. Also superposed are resonances for the $x = 0$ sample NbFeSb-1050 with a much smaller room-temperature carrier concentration ($p = 9 \times 10^{19}$ cm^{-3}) [15]. It can be seen from the superposed spectra that there is a small signal due to pure-phase NbFeSb, appearing only in the Ti(0.05) substituted sample. The resonances for both nuclei become broader and move to lower frequencies when the substitution fraction increases.

The increasing line width *vs* x is due to a superposition of local environments at Nb and Sb sites. For Nb, the first and second neighbor shells are composed of Fe and Sb ions respectively, so it is only starting with the third shell that the (Nb, Ti) substitution produces a distribution of local environments. Correspondingly, for Sb the first neighbor shell consisting of Fe ions is fixed, while the second neighbors include a distribution of (Nb, Ti) ions. This leads to relatively symmetric local environments, with a large number of (Nb, Ti) configurations contributing to the observed line widths. Since the widths scale nearly proportionally to the changes in shift relative to NbFeSb, with Sb widths and shifts considerably smaller, I surmise that the widths, as well as the asymmetry seen for Ti(0.3), are due to a quasi-random superposition of chemical and Knight shifts. As quadrupolar nuclei, it is possible for a second-order quadrupole contribution to affect the mean shift; however, this contribution should be small. For example, Nb oxides having a nearly symmetric first-neighbor shell are found to have ^{93}Nb quadrupole parameters ν_Q less than 1 MHz [146], which would yield [137] a mean shift contribution of about 50 ppm. This is 2% of the mean shift for the Ti(0.3) sample, and is presumably an upper limit, so I neglect such contributions in analyzing the relative shifts.

5.4.1.2 Shifts

^{93}Nb and ^{121}Sb shifts for all samples, measured at room temperature, are shown in Fig. 5.3(a).

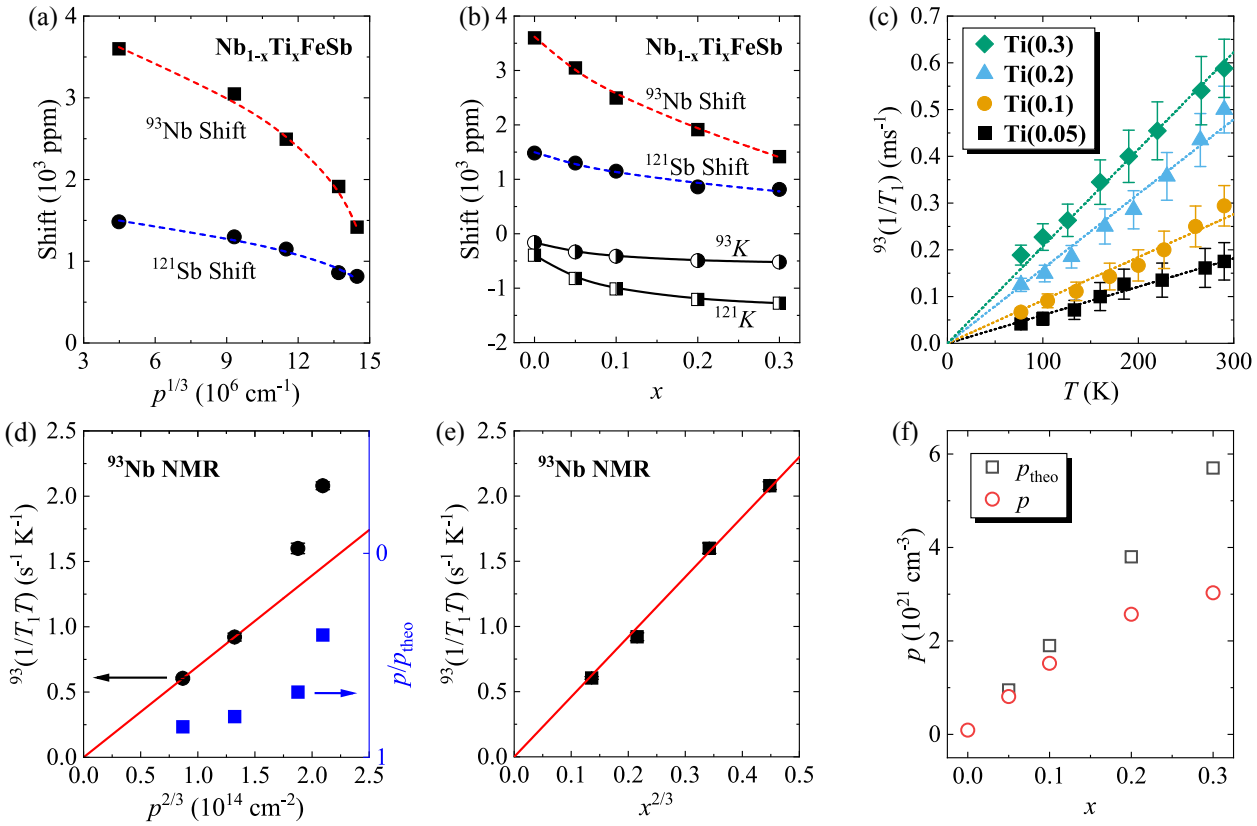

Figure 5.3: (a) $Nb_{1-x}Ti_xFeSb$ center-of-mass ^{93}Nb and ^{121}Sb shifts *vs* $p^{1/3}$ at room temperature, where p is the measured hole density. Dashed lines are the fits to the data described in the text. (b) The same data and fits as (a) but plotted *vs* Ti content x. The Knight shift parts of the fit are also included. (c) Temperature dependence of ^{93}Nb relaxation rates in Ti(x) samples, indicated by squares, circles, triangles, and diamonds for $x = 0.05, 0.1, 0.2, 0.3$ respectively, with fits to metallic behavior as described in the text. (d) $^{93}(1/T_1T)$ from the linear fits shown in (c) *vs* $p^{2/3}$. Straight line corresponds to carriers filling a parabolic band, fitted to the two lowest points. Also shown: $p/p_{\rm theo}$ *vs* $p^{2/3}$, where $p_{\rm theo}$ is the theoretical hole concentration expected from the composition. (e) $^{93}(1/T_1T)$ *vs* $x^{2/3}$ with a linear fit. (f) Room-temperature p and $p_{\rm theo}$ *vs* Ti content x.

These are the center-of-mass isotropic positions of the measured spectra defined as the intensity-weighted average shifts, thus corresponding to the mean shift of the observed nuclei. Note that the Ti(0.05) shift is also a center-of-mass shift, however with the small peak due to unsubstituted phase removed. The spectrum was fitted using two Lorentzian peaks, and the extra small peak was subtracted, after which the remaining spectrum was used for shift calculation. These shifts can be considered as a sum of the Knight shift (K) due to the susceptibility of the charge-carrier spins and the chemical shift (δ) due to the local orbital susceptibility. For samples sufficiently doped to exhibit metallic behavior, K is given generally as,

$$K = \frac{H_{\mathrm{HF}}\chi_P}{\mu_B}, \tag{5.1}$$

where H_{HF} is the relevant hyperfine coupling field constant, μ_B is Bohr magneton, and χ_P is the Pauli electron spin susceptibility per atom, $g(E_F)(g_{\mathrm{eff}}/2)\mu_B^2$ for weakly-interacting electrons. g_{eff} is the effective g-factor due to spin-orbit coupling, which can modify the energy splitting and also K. For s-character conduction electron states, the dominant hyperfine interaction is Fermi contact. However, with *d* electrons dominant here, the core polarization hyperfine field H_{CP} is the relevant spin coupling with the dipolar spin contribution to K vanishing in cubic symmetry. Note also that I assume spin-orbit coupling effects are small. As a result, K can be expressed as

$$K = g_{\mathrm{partial}}(E_F)(\frac{g_{\mathrm{eff}}}{2})\mu_B H_{\mathrm{CP}}, \tag{5.2}$$

where $g_{\mathrm{partial}}(E_F)$ is the Fermi-level partial density of states for the atom containing the nucleus being measured.

In an effective mass approximation, which is often appropriate for semiconductors, it is found in the metallic limit,

$$g(E_F) = m_{\mathrm{eff}}\frac{(3\pi^2 n)^{1/3}}{\pi^2\hbar^2}V_{\mathrm{f.u.}}, \tag{5.3}$$

where m_{eff} is the thermodynamic effective mass, *n* is the carrier density and $V_{\mathrm{f.u.}}$ is the volume

per formula unit. Thus, substituting Eq. (7.5) into Eq. (7.7), K should scale as $p^{1/3}$. As shown in Ref. [147], the chemical shift (δ) of $Cd_{1-x}Zn_xTe$ is linearly dependent on *x*, indicating a linear relationship between substitution fraction and chemical shift similar to other properties often observed in semiconductor alloys. $\delta(x)$ is thus assumed to be linearly dependent on the substitution fraction of Ti. I therefore model the shift as,

$$(\text{Total Shift}) = K(p) + \delta(x) = A \cdot p(x)^{1/3} + B \cdot x + C \tag{5.4}$$

where $A = \frac{(3\pi^2)^{1/3}}{\pi^2\hbar^2}(\frac{g_{\text{eff}}}{2})m_{\text{eff}}\mu_B H_{\text{CP}}$ and C represents the baseline shift, corresponding to the Fermi level at the mid-gap for pure NbFeSb. The list of hole densities *vs x* is given in Table 5.1, and these are designated here as $p(x)$. Curves shown in Fig. 5.3(a) and (b) correspond to the fits to Eq. (6.1). This yields, for Nb $A = (-0.9 \pm 0.2) \times 10^{-4}$ cm, $B = -4440 \pm 700$ and $C = 4020 \pm 150$; and for Sb $A = (-0.4 \pm 0.2) \times 10^{-4}$ cm, $B = -1200 \pm 600$ and $C = 1660 \pm 130$, all in ppm shift units. The Knight shift contributions (A terms) are also plotted in Fig. 5.3(b), with the remainder corresponding to the chemical shift. For all fitting parameters, B has the largest standard error due to the lack of points for *x* close to 1. Also note, as mentioned above, the Ti(0.05) shift was obtained after subtracting the unsubstituted-phase peak, thus I also considered the fit in absence of this composition. I discovered that removing the Ti(0.05) point only makes very slight changes in the fitting results: the $x = 0$ chemical shifts (parameter C) changed by less than 1%, with the largest difference upon omission of the Ti(0.05) point being a change of B for Sb from -1200 to -1000, which is within the fitting uncertainty. This gives further confidence in the consistency of the results.

While the T_1 results described below allow a more targeted analysis of the carrier behavior, the shift analysis is particularly important in assessing the NbFeSb ($x = 0$) chemical shifts. The fitted results indicate a large ^{93}Nb chemical shift of $\delta \approx 4020$ ppm for NbFeSb, decreasing rapidly *vs x*. The $x = 0$ result is slightly larger than obtained as described in Chapter 4 since here I are able to better separate the chemical shift rather than assuming a fixed Korringa ratio. The ^{93}Nb shift

in NbFeSb is quite large; the calculated chemical shift, with the offset for the reference standard calibrated against $LaNbO_4$ and $YNbO_4$, is $\delta = 3220$ ppm, a considerably smaller value. We also made a similar calculation for the half-Heusler compound NbCoSn, which yielded a ^{93}Nb chemical shift of 2585 ppm, in much closer agreement with the measured value, $\delta = 2849$ ppm [24]. The fitted results also indicate a much smaller reduction in ^{121}Sb chemical shift going from NbFeSb to TiFeSb. The ^{121}Sb shifts calculated using the WIEN2k package decrease by 132 ppm, following the same trend *vs* substitution as the measured results. However, the ^{93}Nb result exceeds the usual range of reported shifts, and here I see that it is significantly larger than obtained by DFT. In Chapter 6 this is explored further, and shown to be a general trend for half-Heusler compounds with large orbital susceptibility.

5.4.1.3 Spin-lattice relaxation rates

The ^{93}Nb spin-lattice relaxation rate, denoted as $^{93}(1/T_1)$, was measured using the inversion recovery method from 77-290 K. The recovery of the ^{93}Nb central-transition magnetization for the case that only the central transition is inverted can be expressed as

$$\frac{M(t) - M(\infty)}{M(\infty)} = -2\alpha(0.152e^{-\frac{t}{T_1}} + 0.14e^{-\frac{6t}{T_1}} + 0.153e^{-\frac{15t}{T_1}} + 0.192e^{-\frac{28t}{T_1}} + 0.363e^{-\frac{45t}{T_1}}). \quad (5.5)$$

Here, $M(t)$ is the measured signal and t the recovery time. Each experimental T_1 value was obtained by a fit to this multi-exponential recovery curve. For all studied compounds, the $^{93}(1/T_1)$ results exhibit a constant T_1T behavior within error bars, indicating a metallic-type relaxation process as shown in Fig. 5.3(c). In the case that an effective mass treatment is appropriate, from an analysis similar to what is given above for K one finds that $1/T_1$ should scale as $p^{2/3}$. As shown in Fig. 5.3(d), $^{93}(1/T_1T)$ follows a linear dependence on $p^{2/3}$ for smaller *p*, although there is an enhancement for large *p*, which is further discussed below. On the other hand, with *p* expected to be proportional to *x* in the case that each Ti donates one hole to the valence band (see Fig. 5.3(f)), I find that indeed the fitted $1/T_1T$ is proportional to $x^{2/3}$, as shown in Fig. 5.3(e). This is an indication that the Hall results do not represent all of the holes in the valence band for large substitution

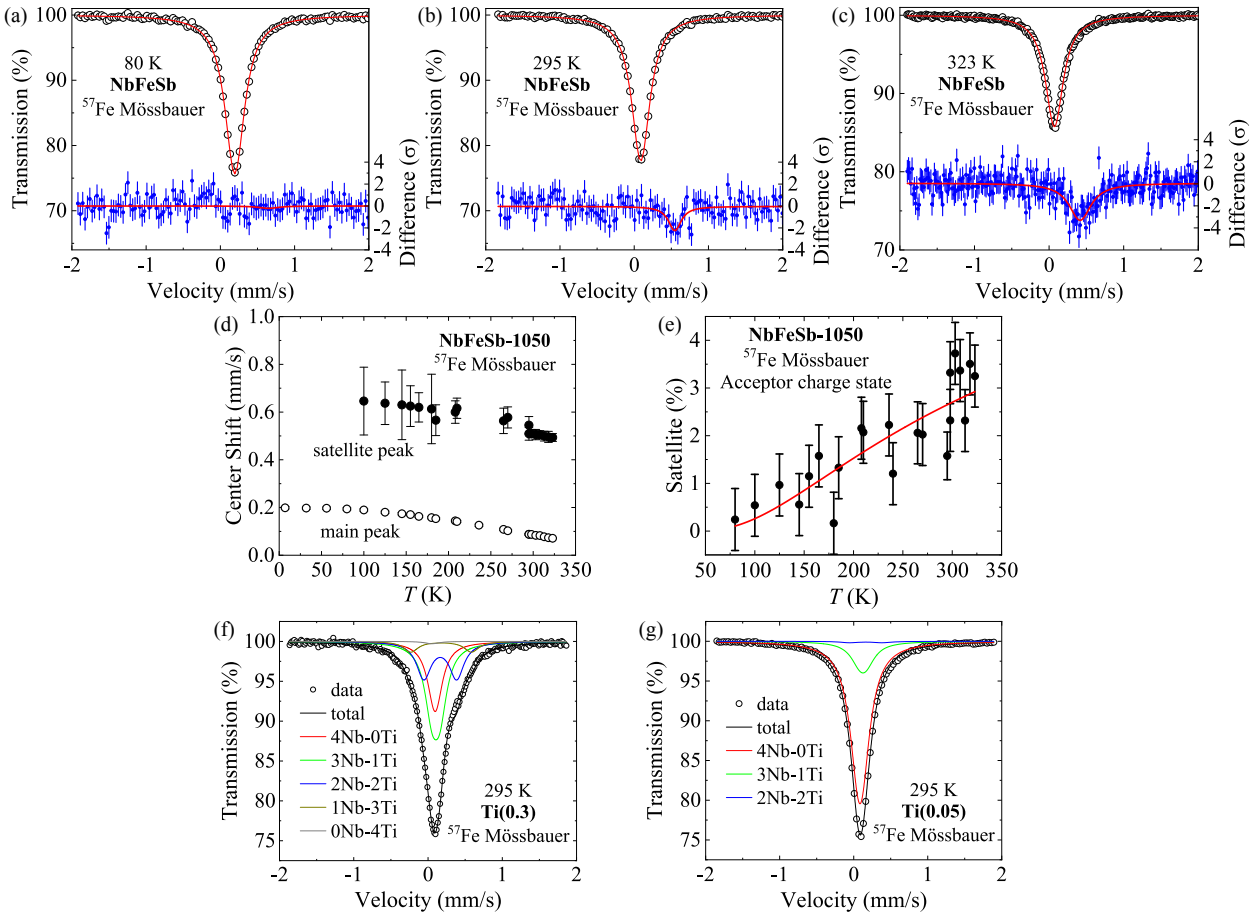

Figure 5.4: (a)-(c) ^{57}Fe Mössbauer spectra for unsubstituted NbFeSb-1050 sample with least-squares fits described in the text (solid curves). Velocities are relative to α-Fe, with error bars too small to be seen. Residuals are also shown below these plots with fitted satellite curves overlaid, relative to the statistical error of the fit. (d) Shift *vs* temperature for the fitted NbFeSb-1050 main peak and satellite peak. (e) Satellite peak relative area *vs* temperature. (f)-(g) ^{57}Fe Mössbauer spectra of Ti(0.3) and Ti(0.05) samples, with fits for neighbor configurations of Fe atoms as shown. 3Nb-1Ti and 4Nb-0Ti configurations have negligible probabilities for Ti(0.05) and are not shown.

levels.

5.4.2 Mössbauer measurements

Figs. 5.4(a)-5.4(c) show Mössbauer spectra for the unsubstituted NbFeSb-1050 sample at 80, 295 and 323 K, respectively. The spectra show no sign of magnetic splitting. Least-square fitting curves are also shown in the figure. The initial fits including one singlet revealed a second satellite peak in the residual plots especially at larger T as shown in Figs. 5.4(a)-5.4(c). Thus, I adopted a

fitting with two Lorentzian lines, including a main peak and a small satellite with about 0.5 mm/s larger shift. The fitted line widths for the main peak are temperature independent at FWHM 0.30 mm/s. The small line widths indicate a lack of inhomogeneous broadening, showing NbFeSb to be well-ordered in the half-Heusler structure. The main line shift is 0.089 mm/s at 295 K, gradually increasing to 0.199 mm/s at 7 K, very similar to the results reported [148] for *n*-type NbFeSb. The T-dependent shift is shown in Fig. 5.4(d). The addition of the satellite yielded a small improvement in the fitting at high temperatures, for example at 323 K, χ^2 improved from 1.25 to 0.92. The fitted satellite positions are also shown in Fig. 5.4(d). Due to the small amplitude of the satellite peak, it was fitted with the same width as the main peak.

The change in amplitude of the fitted satellite *vs* T can be understood as a change in the charge state of a native defect *vs* temperature. Fig. 5.4(e) shows the spectral area of the satellite peak, as a percentage of the total area, corresponding to the relative number of Fe ions affected by these defects. Since the defect identity is not determined [15], the satellite might correspond to either a Fe-centered defect, or immediate Fe neighbors of the defect site, although the lack of quadrupole splitting tends to indicate the former. With a large density of such defects close to the band edge energy, when temperature increases the charge state of these defects can change, as holes are transferred to the valence band, due to excitation of carriers out of the defect level. Accordingly, the result was fit to the acceptor density function [139],

$$N_a^+ = \frac{N_A}{1 + 4 \cdot e^{\Delta/kT}}, \tag{5.6}$$

assuming each neutral acceptor contains two electrons with opposite spins and the state with no electron is prohibited, and where Δ is the energy difference between defect level and chemical potential. The fitting [Fig. 5.4(e)] gives $\Delta = 31 \pm 0.6$ meV and $N_A = 39 \pm 10\,(\%)$ showing maximally around 8% Fe affected by defects. This is in good agreement with the result previously obtained from NMR [15], in which the spin-lattice relaxation rate of NbFeSb also shows a sharp increase close to room temperature, modeled as a large density of shallow defects located about

Table 5.2: Absorption areas, described in text, and the fitted hyperfine parameters for the room-temperature ^{57}Fe Mössbauer spectra of Ti(0.3) and Ti(0.05) samples with the labels referring to $Nb_{1-x}Ti_xFeSb$ (x = 0.3 and 0.05), respectively.

	Absorption area (%)		Isomer shift (mm/s)		Quadrupole splitting (mm/s)	
	Ti(0.3)	Ti(0.05)	Ti(0.3)	Ti(0.05)	Ti(0.3)	Ti(0.05)
4Nb-0Ti	26.5 ± 0.8	81.4 ± 0.6	0.087 ± 0.005	0.085 ± 0.002	0	0
3Nb-1Ti	44.8 ± 0.5	17.1 ± 0.8	0.111 ± 0.003	0.13 ± 0.01	0.105 ± 0.004	0.08 ± 0.01
2Nb-2Ti	19.8 ± 1.0	1.3 ± 1.2	0.173 ± 0.003	0.16 ± 0.10	0.446 ± 0.005	0.4 ± 0.2
1Nb-3Ti	8.0 ± 1.4	-	0.181 ± 0.006	-	0.73 ± 0.01	-

30 meV above the valence band in the *p*-type samples making up an impurity band near the band edge.

Figs. 5.4(f) and 5.4(g) show ^{57}Fe Mössbauer spectra of Ti(0.3) and Ti(0.05) respectively at room temperature. For Fe atoms ($4c$ sites) in $Nb_{1-x}Ti_xFeSb$ alloys, 4 out of 8 nearest-neighbor sites are occupied by mixed Nb and Ti atoms. Therefore, the resulting spectra were modeled as superpositions of peaks for different local configurations of these neighbor ions. The spectra were fit assuming amplitudes corresponding to a binomial distribution,

$$P_n(x) = \frac{4!}{n!(4-n)!} x^n (1-x)^{4-n}, \tag{5.7}$$

for the probability of each $Nb_{4-n}Ti_n$ configuration. For the Ti(0.3) composition, probabilities given by Eq. (5.7) are 24, 41, 26, 7.6, and 0.8%, for $n = 0$ through 4 respectively. However, after first fixing these areas in the fit, I found that the goodness of fit (χ^2) decreased from 1.58 to 0.98 based on slightly modified probabilities equal to 26.5, 44.8, 19.8, 8.0, and 0.9%, for the same neighbor configurations. The results are plotted in Fig. 5.4(f) based on the modified probabilities. The fitting parameters are shown in Table 5.2, omitting the very small $n = 4$ term; widths were held fixed in these fits. The results indicate a reduced probability for the 2Nb-2Ti configuration in favor of the others, which could be an indication of the segregation of Nb and Ti neighbors for larger substitution amounts. On the other hand, for Ti(0.05), the standard binomial probabilities, 81.4,

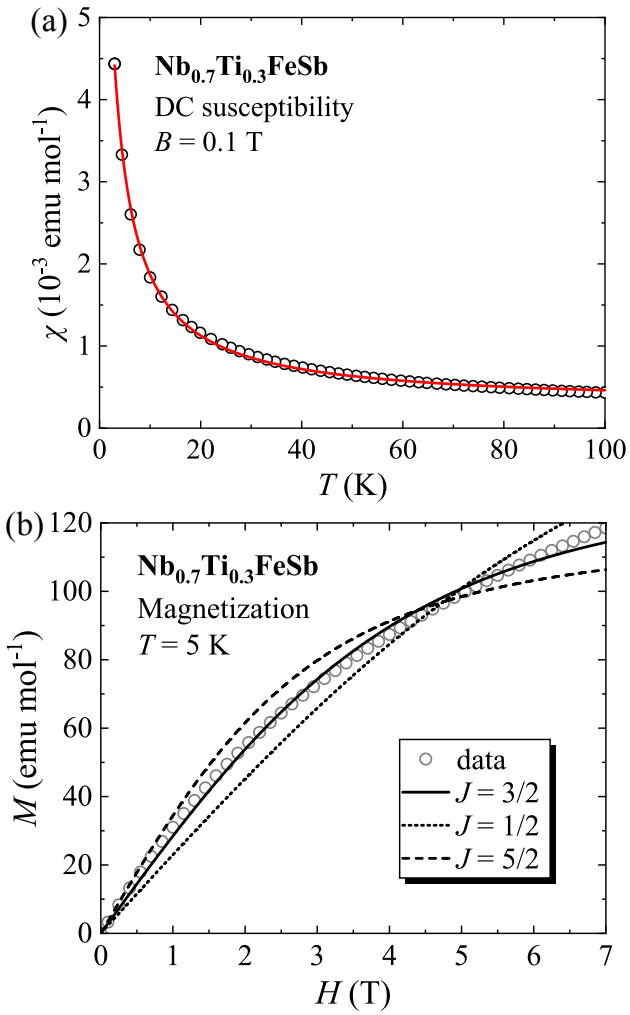

Figure 5.5: Magnetic measurements for sample Ti(0.3). (a) Susceptibility *vs* T from 3 to 100 K with fit described in text. (b) M *vs* H measured at 5 K. $J = 3/2$ Brillouin function fit is shown with $J = 1/2$ and $J = 5/2$ curves for comparison.

17.1, and 1.3% (Table 5.2), with negligible contributions for 3 and 4 neighbors, worked very well in fitting the data. In the fits, the peaks for Fe with Nb-only neighbors (4Nb-0Ti) have very similar center shifts of 0.087 and 0.085 mm/s, and these are very close to the room-temperature shifts for the unsubstituted sample with an identical Fe nearest neighbor configuration. The increasing isomer shift *vs* number of Ti neighbors, shown in the Table 5.2, is an indication of enhanced *d*-electron transfer to Fe in these configurations.

5.4.3 Magnetic measurements

The DC magnetic susceptibility (χ) of the sample with the largest Ti concentration, Ti(0.3), is shown in Fig. 5.5(a), for a fixed field of 1000 Oe. I fit the low-T data to a Curie-Weiss function according to the standard relationship, $\chi(T) = C/(T - T_c) + \chi_0$, where $C = N_A c \mu_{\text{eff}}^2 / 3k_B$ is the Curie constant with c the concentration of paramagnetic defects, and μ_{eff} the effective moment. The results are $T_C = -1.4$ K, $\chi_0 = 2.8 \times 10^{-4}$ emu mol^{-1} and assuming $\mu_{\text{eff}} = 3.87\,\mu_B$ per defect corresponding to $J = 3/2$ (see below), a dilute concentration $c = 0.01$ per formula unit of these defects.

M *vs* H measurements confirm that the magnetic response is due to dilute paramagnetic defects, as shown at $T = 5$ K in Fig. 5.5(b) for sample Ti(0.3). To analyze for the local magnetic moments, data were fit to

$$M = N_A c g J \mu_B B_J(x), \tag{5.8}$$

where $B_J(x)$ is a Brillouin function with $x = \frac{g\mu_B JB}{k_B T}$. Assuming $g = 2$ expected for transition ions, I found that $J = 3/2$ gives the closest agreement [Fig. 5.5(b)] by choosing possible J values and fitting to c. Fixing $J = 3/2$, the fitted $c = 0.008$ per formula unit agrees well with the value obtained from M-T measurement, $c = 0.01$. This indicates that the predominant magnetic defect is a $J = 3/2$ local moment.

The small density of moments obtained here is comparable to what was obtained in annealed unsubstituted NbFeSb samples [15], for example 0.002 per formula unit in sample NbFeSb-1050 also with $J = 3/2$ (see Chapter 4). Thus, I see that there is almost no tendency for Ti substitution to promote magnetic defect formation. Note also that in TiFe$_{1+x}$Sb half-Heusler alloys close to the stable TiFe$_{1.33}$Sb composition [149, 150], with the Fe interstitials balancing the charge of the Ti ions to achieve 18-electron balance, a large Curie-type response was observed. However, this term corresponds to only a few percent of the Fe sites, with the bulk of the material also nonmagnetic similar to NbFeSb, as confirmed by Mössbauer results [150]. In the compositions studied here, even with Ti substitution far from the 18-electron stability rule, there are not significant numbers

of Fe interstitials (Table 5.1). By analogy with the $TiFe_{1.33}Sb$ results quoted above, those antisites present are likely to be nonmagnetic, and perhaps these are the source of the defects indicated by Mössbauer results. As was discussed in detail in Ref. [15] a likely candidate for the dilute-magnetic $J = 3/2$ defects would be Fe antisites on Nb positions. Note also that a small paramagnetic peak [15] might also be expected in the NMR $1/T_1$ [Fig. 5.3(c)]; however, here the relaxation rate is strongly dominated by a larger $1/T_1$ contribution due to the carriers in the substituted samples.

5.5 Discussion

The variation in amplitude of the satellite ^{57}Fe Mössbauer peak in NbFeSb is an unusual feature corresponding to a relatively large density of defects with charge states changing *vs* T. As shown above, this is consistent with the existence of the impurity band shown previously from NMR results [15]. The temperature dependence of ^{57}Fe Mössbauer absorption area shows that the origin of the impurity band is Fe-related, perhaps due to Fe interstitials [15].

In a previous study, Gerard *et al.* pointed out that charge promotion between bands in FeSi and $FeSb_2$ can lead to dynamically averaged spectra [151], and charge hopping in mixed valence materials has also been observed to lead to activated dynamical effects [152, 153]. However, in contrast to excitation of carriers in delocalized bands, here I consider charge promotion involving fixed defect sites. Since a fixed satellite is observed here, I surmise that there is very little hopping between these sites within the impurity band on the Mössbauer time-scale, whereas hopping faster than $\sim$10-100 MHz would be expected to collapse the satellite line with the main line. I also consider the possibility that the charges would be dynamically promoted between the band edge and the defect states fast enough to lead to an averaging of the spectrum. However, the defect capture cross-section can vary over many orders of magnitude in semiconductors depending upon the relative symmetries, and whether a phonon must be involved, which are not known in the present case. Thus, the charge-state lifetime is not known, but based on the good agreement between the excitation energy observed for the Mössbauer satellite amplitude and the previously observed NMR results connected to a band of impurity states [15], I conclude that the behavior of the Mössbauer satellite is also connected to these defects.

Besides our work, Hobbis $et\ al.$ [148] also reported ^{57}Fe Mössbauer spectroscopy of NbFeSb; however, in contrast with the *p*-type NbFeSb-1050 sample, their work focused on *n*-type NbFeSb. For *n*-type NbFeSb, two extra small doublets were observed with positions that differ from that of our measured satellite (0.65 mm/s). These different behaviors indicate distinct types of defects, which is reasonable given the different carrier types.

Comparing to ^{57}Fe Mössbauer results for different materials within the half-Heusler family, for VFeSb, only a single line was observed with an isomer shift of ∼0.05 mm/s with no extra peaks [154]. In Ref. [150], ^{57}Fe Mössbauer of $TiFe_{1.33}Sb$ also shows two sets of peaks, a doublet (main peak) with an isomer shift 0.108 mm/s and a singlet with an isomer shift 0.279 mm/s (a satellite peak). These were matched to certain local atomic arrangement close to Fe atoms, indicating non-randomness of Fe atoms on the $4d$ site. The larger shifts observed for NbFeSb are consistent with the results found here for $Nb_{1-x}Ti_xFeSb$, with an isomer shift which is enhanced as the number of Ti neighbors increases.

In transition metals, besides the contribution from the spin moments of the conduction electrons, the orbital contribution to the NMR relaxation caused by fluctuating orbital moments of the conduction electrons can also make an important contribution to $1/T_1$. In this case, the spin-lattice relaxation rate should be dominated by two terms: $(1/T_1)_{\rm total} = (1/T_1)_{\rm orb} + (1/T_1)_d$, where the first term is an orbital contribution term and the second is the *d*-spin relaxation rate.

For transition metals with cubic structure, the orbital relaxation rate can be expressed in a general form [155],

$$(1/T_1)_{\rm orb} = 2A\frac{2\pi}{\hbar}[\gamma_e\gamma_n\hbar^2 g_{\rm Nb}(E_F)\langle r^{-3}\rangle]^2 k_B T, \tag{5.9}$$

where $A = 10\alpha(2-\alpha)$ is a dimensionless quantity with α the degree of admixture of Γ_5 and Γ_3 symmetry at the Fermi level and $\langle r^{-3}\rangle$ is the average over occupied *d* orbitals, expected [156] for NbFeSb to include only on-site contributions. It was shown in Ref. [155] that $(1/T_1)_{\rm orb}$ for *d*-band metals reaches a maximum with an admixture of *d* orbitals corresponding to $\Gamma_5 : \Gamma_3 = 3 : 2$. Our DFT calculation shows that the ratio of atomic functions for NbFeSb near the band edge is $t_{2g}(\Gamma_5) : e_g(\Gamma_3) = 68\% : 32\%$, giving $A = 9.8$, close to the maximum $A = 10$, while for Nb, the

calculated $g(E)$ near the VB edge is 14% of the total. Since, as shown below, $(1/T_1)_{\rm orb}$ is found to dominate, I examine the dependence on Ti substitution. In Fig. 5.3(d), the solid line is a fit of Eq. (5.9) to Ti(0.05) and Ti(0.1) with $g(E_F)$ expressed by Eq. (7.5). Using $\langle r^{-3}\rangle = 1.84 \times 10^{25}$ cm^{-3} [157], I obtain $m_{\rm eff} = 4.6\, m_e$ in a good agreement with the calculated $m_{\rm eff} = 4.9\, m_e$ for unsubstituted NbFeSb.

The core polarization contribution to the *d*-spin spin-lattice relaxation rate in metals is

$$(1/T_1)_d = 2hk_BT[\gamma_n H_{\rm CP} g_{\rm Nb}(E_F)]^2 q, \tag{5.10}$$

where the core polarization hyperfine field $H_{\rm CP}$ is reported to be -21 T [138] and q is a reduction factor which is a function of the admixture of *d* orbitals. In the present case, nearly uniform occupation of the five *d* orbitals gives $q \approx 1/5$ [138]. Using $g_{\rm Nb}(E_F) = 0.243$ states/eV calculated as described above for the case of $x = 0.3$, Eq. (5.10) gives $(1/T_1T)_d = 0.016$ s^{-1} K^{-1} with $m_{\rm eff} = 4.6\, m_e$, inserted in Eq. (7.5). This is considerably smaller than the observed rates. There is also a dipole spin contribution to $1/T_1$; however, for the large *d*-orbital degeneracy case, this can be shown [138] to be much smaller than the orbital contribution. These results show that the orbital contribution is the dominant term in the spin-lattice relaxation process.

When the Ti fraction increases to 30%, the $1/T_1T$ values depart from $p^{2/3}$ behavior (solid line in Fig. 5.3(d) fitted to the two low-*p* points). At the same time, there is a decrease in the measured hole density relative to $p_{\rm theo}$, as also shown in Fig. 5.3(d). Non-parabolicity of the valence band could give an increase in $m_{\rm eff}$ which might explain the $1/T_1T$ upturn; however, such an effect would not be expected to affect the Hall effect results, at least in the spherical hole pocket limit. Thus, I conclude that the presence of resonant levels having low mobility in the valence band [158] becomes important for large *x*. The results shown in Fig. 5.3(e) help to further clarify this result, indicating that $1/T_1$ is affected by states near E_F which make little contribution to the Hall results. For large *x*, the Fermi level moves more deeply into the valence band encountering states caused by Ti substitutions. This effect could have significance for thermoelectric properties; however, the

agreement between theory and experiment indicates that such effects are not important for smaller *x*, and thus a rigid-band effective mass model provides a good description for the less-heavily substituted compositions.

For Ti(*x*) samples, the measured Knight shift values are also found to be larger than expected. For example, the Knight shift contribution to the total shift for the Ti(0.3) sample is -2185 ppm from our fit. However, using $g_{\rm Nb}(E_F) = 0.243$ states/eV obtained above and the core polarization hyperfine field $H_{\rm CP} = -21$ T, Eq. (7.7) gives $K = -295$ ppm. (The orbital shift contribution is the chemical shift discussed below, which does not depend on $g(E_F)$.) The Knight shift difference could be explained by a large $g_{\rm eff}$ in these samples, or by electron-electron interactions which can also enhance the measured spin susceptibility and thereby the Knight shift.

In addition to the observed large Knight shifts, the ^{93}Nb chemical shifts (δ) also show relatively large values as noted above. Paramagnetic contributions to δ depend upon the connection of filled to empty states through the applied field and orbital hyperfine interaction. Similar to the Van Vleck susceptibility ($\chi_{\rm VV}$), the connection of multiple orbitals in this way with a small energy splitting can give a large response, and in the present case *d* orbitals divided between the conduction and valence bands with relatively small separation appear to be the main contribution to these shift [24]. However, the DFT calculations give the ^{93}Nb chemical shift as 3220 ppm, compared to the fitted $\delta = 4020$ ppm. This shift difference corresponds to a further enhancement of the local orbital hyperfine field which I believe is an interaction effect. In addition to the well-known enhancement of the spin susceptibility, electron-electron interactions can also lead to an enhancement of $\chi_{\rm VV}$ [159], and thus by analogy an enhanced chemical shift. Ref. [160] also pointed out that orbital degeneracy is necessary for this effect; the large degeneracy of orbitals was already discussed above in analyzing the $1/T_1T$ of these samples. Thus, although the calculated distribution of *d* electrons in the valence band for Nb and Fe provide good agreement with the observed orbital T_1, as a measure of the local susceptibilities the NMR shifts demonstrate that electron-electron interaction effects are relatively strong for these states. This is examined in further detail in the next chapter.

5.6 Summary

In this chapter, I have investigated the effect of defects and substitutions of NbFeSb and $Nb_{1-x}Ti_xFeSb$ using local ^{93}Nb and ^{121}Sb NMR and ^{57}Fe Mössbauer probes. The spin-lattice relaxation results are well modeled in terms of an orbital contribution in good agreement with DFT calculations for NbFeSb. With increasing x, I find a deviation from the expected behavior due to resonant valence band levels which do not contribute to transport results. NMR shift *vs* x are well-explained by a model combining carrier-concentration-dependent Knight shift and composition-dependent chemical shift. The local paramagnetic susceptibilities are found to be significantly enhanced relative to calculated values. The T-dependence of the satellite peak in the unsubstituted NbFeSb Mössbauer spectrum provides a direct measure of charging of acceptor states in an impurity band located around 30 meV above valence band edge as previously reported. The Mössbauer spectrum for $x = 0.3$ shows small departures from a binomial distribution, indicating a small deviation from random substitution in the mixed alloys, revealing a possible segregation of 4*a*-site substitution atoms.

6. OTHER THERMOELECTRIC HALF-HEUSLERS*

6.1 Introduction

In this chapter, I apply NMR in studying members of a series of transition-metal-based half-Heusler materials, including TaFeSb, NbCoSn, ZrCoSb and NbFeSb, focusing in particular on trends in the electronic properties in this thermoelectric materials family. All half-Heusler samples were prepared by Dr. Ren's group at University of Houston. The DFT was conducted by my labmate Dr. Nader Ghassemi and I measured all the experimental results.

6.2 Sample Preparation

All of the half-Heusler polycrystalline samples discussed in this chapter were made from high purity elements (Zr, Sb, Nb and Ta $\geq$ 99.9%; Fe and Sn $\geq$ 99.8%; Co $\geq$ 99.5%). ZrCoSb and NbFeSb were prepared by arc-melting, ball-milling and hot-pressing and NbCoSn and TaFeSb were made by ball-milling and hot-pressing. These include: (a) ZrCoSb which is the same material described in Ref. [161], prepared using AC hot pressing at 1400 K and pressure of $\sim$80 MPa for 2 min. Microprobe measurements indicated a composition of $ZrCo_{1.02}Sb_{0.99}$, while the Seebeck coefficient result indicates that ZrCoSb is an *n*-type material with a large Seebeck peak of about -280 μV/K observed near 600 K. (b) NbCoSn which was prepared as described in Ref. [162], where the sintering was at 1113-1273 K under a pressure of $\sim$80 MPa for 2 min. The actual NbCoSn composition was measured to be $Nb_{31.4}Co_{35.4}Sn_{33.2}$, indicating a likely *n*-type behavior for NbCoSn with the extra Co possibly located on Nb sites. (c) TaFeSb which was prepared as described in Ref. [35] with hot-pressing temperature about 1123 K and pressure of $\sim$80 MPa for 2 min. The positive Seebeck coefficient result indicates that TaFeSb is a *p*-type material with no peak observed in S below 1000 K, unlike its "twin material" NbFeSb [15]. (d) NbFeSb which is the same sample as NbFeSb-1050 described in Ref. [15] and Chapter 4. Hall measurement showed

*Part of this chapter is reprinted from Ref. [24] (Y. Tian, N. Ghassemi, W. Ren, H. Zhu, S. Li, Q. Zhang, Z. Wang, Z. Ren, and J. H. Ross, Jr., "Half-Heusler thermoelectric materials: NMR studies," J. Appl. Phys., vol. 128, no. 5, p. 055106, 2020.) with permission from AIP Publishing.

this sample as *p*-type with carrier concentration of 9×10^{19} cm^{-3}. The sample preparation was done in the group of Z. Ren at University of Houston. All other work (except for DFT) described below was done by myself at TAMU or using external facilities.

6.3 Experimental and Computational Details

^{59}Co, ^{93}Nb, and ^{121}Sb NMR experiments were carried out by applying a custom-built pulse spectrometer at a fixed magnetic field 9 T using shift standards aqueous $K_3[Co(CN)_6]$, $NbCl_5$, and $KSbF_6$ in acetonitrile, respectively, with positive shifts here denoting paramagnetic sign. NMR spectra were obtained from the fast Fourier transform of the spin echo using a standard $\pi/2$-τ-π sequence.

Density function theory (DFT) calculations were conducted using the WIEN2k package [113]. In this package, an (linearized) augmented plane wave plus local orbitals method is implemented. These calculations were done using the experimental lattice parameters $a = 6.068$ Å for ZrCoSb [163], 5.950 Å for NbFeSb [15], 5.938 Å for TaFeSb [35], 5.950 Å for NbCoSn [162, 164], and 5.883 Å for TiCoSb [22]. We used $10 \times 10 \times 10$ k-points and adopted the exchange correlation functional introduced by Perdew, Burke, and Ernzerhof (PBE) [165]. The calculations were run without spin-orbit coupling or spin polarization. Calibration of calculated ^{93}Nb chemical shifts was done by computing shifts for $YNbO_4$ and $LaNbO_4$, and comparing to the standard reference ($NbCl_5$ in acetonitrile) as established in Ref. [146]. For ^{59}Co and ^{121}Sb, no comparable solid-state shift standard has been established, so we report relative calculated shifts.

6.4 Results and Discussion

6.4.1 ZrCoSb

In Fig. 6.1(a), the room-temperature ^{59}Co NMR spectrum for ZrCoSb is shown. The spectrum is relatively broad, with a full width at half maximum (FWHM) of 750 ppm (equivalent to 67 kHz), and a Lorentzian shape similar to what has been reported for TiCoSb after annealing [22]. The corresponding ZrCoSb ^{59}Co center-of-mass shift was measured in the temperature range 77-295 K. Note that the error bars have not been indicated for the extracted shifts; however, these are

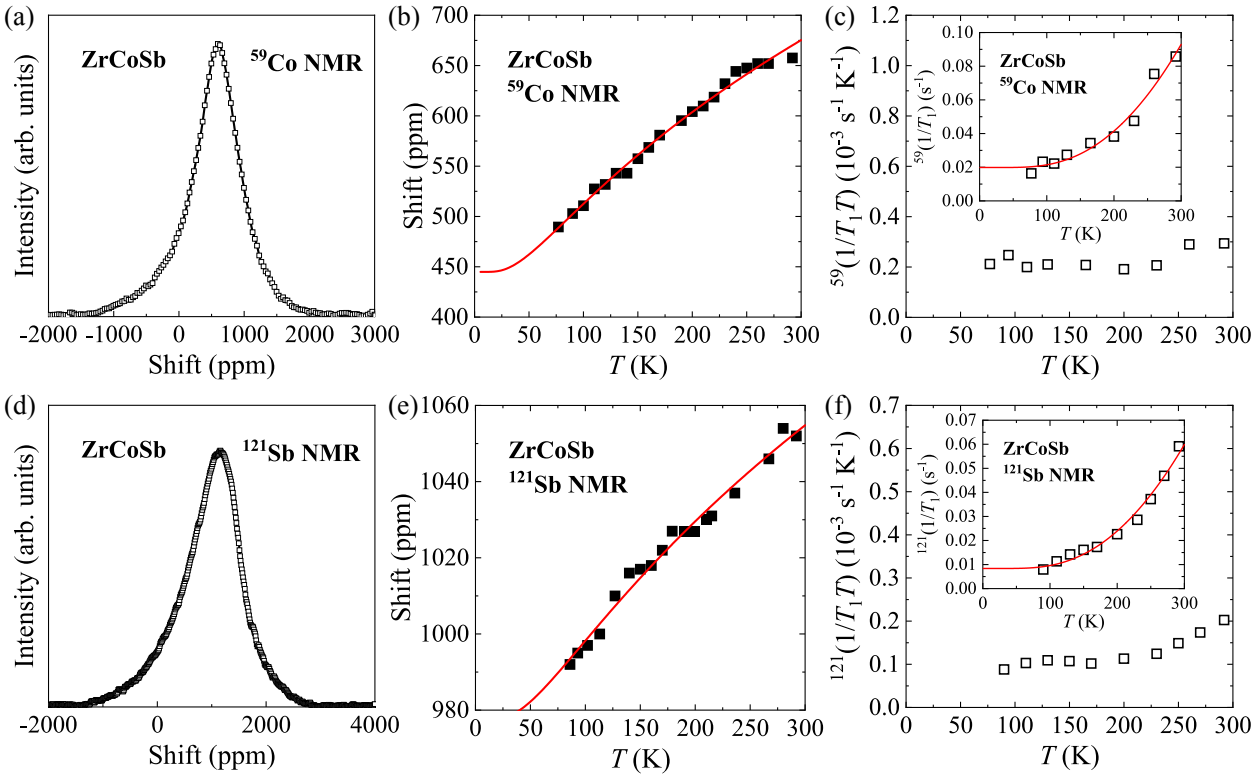

Figure 6.1: NMR results for ZrCoSb. ^{59}Co NMR: (a) room-temperature lineshape, (b) shift *vs* T, and (c) $^{121}(1/T_1T)$ *vs* T [inset: $^{121}(1/T_1)$ *vs* T]. ^{121}Sb NMR: (d) room-temperature lineshape, (e) shift *vs* T, and (f) $^{59}(1/T_1T)$ *vs* T [inset: $^{59}(1/T_1)$ *vs* T]. Shifts and $1/T_1$ for both nuclei are fitted to an excitation energy gap function (solid curves).

typically 5-10 ppm, for all samples. As shown in Fig. 6.1(b), the results can be fitted to a function corresponding to a small energy gap. In this model, when temperature increases, the carriers are thermally excited across an excitation gap, leading to the increase of spin susceptibility. For a parabolic band-edge, appropriate for semiconductors, the change in shift will be proportional to the density of excited carriers divided by the temperature. Thus, the mechanism of shift increase can be written as [166]

$$K = K_1 + C_1 T^{1/2} \exp(-\Delta/k_B T), \tag{6.1}$$

where K_1 is a temperature-independent contribution and Δ is the excitation energy. Note that very similar excitation behavior was also reported in TiCoSb [22], with Ti substituted from the same group. The solid red curve in Fig. 6.1(b) represents a fit to Eq. (6.1), yielding $\Delta = E_g/2 = 18$ meV, consistent with the result obtained via spin-lattice relaxation shown below. The constant term $^{59}K_1$ is 445 ± 20 ppm.

Note that here I use the notation K for the total observed shift of the NMR line, which is normally a sum of the Knight shift due to carrier spin susceptibility (which I designate K_c) and the chemical shift (δ) due to local orbital susceptibility. Although these nuclei have electric quadrupole moments, quadrupole contributions to the shift will vanish in these cubic materials. However, due to random quadrupole splitting due to defects or small internal strains, the satellite splitting is sufficient that the observed lines are (1/2 to $-1/2$) transitions. This is the case for all of the observed spectra, as I verified by the optimized 90-degree pulse lengths. These small random quadrupole splittings will not affect the line positions, thus the shifts were treated as $K = K_c + \delta$. In the limit of zero carrier density, K_c will vanish, leaving only δ as the observed contribution.

^{59}Co spin-lattice relaxation results $^{59}(1/T_1)$ are shown in the Fig. 6.1(c) inset, with $^{59}(1/T_1T)$ shown in the main plot. An inversion-recovery sequence was used for the measurements, with the results fitted to a multi-exponential recovery curve appropriate for the observed (1/2 to $-1/2$) transitions; this was also done for the other materials described below. Generally, the small $^{59}(1/T_1)$ indicates a relatively low density of carriers interacting with the nuclei, while at high T, $^{59}(1/T_1)$ rises rapidly with temperature increasing, which is the characteristic behavior for semiconductors.

Similar to the shift behavior, $^{59}(1/T_1)$ was also fitted to an excitation energy gap. Based on the same mechanism as the shift, the increase in relaxation rate is due to an increase of carriers induced by thermal excitation. In this case, the spin-lattice relaxation rate is given by [166]

$$1/T_1 = C_2 T^2 \exp(-\Delta/k_B T) + \text{const.} \tag{6.2}$$

In good agreement with the shift fitting, this fit yields an excitation gap $\Delta = 17$ meV. Note that this analysis is different from that of the other half-Heuslers, since I found that based on the combined shift and spin-lattice relaxation results for ZrCoSb, the excitation-gap model gives much more reasonable and consistent fits than a Curie-Weiss model.

Similar to ^{59}Co NMR, ^{121}Sb NMR has also been measured for ZrCoSb as shown in Figs. 6.1(d)-6.1(f). Again a broad Lorentzian-type line is observed, with room-temperature FWHM of 1030 ppm (equivalent to 93 kHz). The same fits described for ^{59}Co have been done for the ^{121}Sb NMR shifts and $^{121}(1/T_1T)$, with $\Delta = 10$ meV obtained from the shift fit and $\Delta = 22$ meV from $^{121}(1/T_1T)$, consistent with the ^{59}Co NMR results and confirming the presence of a small gap. For consistency, fits for both the center-of-mass shift [Fig. 6.1(e)] and $^{121}(1/T_1)$ [Fig. 6.1(f) inset] have been recalculated, fixed with an excitation gap $\Delta = 17.5$ meV, the mean value obtained for ^{59}Co. The corresponding constant term $^{121}K_1$ is 978 ppm.

In Ref. [22], there is an increased line broadening observed in TiCoSb after annealing. The broad lineshape was fitted to Lorentzian function which apparently indicated dilute magnetic local-moment broadening. A quantitative analysis [22] showed about 2% Co local moments appearing after annealing. Similarly, the somewhat larger line widths observed in ZrCoSb also likely indicate a local moment density on this order, presumably due to Co antisites. While there has previously been uncertainty [161] about the significance of antisites in this material, the relatively large line widths in ZrCoSb, as compared to other half-Heusler samples described below, point to an enhanced tendency towards such local disorder in this material.

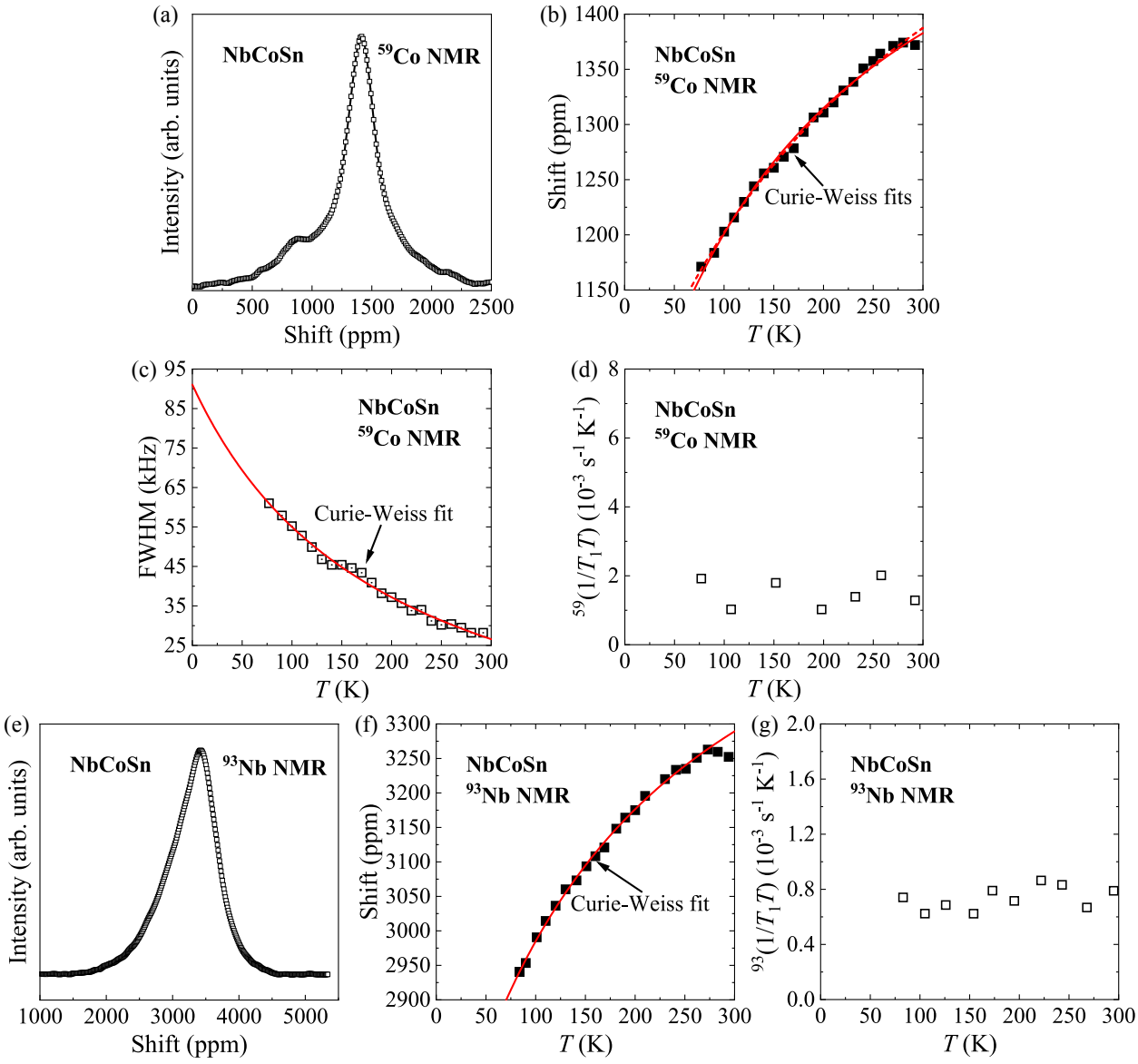

Figure 6.2: NMR results for NbCoSn. ^{59}Co NMR: (a) room-temperature lineshape, (b) shift *vs* T, (c) FWHM *vs* T, and (d) $^{59}(1/T_1T)$ *vs* T. ^{93}Nb NMR: (e) room-temperature lineshape, (f) shift *vs* T, and (g) $^{93}(1/T_1T)$ *vs* T. Solid and dashed curves are Curie-Weiss fits described in text.

6.4.2 NbCoSn

Figs. 6.2(a) and 6.2(e) show the ^{59}Co and ^{93}Nb room-temperature spectra of NbCoSn, respectively. The line shapes are slightly asymmetric, with line widths of 300 ppm (28 kHz) for ^{59}Co NMR and 790 ppm (72 kHz) for ^{93}Nb NMR, increasing as T is lowered. Figs. 6.2(b) and 6.2(d) show ^{59}Co NMR center-of-mass shifts and spin-lattice relaxation rate results for NbCoSn *vs* T. Similarly Figs. 6.2(f) and 6.2(g) show ^{93}Nb NMR shifts and spin-lattice relaxation rate results. The shifts in both cases were modeled by $K = K_1 + K_2(T)$, where $K_2(T)$ was well fitted to a Curie-Weiss type function, $A_1/(T+\theta)$. The fit for ^{59}Co $K_2(T)$ is shown as the dashed curve in Fig. 6.2(b), yielding $^{59}K_1 = 1815$ ppm and the Curie-Weiss temperature $\theta = 309$ K. Shown in Fig. 6.2(c), the ^{59}Co line width also follows a Curie-Weiss law, FWHM $\propto A_2/(T+\theta)$, with the fitted Curie-Weiss temperature $\theta = 196$ K. In this material, the lineshapes have a tail on the low frequency side, presumably due to a small amount of composition inhomogeneity; however, the FWHM is relatively unaffected by this. Thus, I rely upon the FWHM result as a better measure of the temperature dependence, and the Curie-Weiss temperature was fixed to $\theta = 196$ K for fitting the ^{59}Co shift, giving the result shown as the solid curve with the resulting $^{59}K_1 = 1652$ ppm.

Shown in Fig. 6.2(f), the ^{93}Nb center-of-mass shift also follows a Curie-Weiss behavior. For both nuclei, there is a small shift downturn near room temperature, perhaps due to a small increase in carrier density due to native defects, such as seen in NbFeSb [15]. The Curie-Weiss fit yields $\theta = 188$ K with the corresponding $^{93}K_1 = 3728$ ppm, in good agreement with the ^{59}Co line width result, confirming the paramagnetic mechanism governing the observed behavior of NbCoSn. The Curie-Weiss term observed in the NbCoSn shifts indicates local hyperfine interactions with magnetic moments, as opposed to the results observed in ZrCoSb and NbFeSb (shown below), which correspond to long-range dipolar interactions with relatively dilute local moments. Thus, the behavior is that of a more strongly magnetic material, comparable to Refs. [167, 168], with the shifts and line widths scaling together. However, the effect here is much smaller than expected for a magnetic semiconductor [168], with for example no sign of the constant-$1/T_1$ behavior characteristic of interaction-driven fluctuations, indicating a weak effect. The source of the magnetic

moments is apparently the observed Co excess, an effect which also drives this material to *n*-type behavior [162].

The constant $1/T_1T$ shown in Figs. 6.2(d) and 6.2(g) is characteristic of a Korringa-type mechanism, representing the partial Fermi-level DOS of the probed site. The results reveal that there are sufficient carriers so that the Fermi level locates in the band for the whole measured temperature range. The results are larger than observed in ZrCoSb, but $^{93}(1/T_1T)$ is still considerably smaller than observed in NbFeSb [15], for which the Korringa contribution was specifically identified and extracted from the paramagnetic contribution. This indicates that the Knight shift contribution is relatively small for NbCoSn.

6.4.3 TaFeSb

Fig. 6.3(a) shows the room-temperature ^{121}Sb NMR spectrum for TaFeSb, showing a relatively narrow FWHM equal to 210 ppm (21 kHz). Fig. 6.3(b) shows the shift obtained from the center of mass of the measured spectra. As above, the shifts can be expressed by $K = K_1 + K_2(T)$, where K_1 is a temperature-independent term and $K_2(T)$ is the temperature-dependent term which I observed to follow a Curie-Weiss type behavior, $A_1/(T + \theta)$. A fit to this function yields $^{121}K_1 = 1193 \pm 6$ ppm and the corresponding Curie-Weiss temperature $\theta = 9$ K. The fitting shows the existence of paramagnetic centers, possibly in the form of paramagnetic defects; however, the magnitude is considerably smaller than what was observed in NbCoSn.

Fig. 6.3(c) shows the temperature dependence of the ^{121}Sb FWHM, which can also be fitted to a Curie-Weiss type function FWHM $\propto A_2/(T + \theta)$. The unconstrained fit yields $\theta = 22$ K, close to the ^{121}Sb shift result. For the same reason as NbCoSn, I thus fixed the Curie-Weiss temperature as 22 K for the shifts with corresponding $^{121}K_1 = 1199$ ppm, yielding the fitting curve shown in Fig. 6.3(b). (In the figure, the $\theta = 9$ and 22 K curves are indistinguishable, so the $\theta = 9$ K case cannot be seen.) Similar to Refs. [167, 168], and for NbCoSn, the FWHM of TaFeSb at each temperature also scales as about 2-3 times the shift, thus the average local field is about the same size as the distribution of local fields about the mean value. This confirms the local-hyperfine mechanism, and Curie-Weiss behavior of TaFeSb. By analogy to the previous analysis of the "twin

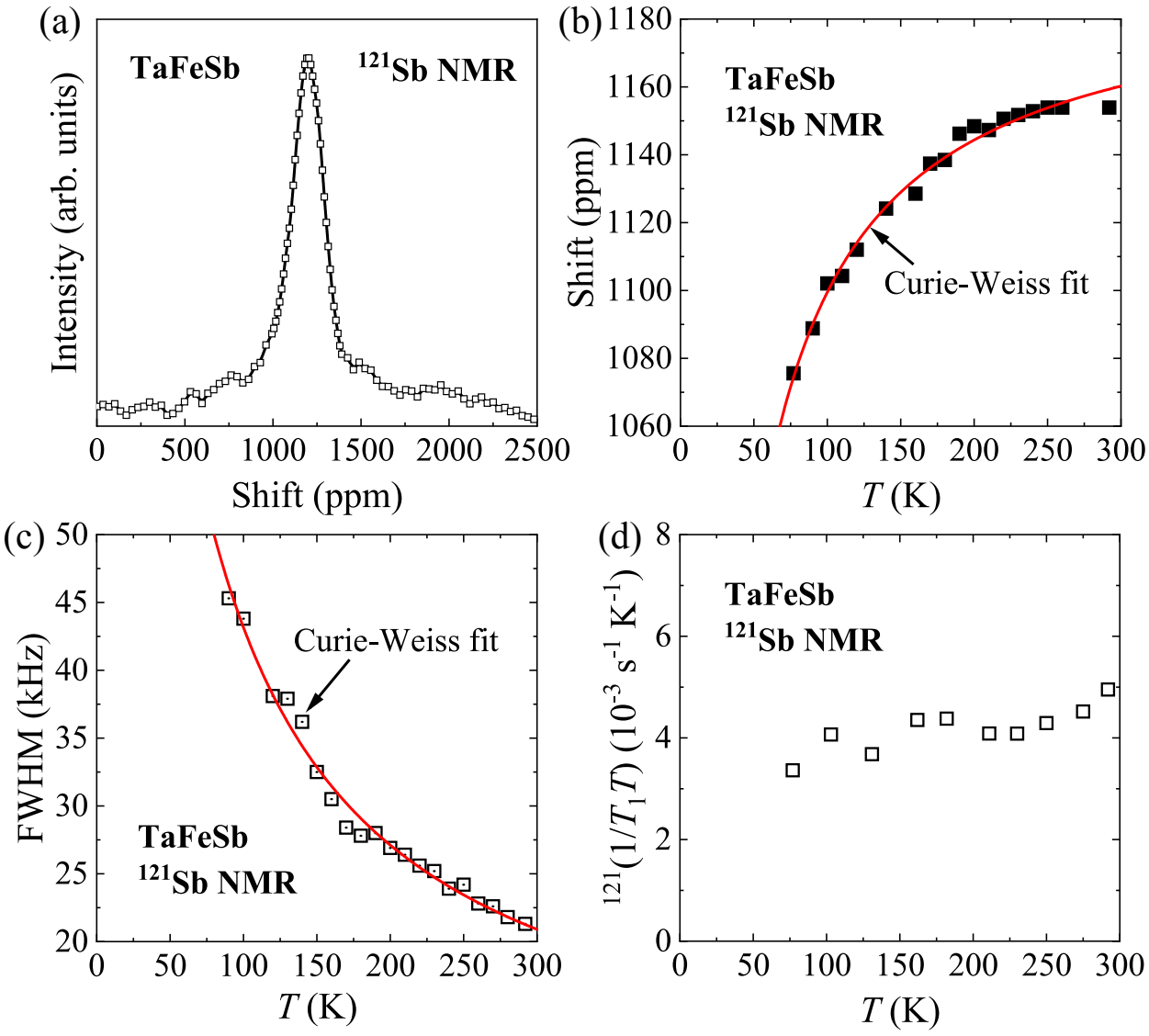

Figure 6.3: ^{121}Sb NMR for TaFeSb: (a) room-temperature lineshape, (b) shift *vs* T, (c) FWHM *vs* T, and (d) $^{121}(1/T_1T)$ *vs* T. Solid curves are Curie-Weiss fits described in text.

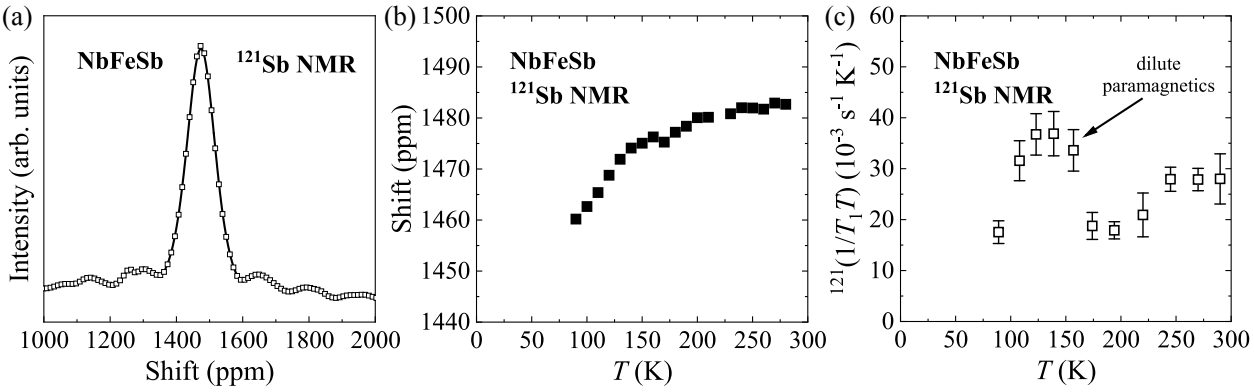

Figure 6.4: ^{121}Sb NMR for NbFeSb: (a) room-temperature lineshape, (b) shift *vs* T, and (c) $^{121}(1/T_1T)$ *vs* T.

material" NbFeSb [15], the local moments for TaFeSb are likely Fe antisites. The Curie-Weiss behavior points to weak interactions for these moments, in contrast to NbFeSb (below) where the $1/T_1$ peak indicates independent fluctuations of dilute moments, behavior which is not observed in TaFeSb.

The constant $1/T_1T$ shown in Fig. 6.3(d) represents the partial Fermi-level DOS of the probed site, indicating the weakly metallic behavior of TaFeSb at low temperature. When temperature is above 250 K, a small upturn can be observed, revealing a possible additional excitation of carriers, as was fitted for the case of ZrCoSb. However, the baseline $1/T_1T$ in this case is larger, making the carrier excitation effect relatively quite small. The constant shift term K_1 is a combination of chemical shift and Knight shift. Based on the Korringa relation, the Knight shift $^{121}K_c$ can be estimated from measured $^{121}(1/T_1T)$ and the small magnitude reveals that the contribution of charge carrier is not significant. Details of calculation can be found below.

6.4.4 NbFeSb

Figs. 6.4(a)-6.4(c) show the ^{121}Sb NMR results for NbFeSb, which shows similar behavior comparable to ^{93}Nb NMR reported in Ref. [15] for the same sample. In Fig. 6.4(a), the ^{121}Sb NMR spectrum shows a very narrow line width, with FWHM about 90 ppm (8 kHz) at room temperature, similar to the ^{93}Nb spectrum. There is a very small decrease in shift as temperature is lowered

[Fig. 6.4(b)], and as shown in Fig. 6.4(c), $^{121}(1/T_1T)$ also shows a peak very similar to the ^{93}Nb results [15], shown to be due to very dilute magnetic moments [15]. To extract the moment density requires a more detailed set of measurements using a stretched-exponential analysis [15]; however, for comparison the observed peak $^{93}(1/T_1)$ corresponds to $^{93}(1/T_1T) = 30 \times 10^{-3}$ (s K)$^{-1}$, very similar to the result observed here. Due to a long range dipole mechanism, in the dilute-moment limit, the results are scaled only by the squared gyromagnetic ratios of the two nuclei [40], which are almost identical. Both ^{93}Nb and ^{121}Sb relaxation peaks have very similar magnitudes further confirming the mechanism of long-range dipolar interaction with dilute local magnetic spins in NbFeSb and validating the previous results.

NbFeSb has a significant Knight shift for both nuclei. In Ref. [145], both ^{93}Nb and ^{121}Sb chemical shifts were extracted by studying a series of Ti-substituted samples ($Nb_{1-x}Ti_xFeSb$). Assuming that the chemical shift is linearly dependent on Ti-substitution level for these semiconductors, the chemical shifts were then obtained by a fitting model with measured shifts composed of carrier-density-dependent Knight shift and substitution-fraction-dependent chemical shift. As a result, it also turned out that both ^{93}Nb and ^{121}Sb also have significant Knight shifts in the undoped material. This is consistent with the measured much larger $1/T_1T$ compared to other half-Heusler materials: for example, underlying the paramagnetic peak [Fig. 6.4(c)] it can be seen that the baseline $1/T_1T$ is on order of $^{121}(1/T_1T) \approx 15 \times 10^{-3}$ (s K)$^{-1}$.

6.4.5 DFT computed shifts

Fig. 6.5 is the comparison between experimental shifts and DFT calculated chemical shifts (δ) for the half-Heusler materials, including results for all nuclei (^{93}Nb, ^{59}Co and ^{121}Sb) measured in this work. The experimental values plotted are the temperature-independent shifts (identified as K_1), extracted as discussed above, with the effects of thermally excited carriers (ZrCoSb) or Curie-Weiss contributions (NbCoSn, TaFeSb) removed. While these values generally contain Knight shifts and chemical shifts ($K \equiv K_c + \delta$), where possible, I have identified the Knight shift contributions and these are generally small perturbations, as discussed below. I also include TiCoSb [22], another member of this general family for which NMR studies have been reported,

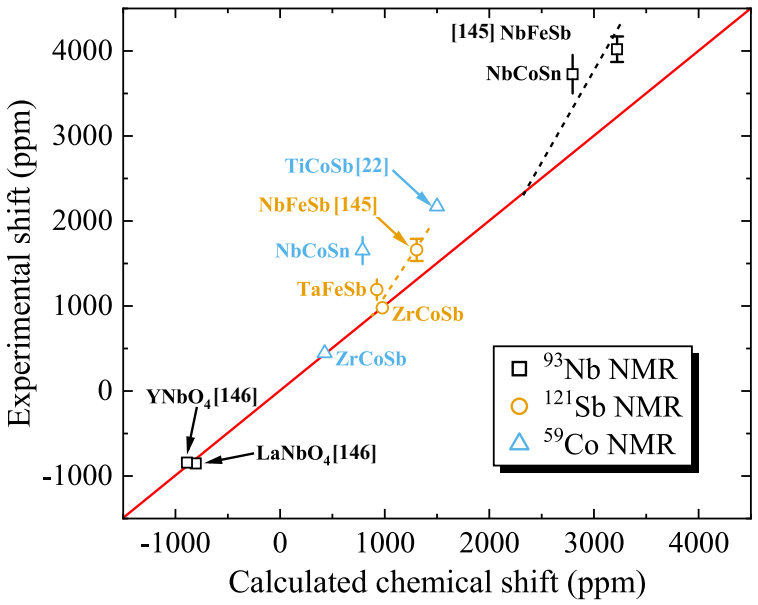

Figure 6.5: Comparison between experimental shifts and DFT calculated chemical shifts. NbFeSb chemical shifts are from Ref. [145], with error bars based on the subtraction of Knight shift contribution as described there, TiCoSb shift from Ref. [22] and Y(La)NbO_4 from Ref. [146]. Vertical bars without caps for the other compositions show the estimated range of chemical shifts after subtraction of Knight shift based on Korringa relation. Additional errors corresponding to uncertainty in measured shift values are smaller than the visible symbols. Dashed lines are guides to the eye.

and for NbFeSb the values are fitted values of δ alone with K removed based on composition-dependent results (Chapter 4). The red line in Fig. 6.5 corresponds to perfect agreement between experiment and calculation. Since measured chemical shifts are generally reported relative to NMR shift standards having unknown absolute shift contributions, a computational reference can be used to calibrate the absolute DFT shifts. For ^{93}Nb NMR shift, the calibrating references are $YNbO_4$ and $LaNbO_4$. For ^{59}Co and ^{121}Sb for which no comparable materials with well-defined chemical shift are available, I discuss here the relative shifts.

The Korringa relation is an important tool to understand metallic behavior, which is characterized by a T-independent Knight shift (K_c) and a constant $1/T_1T$. Often [137], the product $K_c^2T_1T$ is found to be very close to $K_c^2T_1T = (\hbar\gamma_e^2)/(4\pi k_B\gamma_n^2)$,where γ_e and γ_n are the gyromagnetic ratios of the electron and nucleus. However, since other mechanisms can contribute to $1/T_1$ and generally increase the rate, here I can consider that $1/T_1T$ serves to provide an upper limit esti-

mate for K_c. For example, in substituted NbFeSb a significant orbital contribution was shown to contribute to the relaxation rate [145]; however, this term does not contribute to K_c [145], and as noted above, paramagnetic contributions due to local moments can in some cases also contribute to $1/T_1$. For ^{121}Sb, based on the standard product $K_c^2 T_1 T = 4.5 \times 10^{-6}$ s K, the low temperature $^{121}(1/T_1T)$ values correspond to 20 ppm for ZrCoSb, and 130 ppm for TaFeSb. The small contribution for ZrCoSb, and a similar small contribution estimated from the ^{59}Co relaxation rates, justifies putting those values on the red line in Fig. 6.5, and using these values to calibrate the relative ^{59}Co and ^{121}Sb chemical shifts. For NbCoSn, the mean observed $^{93}(1/T_1T) = 1.5 \times 10^{-3}$ (s K)$^{-1}$ is 10 times smaller than the Korringa $^{93}(1/T_1T)$ extracted for the NbFeSb sample studied here [40], hence I estimate that $^{93}K_c$ may be $\sqrt{10}$ times smaller than the extracted Knight shift for NbFeSb, or about 230 ppm. The $^{59}(1/T_1T)$ values for NbCoSn are somewhat smaller than for ^{93}Nb, but K_c in both cases is expected to be negative, due to the negative core-polarization hyperfine fields corresponding to the *d* states which dominate the electronic behavior at the band edges for these ions. I have placed vertical bars on the NbCoSn points in Fig. 6.5, to represent the corresponding K_c contributions which may be present, and hence showing the range of underlying chemical shifts which can be deduced from the experimental results. These estimated uncertainties have been included in Fig. 6.5 as simple vertical lines. For the case of NbFeSb, as described above measurements of Ti-substituted materials were previously used to extract the chemical shifts [145], and the corresponding statistical error bars from this fit are displayed in Fig. 6.5.

6.4.6 Discussion and analysis

The actual size of the bulk gap in ZrCoSb is believed to be much larger than the fitting result described above (for example a calculated value near 1 eV has been reported [169, 170], and the observed Seebeck coefficient peak [161] for this sample also points to a gap that is significantly larger than what is apparent from the NMR results), indicating that a defect level locates above the valence band forming an impurity band in the bulk gap, similar to NbFeSb [15] (see Chapter 4). In Ref. [15], NbFeSb has also exhibited a very small gap $\sim$30 meV, shown to indicate an impurity band rather than a real band gap. By analogy, this small gap for ZrCoSb is likely to indicate the

existence of an impurity band, which is a narrow band of states within a semiconductor energy gap due to the combined effect of a relatively large density of impurity states. The *n*-type carrier type suggests that the impurity band is right below the conduction band, different from NbFeSb. Note also that $1/T_1T$ for both nuclei measured in ZrCoSb is very small, especially at low temperatures. As discussed below, it can be concluded that the extracted K_1 values have very little contributions due to free carriers (hence small Knight shifts, K_c). Thus, I analyze the fitted K_1 for ZrCoSb as representing the chemical shift. A similar argument can be applied to the previously reported results for TiCoSb [22], as further discussed below.

Comparing to ZrCoSb, the narrow line width of NbFeSb indicates a particularly strong tendency for local ordering in NbFeSb, for which the observed $1/T_1T$ peak provides evidence of a small density of independent magnetic moments. On the other hand, both TaFeSb and NbCoSn exhibit Curie-Weiss behavior, which can be understood as due to interacting Fe or Co antisites, owing to stoichiometry differences. The off-stoichiometry for TaFeSb is probably driven by difficult synthesis conditions due to the high melting temperature of Ta, while compared with TaFeSb, the broader line width of NbCoSn corresponds to its larger tendency for off-stoichiometry, and is reasonably consistent with the 2% Co excess measured by energy dispersive X-ray spectroscopy (EDS) [162].

The DFT computed shifts capture the general trend of the experimental shifts rather well, as seen in Fig. 6.5. Although there are Knight shifts involved in some of the measured shifts, as discussed above their estimated magnitudes are relatively small compared to the very large chemical shifts. This gives further confidence that WIEN2k can provide good predictions of chemical shift for these half-Heusler materials, and that the very large range of observed shifts is indeed intrinsic to these materials. For ZrCoSb, I showed that both the ^{59}Co and ^{121}Sb NMR measured shifts include very small Knight shifts, with a Korringa-type contribution that is essentially negligible. Similarly, TaFeSb also falls close to the red line in Fig. 6.5. However, a trend can be seen by which the larger shifts are enhanced relative to the expected values; this is emphasized by the dashed lines in Fig. 6.5. Note also that these larger shift values (^{93}Nb shift for NbFeSb and NbCoSn; ^{121}Sb shift

for NbFeSb and TiCoSb) are out of the established ranges of chemical shifts for ^{93}Nb [122] and ^{121}Sb [171] NMR.

These paramagnetic shifts can be understood as due to the paramagnetic susceptibility of nearly degenerate *d* bands split into the conduction and valence bands. The mechanism is closely related to the Van Vleck susceptibility, χ_{VV}, which measures the macroscopic orbital paramagnetism. A general form of the NMR orbital shift can be expressed [172] as

$$K_{\mathrm{orb}} = \frac{2e^2}{m^2c^2} \sum \frac{\langle \Psi | L_z | \Psi' \rangle \langle \Psi' | L_z / r^3 | \Psi \rangle}{\Delta E} + \mathrm{c.c.}, \tag{6.3}$$

where Ψ is an occupied state, Ψ' is an excited state, and the sum of angular momentum matrix elements across the semiconducting gap is an integration throughout momentum space of vertical transitions, associated with the bands as a whole rather than being dominated by the band edges. The multiplicity and larger angular momentum of *d* states separated by the gap, along with a relatively small ΔE [172], can lead to a large orbital shift contribution. Since the sum is unaffected by small additions of charger carriers at the band edge, this shift also has little temperature dependence.

As noted above, in Fig. 6.5 it can be observed that the experimental shift has the trend of exceeding the calculated chemical shift, as the shift values become large. This is seen most clearly for ^{121}Sb and ^{93}Nb shifts, illustrated by dashed lines. A likely explanation for this behavior is described in Refs. [159, 173, 174], indicating that the Van Vleck susceptibility can be enhanced by electron-electron interactions as well as the more familiar enhancement of the Pauli susceptibility. There is also a predicted increase due to spin-orbit interactions, with the example [159] being Sr_2RuO_4, for which the spin-orbit strength should be comparable in magnitude to NbFeSb, and the effect relies upon inter-orbital interactions, and thus requires orbital degeneracy within the band. Thus, tentatively I ascribe the orbital dominated Van Vleck shift enhancement in the half-Heuslers to e-e interactions in nearly degenerate *d* orbitals.

The correlation between chemical shifts and the electronegativities of neighboring ions is a

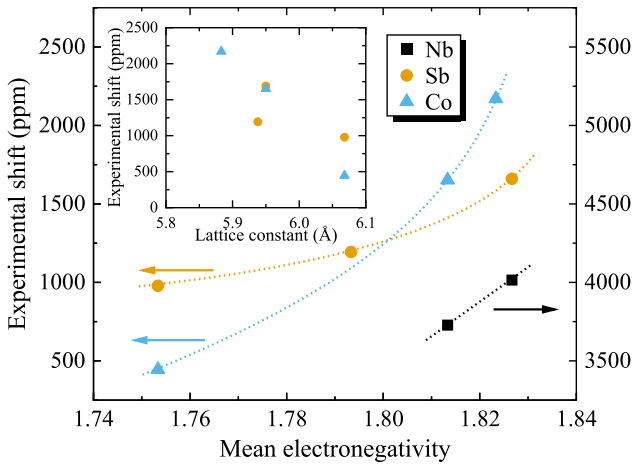

Figure 6.6: Experimental shifts *vs* mean electronegativity. Mean electronegativity is the mean value of Pauli electronegativities of three elements in each ternary half-Heusler sample. Dashed curves are guides to the eye. Inset: Co and Sb shifts *vs* half-Heusler lattice constant.

comparison that is often made in NMR spectroscopy. In a study of main-group half-Heusler materials [175], it was also recently shown that the metal-atom chemical shifts increase nearly linearly with the anion electronegativity. Such a comparison between anions cannot be made for the transition-metal half-Heusler materials studied here, since most of the corresponding compounds containing other pnictogen or carbon-group anions are not stable in the same structure. However, a regular trend can be seen by comparing the chemical shifts to the mean Pauli electronegativities of the 3 elements comprising each compound, as shown in Fig. 6.6.

The general trend displayed in Fig. 6.6 is an increase in shift *vs* mean electronegativity. Since in each series the atom corresponding to the nucleus being measured is held constant, increasing mean electronegativity implies that the observed nucleus experiences a nominal decrease in on-site charge. Thus, this is the same trend observed *vs* anion substitution in main-group half-Heusler compounds [175]. However, whereas in proton NMR a decrease in on-site charge will increase shift because the electron density contributes most significantly to the diamagnetic NMR shielding, here the large positive NMR shifts seen here are clearly paramagnetic shifts dominated by a Van Vleck mechanism as discussed above. The results are not completely linear, in fact for ^{59}Co and ^{121}Sb the upward trend observed for large shifts is the same as the trend identified in comparison to

the DFT results discussed here, with large chemical shifts becoming enhanced in magnitude over what is expected.

Along with the electronegativity trend, there is generally a corresponding decrease in shift *vs* increasing lattice constant, a, shown in the inset of the Fig. 6.6. (The ^{93}Nb shifts are not plotted since they are for compounds with the same lattice constant.) This trend can be connected to changes in hybridization, which will increase as a decreases, and contribute a greater mix of *d* orbitals in the conduction and valence bands, which as noted above produces the large observed paramagnetic chemical shifts by the Van Vleck mechanism. This also helps to understand the electronegativity trend, since moving to the right and upward on the periodic table, in the direction of increasing electronegativity, also corresponds to more compact orbitals and enhanced hybridization. Thus, the observed experimental trends and large NMR shifts can be understood as relating to an enhanced mix of orbitals in these compounds.

To investigate whether this might be due to effects such as stoichiometry or site disorder, we performed a volume minimization for these materials, using the PBE functional in WIEN2k, and obtained 5.948 ± 0.004 Å for TaFeSb and 5.961 ± 0.003 Å for NbFeSb. The calculated lattice constant difference between TaFeSb and NbFeSb is in a good agreement with the experimental difference, and it is also similar to other recently reported calculated values [176] indicating that the smaller size of TaFeSb lattice is an intrinsic feature. As noted above the significantly larger paramagnetic chemical shift observed in NbFeSb relative to TaFeSb is in agreement with DFT results based on the experimental results. With these large shifts dominated by hybridization among *d* orbitals, the TaFeSb shift is smaller despite the more diffuse 5*d* orbitals which might be expected to lead to enhanced hybridization. This result is likely caused by the presence of the $4f$ electrons on Ta, and the resulting contraction and energetic favoring of the Ta 6*s* over the 5*d* electrons, thus reducing the number of occupied *d* orbitals which can interact with the applied field.

6.5 Summary

In this chapter, I have investigated various half-Heusler thermoelectric materials (ZrCoSb, NbCoSn, TaFeSb and NbFeSb) using NMR as a local probe combined with DFT calculations. For

ZrCoSb, both ^{59}Co and ^{121}Sb shift and spin-lattice relaxation measurements show consistent results indicating the excitation of carriers and the existence of impurity band right below the conduction band. For NbCoSn and TaFeSb, both show Curie-Weiss-like behavior revealing paramagnetic-type defects. The constant spin-lattice relaxation rates represent the partial Fermi-level DOS of the probed site, indicating the metallic behavior at measured temperature range. ^{121}Sb NMR spin-lattice relaxation result for NbFeSb shows a clear peak due to long range dipolar interaction with local magnetic defects, confirming previous published ^{93}Nb NMR results for NbFeSb. These paramagnetic shifts can be understood as degenerate *d* bands splitting and mixing in the conduction and valence bands. The observed trends of chemical shift *vs* electronegativity and lattice constant can be connected to variations in the *d*-electron hybridization in half-Heuslers. The DFT computed results give an overall reasonable prediction of NMR chemical shifts for half-Heusler materials. The largest shifts are observed to exceed what is predicted, and I discuss a likely mechanism due to electron-electron enhanced Van Vleck susceptibility.

7. SKUTTERUDITE THERMOELECTRIC MATERIALS*

7.1 Introduction

In this chapter, I describe results for $Ba_xYb_yCo_4Sb_{12}$ and $A_xCo_4Sb_{12}$ (A = Ba, Sr), combined with transport measurements using NMR as a powerful technique to detect the electronic properties of semiconductors and thermoelectric materials. The results provide new information about the electronic behavior and the importance of defects, very close in energy to the conduction band edge in these *n*-type filled skutterudites. The materials were prepared by Prof. Uher's group at University of Michigan and measured partially by my former labmate Dr. Ali A. Sirusi and partially by myself in our lab at TAMU.

7.2 Sample Preparation and Experimental Methods

Skutterudites (space group $Im3$, shown in Fig. 7.1, visualized with VESTA [115]) of nominal composition $Ba_{0.1}Yb_{0.2}Co_4Sb_{12}$, $Ba_{0.2}Co_4Sb_{12}$, and $Sr_{0.2}Co_4Sb_{12}$ were prepared by a melting-annealing-spark plasma sintering method. The high-purity elements were weighed and mixed in the stoichiometric ratio, loaded into graphite-coated quartz tubes, and sealed in vacuum. These were placed in a furnace and heated to 1373 K at the rate of 1 K min^{-1} and held for 10 h to ensure thorough mixing of the constituents. The temperature then decreased to 1013 K at the rate of 4 K min^{-1} and held for 10 days. The furnace was then turned off and cooled to room temperature. The resulting ingots were ground to fine powders and pressed by a cold press into pellets, which were then loaded into quartz tubes again, sealed in vacuum, heated to 1013 K at the rate of 4 K min^{-1}, and held for 2 weeks to form a pure skutterudite phase. The furnace was then turned off and cooled to room temperature. The ingots were ground again to a fine powder and loaded into a graphite die for spark plasma sintering. The final sintering (for densification) was carried out at 903 K for 15 min. $Ba_{0.1}Yb_{0.2}Co_4Sb_{12}$ is the same sample prepared as reported in Ref. [41] with

*Part of this chapter is reprinted from Ref. [13] (Y. Tian, A. A. Sirusi, S. Ballikaya, N. Ghassemi, C. Uher, and J. H. Ross, Jr., "Charge-carrier behavior in Ba-, Sr- and Yb-filled $CoSb_3$: NMR and transport studies", Phys. Rev. B, vol. 99, no. 12, p. 125109, 2019.) with permission from AIP Publishing.

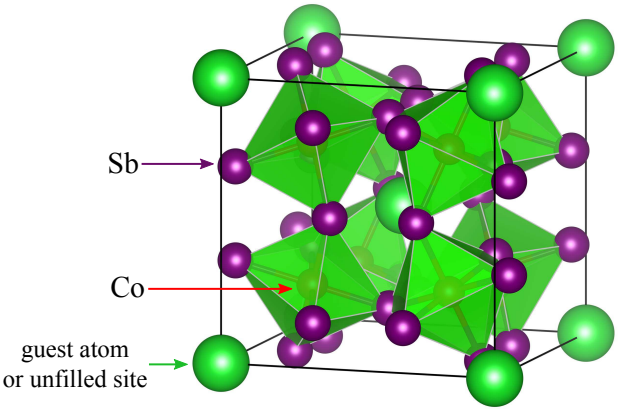

Figure 7.1: Crystal structure of filled skutterudites, $M_zT_4X_{12}$, where M is a guest atom $(0 \leq z \leq 1)$.

Table 7.1: Nominal composition, actual composition (from EPMA analysis), and *n*-type carrier concentration n_H derived from Hall measurements at room temperature.

Nominal	Actual	n_H (10^{20} cm^{-3})
$Ba_{0.1}Yb_{0.2}Co_4Sb_{12}$	$Ba_{0.07}Yb_{0.067}Co_4Sb_{11.94}$	2.29
$Ba_{0.2}Co_4Sb_{12}$	$Ba_{0.036}Co_4Sb_{11.77}$	1.80
$Sr_{0.2}Co_4Sb_{12}$	$Sr_{0.041}Co_4Sb_{11.87}$	1.00

zT approaching 1 at 800 K.

Electron probe microanalysis (EPMA) measurements including wavelength dispersive spectroscopy were performed to measure the compositions. Results indicate uniform skutterudite phases with very small composition variations. The actual compositions are listed in Table 7.1. Compared to the nominal compositions, filling fractions are smaller than the starting compositions, which is typical for $CoSb_3$-based skutterudites [177], with remaining filling elements expected to form small oxide particles. In this work, we denote $Ba_{0.1}Yb_{0.2}Co_4Sb_{12}$ as sample Ba(0.1)Yb(0.2), $Ba_{0.2}Co_4Sb_{12}$ as sample Ba(0.2) and $Sr_{0.2}Co_4Sb_{12}$ as sample Sr(0.2). Based on the filler atom densities, and assuming ion charges Yb^{3+}, Ba^{2+} and Sr^{2+}, the measured compositions correspond to $n = 4.6$, 1.0, and 1.1×10^{20} cm^{-3}, for Ba(0.1)Yb(0.2), Ba(0.2) and Sr(0.2), respectively, if

the ionized charges are donated to the conduction band. However, these can be reduced by native defects, mostly due to departure from $CoSb_3$ stoichiometry. The measured compositions indicate Co excess and Sb deficit typical for these materials, and comparable to the concentrations of filler ions, although note that these composition differences are on the same order as the absolute accuracy of the microprobe. Magnetic measurements were performed using a Quantum Design superconducting quantum interference device magnetometer. The magnetic results are shown in the Appendix indicating that the samples are non-magnetic with a dilute paramagnetic response attributed to native defects, as well as Yb^{3+} moments in the case of sample Ba(0.1)Yb(0.2).

NMR measurements were carried out by applying a custom-built system at magnetic field 9 T from 4 K to 450 K. ^{59}Co (nuclear spin $I = 7/2$) NMR spectra were obtained using a spin echo sequence with aqueous $K_3[Co(CN)_6]$ as shift reference. The spin-lattice relaxation times at the central transition lines were determined from fitting to a multi-exponential function for inversion recovery. QuadFit [178] was used to fit the spectra. High-temperature transport measurements were carried out under dynamic argon flow in the range 300 to 800 K. Carrier concentrations and Seebeck coefficients were measured using a home-made apparatus with a standard four-probe configuration. Room-temperature carrier concentrations of all samples from Hall measurements are also listed in Table 7.1. As opposed to the *p*-type behavior of pure $CoSb_3$, all samples show *n*-type behavior due to electron donation from filler atoms.

7.3 Experimental Results

7.3.1 NMR measurements

7.3.1.1 Line shapes

Fig. 7.2 shows the ^{59}Co NMR spectrum of sample Ba(0.1)Yb(0.2) at 290 K. The powder spectra exhibit the characteristic sequence of edge singularities due to the $\Delta m = 1$ nuclear transitions. The quadrupole frequency is defined as $\nu_Q = 3eQV_{zz}/[2I(2I-1)]$, where Q is the nuclear quadrupole moment and V_{zz} is the maximum principal value of the electric field gradient (EFG) tensor. The other two principal values V_{xx} and V_{yy} are equal due to the axial Co site symmetry. Compared to

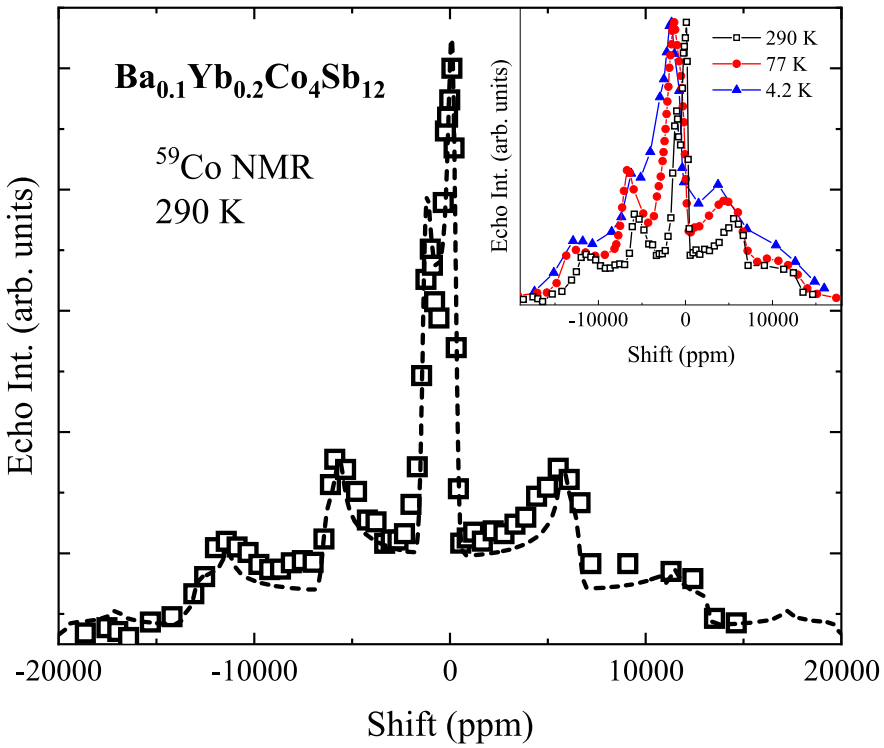

Figure 7.2: ^{59}Co NMR spectrum for sample Ba(0.1)Yb(0.2) at 290 K. The dashed line is a fit for the overall spectrum. The inset shows spectra at 4.2 K, 77 K, and 290 K, normalized to the same peak intensity.

$CoSb_3$ with $\nu_Q = 1.18$ MHz [179], the fitted room-temperature spectra (dashed line in Fig. 7.2) have $\nu_Q = 1.11 \pm 0.01$ MHz for all 3 samples. The chemical shift anisotropies for Ba(0.1)Yb(0.2), Ba(0.2) and Sr(0.2) are 1250 ppm, 1200 ppm and 1220 ppm, respectively (given as the span, $\Omega = \delta_{11} - \delta_{33}$). This is in good agreement with the value $K_{\text{ax}} = -0.039\%$ (corresponding to $\Omega = 1170$ ppm) for $CoSb_3$ reported by Lue *et al.* [180]. The reduction in ν_Q due to filler atoms is similar to the behavior of $Ca_xCo_4Sb_{12}$ and $La_xCo_4Sb_{12}$ [180, 181]. The inset of Fig. 7.2 displays spectra for sample Ba(0.1)Yb(0.2) at 4.2 K, 77 K, and 290 K, demonstrating the shift to lower frequencies along with increasing line width upon cooling. Fig. 7.3 shows a comparison of spectra for all three samples at room temperature and 77 K.

Note that in the measured frequency range, ^{121}Sb signals coexist with those of ^{59}Co, however with very large line widths. Based on NQR in La-filled $CoSb_3$, a large ν_Q of 38.8 MHz has been reported [182]. Similar results for the present materials will lead to a central transition for ^{121}Sb $\sim$1200 times wider than the ^{59}Co central transition, or about 10 MHz, and the spectral intensity correspondingly reduced by a very large factor.

7.3.1.2 Knight shifts

Fig. 7.4 shows the temperature-dependent ^{59}Co NMR isotropic shift obtained for the three samples by calculating the center of mass of the central transition ($-1/2 \leftrightarrow +1/2$) portion of the spectrum. The shift is composed of two main contributions: Knight shift and chemical shift. The Knight shift, due to unpaired spins of charge carriers and defects, provides the large temperature dependence for these samples. Thus, for simplicity, in the plot K is used to represent the entire shift, similar to what has been reported for $La_xCo_4Sb_{12}$ [181]. It can be seen that the total shift is negative, becoming more positive with temperature increasing. In Sec. 7.4, we will discuss a theoretical model for this temperature dependence in terms of increasing carrier density vs. temperature. Due to the increasing shift and broadening, close to 4 K the central transition and satellite transitions peaks merge for all three samples, which makes it difficult to isolate the shift at very low temperatures.

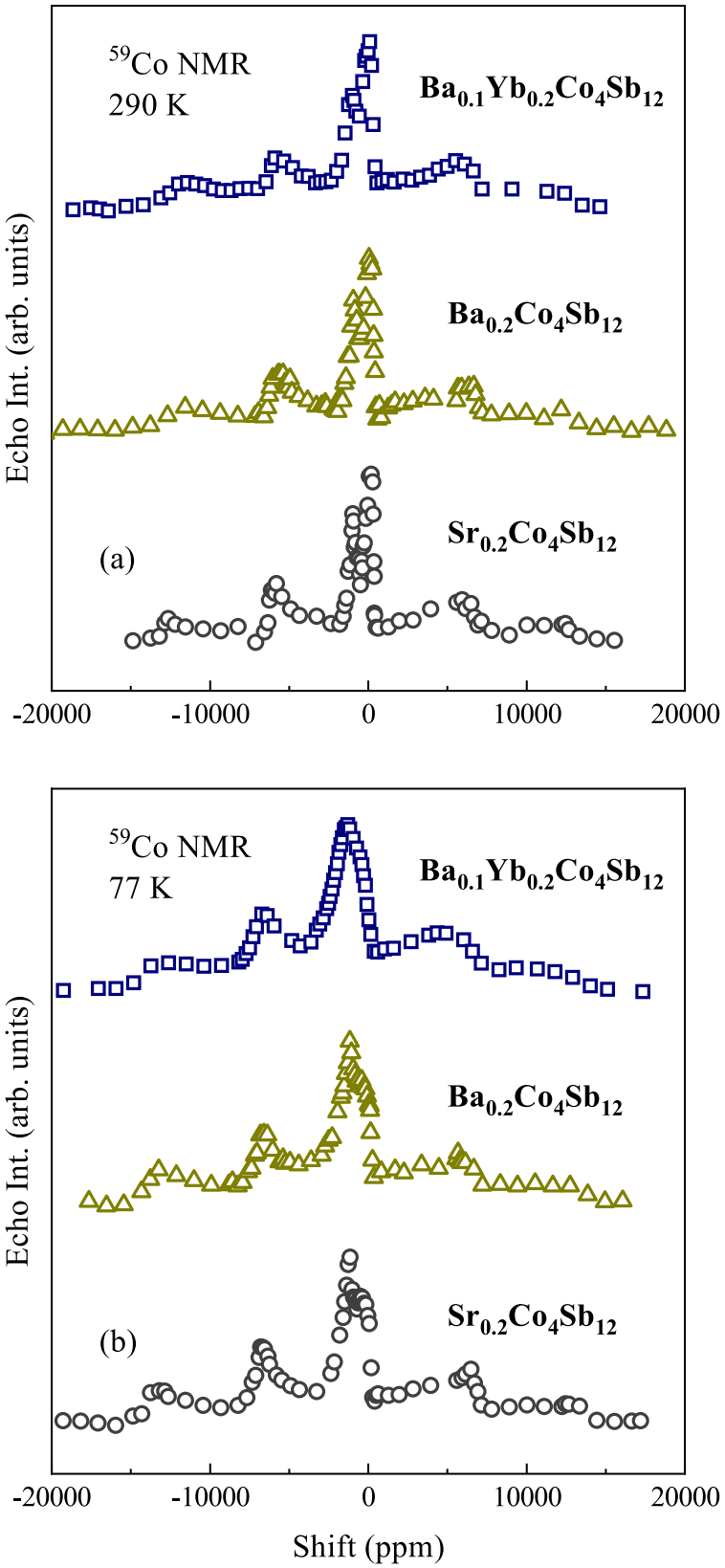

Figure 7.3: ^{59}Co NMR spectra for samples Ba(0.1)Yb(0.2), Ba(0.2) and Sr(0.2) in (a) 290 K and (b) 77 K. The data are offset vertically for clarity.

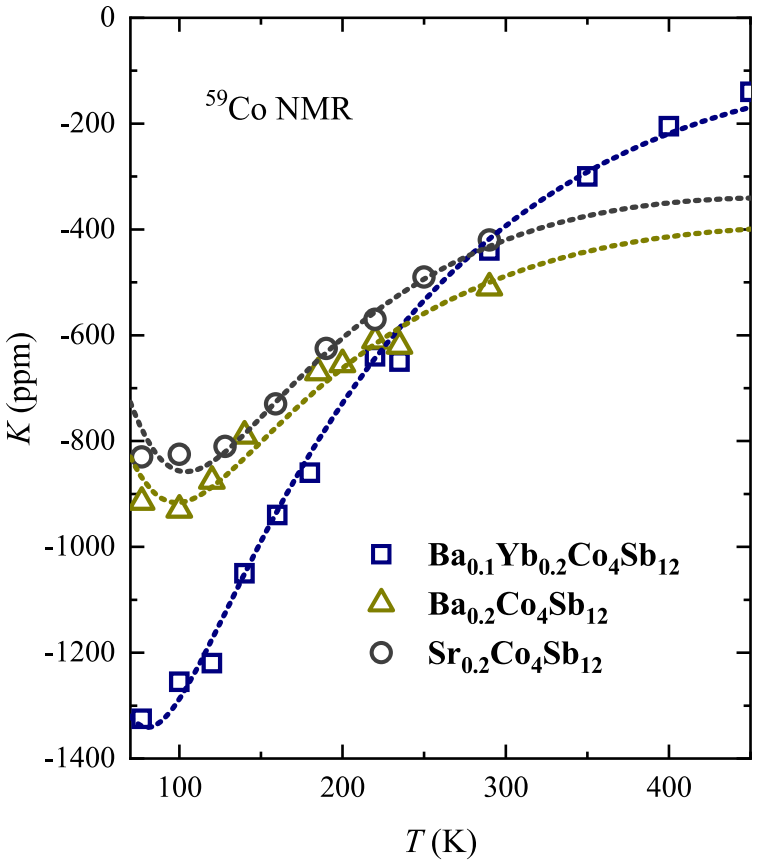

Figure 7.4: Temperature-dependent ^{59}Co NMR shift for samples Ba(0.1)Yb(0.2), Ba(0.2) and Sr(0.2). The dotted lines are fits based on the model described in the text.

7.3.1.3 Spin-lattice relaxation rates

The ^{59}Co spin-lattice relaxation rate was measured using the inversion recovery method, based on the integrated spin echo fast Fourier transform of the ^{59}Co ($I = 7/2$) lines. We irradiated only the central portion of the spectra corresponding to the peak intensity of the $-1/2 \leftrightarrow +1/2$ transitions, well known to give a multi-exponential recovery. Similar to the shift data, this was done only at 77 K and above, due to the merging of the central transition with satellite transitions at low T. For the central transition with $I = 7/2$, the recovery of the nuclear magnetization due to spin excitations can be expressed as

$$\frac{M(t) - M(\infty)}{M(\infty)} = -2\alpha(0.012e^{-\frac{t}{T_1}} + 0.068e^{-\frac{6t}{T_1}} + 0.206e^{-\frac{15t}{T_1}} + 0.714e^{-\frac{28t}{T_1}}). \quad (7.1)$$

Here, α is a fractional value derived from the initial conditions, $M(t)$ is the nuclear magnetization at time t, and $M(\infty)$ represents the asymptotic signal. Each experimental value was obtained by a fit to Eq. (7.1). The resulting $1/T_1$ values are shown in Fig. 7.5.

7.3.2 Transport measurements

Carrier concentrations (n_H) for samples Ba(0.2) and Sr(0.2) obtained by Hall measurements from 4 K to 300 K are plotted in Fig. 7.6, with the inset showing data from room temperature to 773 K of sample Ba(0.1)Yb(0.2) extracted from Ref. [41]. Fig. 7.7 shows the Seebeck coefficients of all samples from 300 K to 800 K. Both of these sets of results have the expected sign corresponding to *n*-type materials. Although the increase in n_H of Fig. 7.6 could be attributed to excitation of holes and electrons across a very small band gap on order of 30-50 meV, the Seebeck results generally support non-compensated behavior with a larger band gap consistent with other experimental results [183, 184] and calculations [185–187], with negligible hole contribution at temperatures of the NMR measurements. The decrease in S above 400 K observed for the Ba- and Sr-filled samples could possibly indicate the excitation of holes above this temperature [188], although there are also alternative explanations for this behavior as will be discussed in Sec. 7.5.

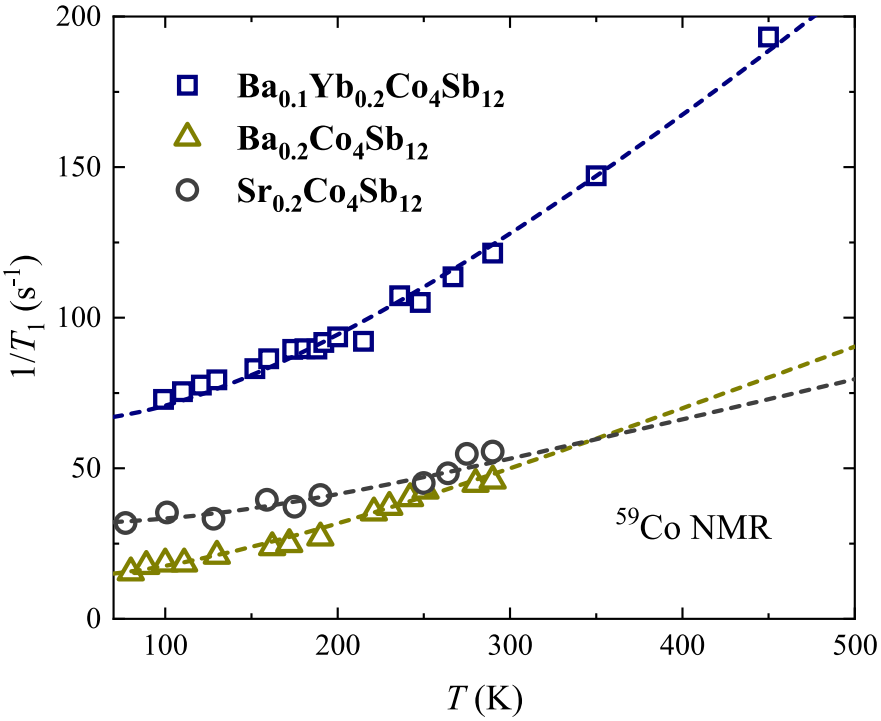

Figure 7.5: $1/T_1$ vs. T for samples Ba(0.1)Yb(0.2), Ba(0.2) and Sr(0.2). The dashed lines are fits as described in the text.

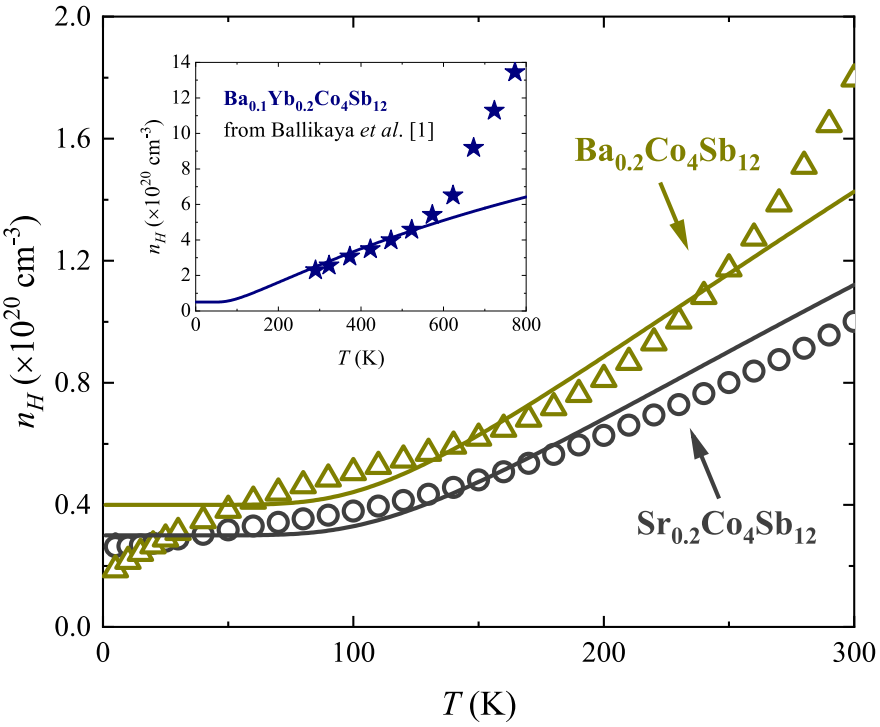

Figure 7.6: Carrier concentration vs. T from 4 K to 300 K for samples Ba(0.2) and Sr(0.2). Inset shows n_H vs. T for sample Ba(0.1)Yb(0.2) from room temperature to 773 K [41]. Solid curves: conduction-band carrier concentration ($n_{\rm CB}$); model described in text.

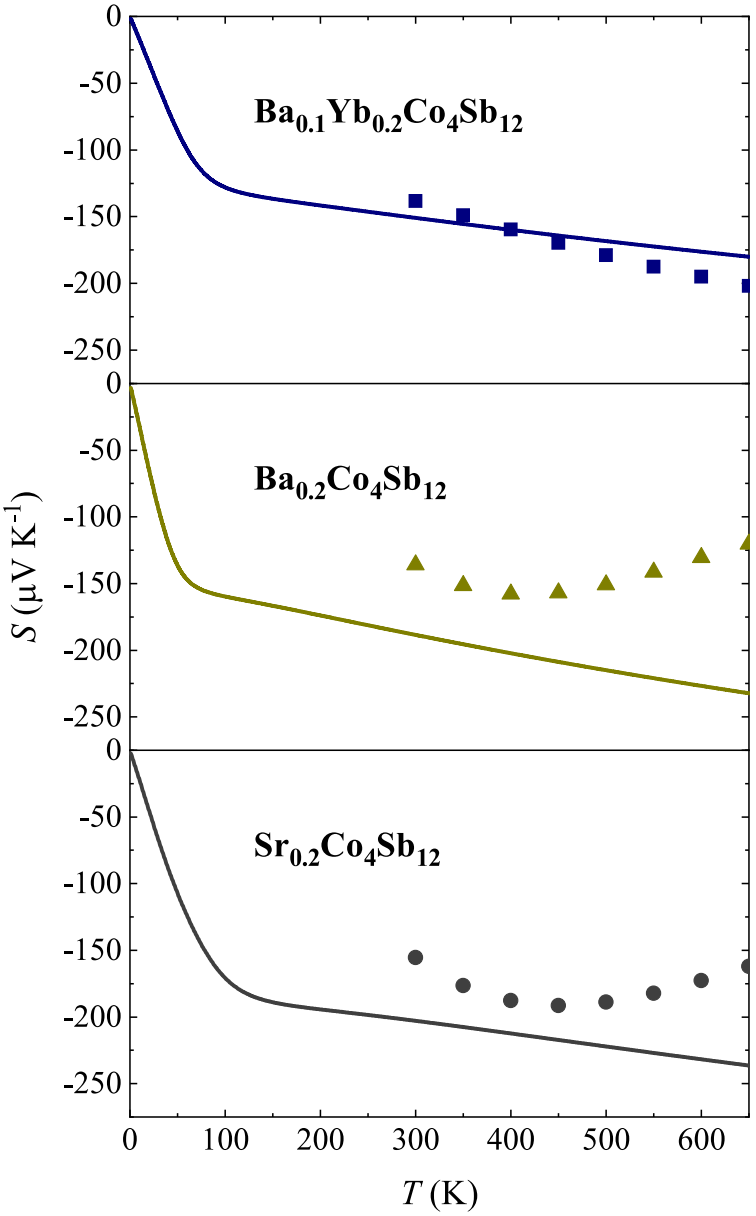

Figure 7.7: Seebeck coefficient vs. T from 300 K to 650 K for samples Ba(0.1)Yb(0.2), Ba(0.2) and Sr(0.2). Theoretical curves are shown superposed on each plot.

7.4 Theoretical Modeling and Analysis

To analyze the experimental data, we developed a formalism for the interaction between nuclei and carriers in the conduction band, allowing for arbitrary carrier densities rather than treating the extreme metallic or non-degenerate limit. The model assumes that all carriers reside in the conduction band.

The Knight shift (K) reflects the local effective magnetic field at the nuclei due to conduction electrons, given by

$$K = \frac{\Delta\nu}{\nu_0} = \frac{H_{\text{HF}}\chi_s^e}{\mu_B}, \tag{7.2}$$

where H_{HF} represents a hyperfine field. Note that conduction band edge has been shown to be dominated by Co d-states [189]. If the interaction is Fermi contact, this is defined by $H_{\text{HF}} = \frac{8\pi}{3}\langle|\varphi_k(0)|^2\rangle_{E_F}\mu_B$, however, since d electrons are dominant here, H_{HF} is instead the core polarization hyperfine field [190, 191]. For ^{59}Co, we used the measured value of this field, -21.7 T [192]. χ_s^e is the electron spin susceptibility which can be calculated according to the average carrier concentration per Co atom $N_{\text{atom}}(\mu) = n(\mu) \times V_{\text{atom}}$,

$$\chi_s^e \cong \frac{\mu_B}{2H}(g^*\mu_B H)\frac{\partial N_{\text{atom}}}{\partial\mu} = \frac{g^*}{2}\frac{\partial N_{\text{atom}}}{\partial\mu}\mu_B^2, \tag{7.3}$$

in which V_{atom} is the average volume per Co atom and μ is the chemical potential. $n(\mu)$ is defined by

$$n(\mu) \equiv \int g(E)f(E,\mu)dE, \tag{7.4}$$

where the conduction band density of states is given by

$$g_{\text{CB}}(E) = \begin{cases} \frac{\sqrt{2}Nm^{*3/2}}{\pi^2\hbar^3}\sqrt{E-E_C}, E \geq E_C \\ 0, E < E_C \end{cases} \tag{7.5}$$

with N the number of minima and m^* the effective mass in the band edge, assumed to be parabolic.

The Fermi function is,

$$f(E,\mu) = \frac{1}{e^{\frac{E-\mu}{kT}}+1}. \tag{7.6}$$

By substituting Eqs. (7.3), (7.4), (7.5) and (7.6) into Eq. (7.2) and letting $x = E - E_C$, we can derive

$$K = K_0 + \frac{A_1}{T}\int_0^\infty \frac{\sqrt{x}e^{-\frac{E_C-\mu+x}{kT}}}{(e^{-\frac{E_C-\mu+x}{kT}}+1)^2}dx, \tag{7.7}$$

with $A_1 = H_{\text{HF}} g^* \mu_B N V_{\text{atom}} {m^*}^{3/2}/\sqrt{2}\pi^2\hbar^3 k$ and the constant term K_0 representing an additive chemical shift and background Knight shift.

The T_1 relaxation process can be understood on the basis of scattering from initial occupied electron states to final unoccupied states. Note, there has been speculation that localized anharmonic modes (or "rattling" modes) affects the thermal conductivity in these skutterudites, although recent evidence [193] points to other intrinsic mechanisms for the low thermal conductivity. We find no evidence for a "rattling" contribution to the T_1 [14, 194], and show here that a purely electronic mechanism explains the T_1 results very well. According to Fermi′s golden rule, the transition rate from state i to state f is given by [172]

$$\Gamma_{i\to f} = \frac{2\pi}{\hbar}|\langle f|V|i\rangle|^2 \delta(E_f - E_i), \tag{7.8}$$

where $V = H_{\text{HF}}\gamma_n\hbar\mathbf{I}\cdot\mathbf{S}$ is the interaction providing the scattering mechanism. As a result, $1/T_1$ can be expressed by [195]

$$\frac{1}{T_1} = \frac{1}{2}\iint \Gamma_{i\to f}\Big(g_{\text{CB}}(E_i)f(E_i)\Big)\Big(g_{\text{CB}}(E_f)[1-f(E_f)]\Big)dE_i dE_f, \tag{7.9}$$

where $E_i \approx E_f$ represent initial and final states, respectively. By substituting Eqs. (7.5), (7.6) and (7.8) into Eq. (7.9),

$$\frac{1}{T_1} = \frac{1}{T_{1C}} + A_2\int_0^\infty \frac{xe^{-\frac{E_C-\mu+x}{kT}}}{(e^{-\frac{E_C-\mu+x}{kT}}+1)^2}dx, \tag{7.10}$$

with $A_2 = 8H_{\text{HF}}^2\mu_B^2 N^2 V_{\text{atom}}^2 {m^*}^3\gamma_n^2/\pi^3\hbar^7\gamma_e^2$ and $1/T_{1C}$ representing other contributions to the re-

laxation rate. Note that in the highly degenerate limit ($\mu - E_C \gg kT$), these results can easily be shown to simplify to $K =$ const. and $1/T_1 \propto T$, as often seen for heavily doped semiconductors [47]. Here, we consider the more general case, since $\mu - E_C \approx kT$ for much of the range considered here.

The carrier concentration in the conduction band, n_{CB}, can be derived by substituting Eqs. (7.5) and (7.6) into Eq. (7.4),

$$n_{\mathrm{CB}} = \frac{\sqrt{2}Nm^{*3/2}}{\pi^2\hbar^3}\int_0^\infty \frac{\sqrt{x}}{e^{\frac{E_C-\mu+x}{kT}}+1}dx. \tag{7.11}$$

Also the Seebeck coefficient can be calculated by $S = -\frac{1}{eT}\frac{\mathscr{L}^{(1)}}{\mathscr{L}^{(0)}}$, which contains the function, $\mathscr{L}_{ij}^{(\alpha)} \equiv e^2\int\frac{d^3\mathbf{k}}{4\pi^3}(-\frac{\partial f}{\partial E})\tau v_i v_j(E-\mu)^\alpha$ [139]. By substituting Eqs. (7.5) and (7.6), the Seebeck coefficient is expressed as

$$\begin{aligned} S &= -\frac{1}{eT}\frac{\int(df/dE)g(E)\tau(E)E(E-\mu)dE}{\int(df/dE)g(E)\tau(E)EdE} \\ &= -\frac{1}{eT}\frac{\displaystyle\int_0^\infty \frac{e^{-\frac{E_C-\mu+x}{kT}}}{(e^{-\frac{E_C-\mu+x}{kT}}+1)^2}\tau(x)x^{3/2}(x-\mu)dx}{\displaystyle\int_0^\infty \frac{e^{-\frac{E_C-\mu+x}{kT}}}{(e^{-\frac{E_C-\mu+x}{kT}}+1)^2}\tau(x)x^{3/2}dx}, \end{aligned} \tag{7.12}$$

where the second form assumes explicitly that $g_{\mathrm{CB}} \propto (E-E_C)^{1/2}$. Typically, $\tau(E)$ is considered proportional to $(E-E_C)^r$ with $-3/2 \le r \le 1/2$ depending on the scattering mechanism [196].

Fig. 7.8 shows the simple model for $g(E)$ found to give consistent agreement with the results, with shallow defect states assumed to be represented by a single Dirac delta function due to a superposition of isolated in-gap states at energy E_D. This leads to the low-temperature increase in n_H, with μ in the conduction band at $T = 0$ due to electrons donated by the filler atoms. The conservation of total charge, $n_D(0) + n_{\mathrm{CB}}(0) = n_D(T) + n_{\mathrm{CB}}(T)$, determines the temperature dependence of the chemical potential μ, where n_D represents the electron concentration in shallow

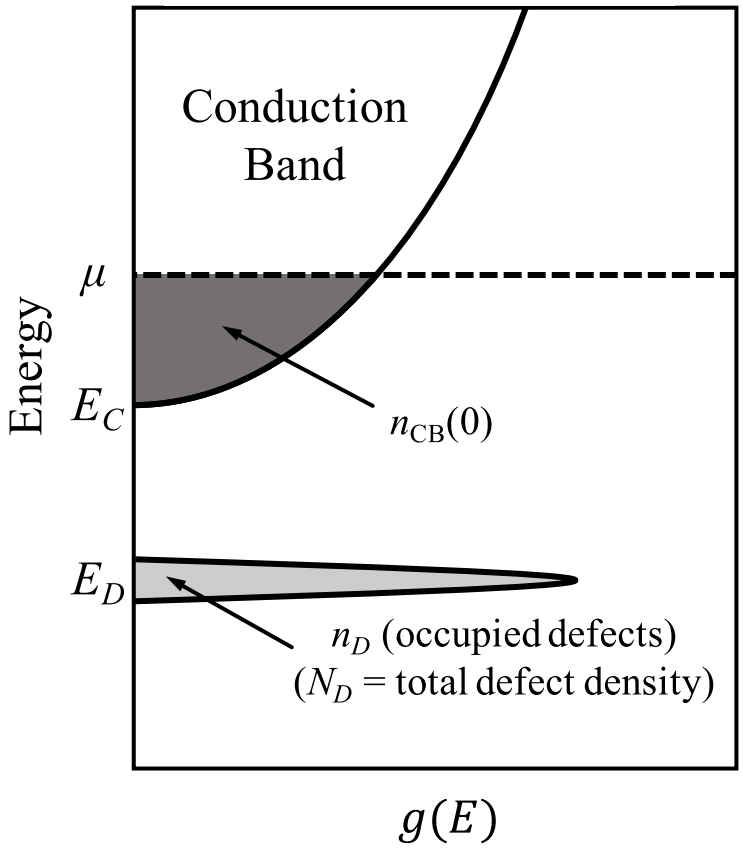

Figure 7.8: The general model for the total density of states used here. E_C, E_D and μ are the positions of conduction band minimum, shallow defect state and chemical potential, respectively. n_{CB} represents the carrier concentration in the parabolic conduction band. For simplicity this is pictured for $T = 0$ for which $n_{\text{CB}}(0)$ is the limiting value. n_D represents the electron concentration in shallow defect states (light gray area), with available level density N_D, assumed to be a Dirac delta function.

Table 7.2: Parameters of theoretical fittings for samples Ba(0.1)Yb(0.2), Ba(0.2) and Sr(0.2). E_D (meV) is the position of defect state relative to E_C, N_D (10^{20} cm^{-3}) the concentration of defect state, $n_{\text{CB}}(0)$ (10^{20} cm^{-3}) the CB carrier concentration at 0 K, $m_{\text{eff}} = N^{2/3}m^*$ (m_e) the thermodynamic effective mass, g^* the effective g-factor, K_0 (ppm) the addictive shift and $1/T_{1C}$ (s^{-1}) the spin-lattice relaxation rate at 0 K.

Sample	E_D	N_D	$n_{\text{CB}}(0)$	m_{eff}	g^*	K_0	$1/T_{1C}$
Ba(0.1)Yb(0.2)	-26	15	0.5	3.8	-8	-3560	61
Ba(0.2)	-35	6	0.4	3.4	-8.5	-2570	12
Sr(0.2)	-38	4.5	0.3	3.2	-9	-2230	30

defect states (light gray area shown in Fig. 7.8). The relationship of μ and T is thus given by

$$\begin{aligned} N_D + n_{\text{CB}}(0) &= \int N_D \delta(E - E_D) f(E) dE + n_{\text{CB}} \\ &= N_D \frac{1}{e^{\frac{E_D - \mu}{kT}} + 1} + n_{\text{CB}}, \end{aligned} \tag{7.13}$$

where $N_D = n_D(0)$ and $n_D(T)/N_D$ are the concentration of shallow states and the filled fraction at a given T, respectively, and $n_{\text{CB}}(0)$ is the carrier concentration at $T = 0$. Then for each temperature, the corresponding chemical potential can be obtained by numerically solving Eq. (7.13).

Figs. 7.4-7.7 show fitted theoretical curves based on this model. Since the numerical solution of several integral equations is required, we cannot least-squares fit all parameters at once. However, we find that the carrier concentration is much more sensitive to effective mass than the other quantities, so the thermodynamic effective mass, $m_{\text{eff}} = N^{2/3}m^*$ and $n_{\text{CB}}(0)$ were fitted to the carrier concentration with values shown in Table 7.2. Both for Ba(0.2) and Sr(0.2), n_H exhibits a decrease below about 50 K, apparently a trend toward localization at the temperatures, so we fitted the data above this temperature. The results for m_{eff} are in close agreement with each other, as might expected for rigid-band filling of states at the CB edge. Then by fitting K and $1/T_1$ together, E_D, N_D and, g^* were optimized, giving the results also listed in Table 7.2. Values of g^* are between -8 and -9, comparable to that of the holes, with smaller m^*, having $g^* = -10.1$ as reported by Arushanov *et al.* [197].

While the gradual increase of Knight shift and $1/T_1$ vs. temperature can be understood in terms of an increasing number of carriers excited into CB, the terms K_0 and $1/T_{1C}$ can be interpreted as due to the susceptibility of electrons in the localized levels. To the extent that Coulomb interactions allow unpaired spins within these states, a Curie-type susceptibility contribution is expected at low temperatures, the presence of which is confirmed by the large negative NMR shifts at helium temperatures in all three samples. These shifts are responsible for the overlapping of transitions at low temperatures, which prevented separation of the central transition shifts in this limit as discussed above. Note that the mechanism involves contact with Co d-states through the negative $H_{\rm HF}$ for Co, as opposed to dipole coupling for dilute local moments which provides an additional broadening mechanism for Yb^{3+} moments in sample Ba(0.1)Yb(0.2), but no net shift contribution [15]. Other contributions to the shifts include differences in chemical shift, and above 77 K we find that an added constant term (K_0) can best fit the temperature dependence of these shifts.

The localized-electron contribution to $1/T_1$ can be modeled directly in terms of the dynamical susceptibility of such localized spins. From general considerations, it is often found [198, 199] that $1/T_1 \propto k_B T \chi_0 \tau$, where χ_0 is the DC susceptibility and τ is an electron spin lifetime. For sufficiently concentrated localized spins, τ can approach a constant due to spin diffusion, even for carriers which do not contribute to the electrical conductivity, and with $\chi \propto 1/T$, this gives a constant contribution to $1/T_1$. Similar results are obtained for Si:P near its metal-insulator transition [195, 199]. The term ($1/T_{1C}$) is thus expected to be due to such a contribution, and it seems reasonable that sample Ba(0.1)Yb(0.2), for which we obtained the largest density of localized states (N_D), this contribution to $1/T_1$ is found to be the largest.

The resulting theoretical transport curves for all three samples are shown in Figs. 7.6 and 7.7. With the chemical potentials solved by Eq. (7.13) plugged into Eq. (7.11), the theoretical curves describe the temperature-dependent n_H quite reasonably. The deviation of the theoretical n_H from the experimental data above 600 K for sample Ba(0.1)Yb(0.2) is likely due to carriers excited to a second band in higher temperature with a corresponding increase in effective mass [200]. With no adjustable parameters, the theoretical curves for Seebeck coefficient were drawn directly

from Eq. (7.12) as shown in Fig. 7.7. For these plots, $\tau(E)$ was taken to be proportional to $(E - E_C)^r = (E - E_C)^{-1/2}$ due to the acoustic phonon deformation potential mechanism. This mechanism is shown to provide a good agreement for materials with complex structures and multi-valley Fermi surfaces [201], although there are indications that in some substituted skutterudites the mechanism and exponent r may change vs. T [141]; this would have the effect of scaling the resulting $S(T)$ curves vertically. A distribution of defect energies (E_D) would also explain the softer turn-on apparent in the $S(T)$ data, however, our simple model successfully predicts both the sub-linear temperature dependence and the approximate magnitudes of $S(T)$, without adjustment of the parameters.

7.5 Discussion

The model of Fig. 7.8 provides a consistent picture of both the transport and NMR results and thus indicates the importance of states near the conduction band edge in filled $CoSb_3$. This differs from unfilled $CoSb_3$, for which native deep acceptor states are believed to dominate the behavior [54, 59], although recent experimental evidence also indicates *n*-type behavior for the case of large Sb deficit [55].

In our model, the valence band is completely filled with negligible hole density over the measured temperature range. Thus we do not probe the band gap from VB minimum to CBM minimum directly. However, from our results it appears that previous results showing evidence for excitation across a gap of order tens of milli-electron volts [179, 197, 202] are likely also dominated by defect levels close to the CB, while the relatively larger band gaps obtained by other techniques [183, 184, 203–205] are consistent with what we propose. Computational results based on DFT and more advanced techniques generally indicate a band gap in the range 0.2 to 0.6 eV for $CoSb_3$ [59, 200, 206] with relatively small changes due to filler atom densities comparable to those in our samples [185, 207]. Our results thus demonstrate that a larger gap combined with the presence of additional donor states can explain previous inconsistencies in the reported band gap. Note that while the calculated chemical potential positions in this model dip toward the CB edge as the temperature rises, they remain far above the VB edge, such that our assumption of negligible

hole density remains valid. With the VB effective mass ratio reported to be $m_h^*/m_e = 0.24$ [179], we obtained hole densities by direct integration (e.g. similar to Eq. (7.11)) for the Sr(0.2) sample, which in the numerical results has the smallest chemical potential. At 300 K, for a band gap at the low end of the range quoted above (0.2 eV) we obtain a hole density 1×10^{16} cm^{-3}, and orders of magnitude smaller as the gap increases. Thus over the range of expected behavior the VB has a negligible contribution to the transport and NMR behavior.

Regarding the origin of the defect states shown to sit near the conduction band edge, computational results give a possible explanation based on the presence of composite defects. While off-stoichiometric $CoSb_3$ is usually *p*-type because of acceptor-like defects, Co interstitial pairs are also proposed as *n*-type [59] or *p*-type [54] defects. These pairs are believed to form only at temperatures below that of typical processing conditions, however Hu *et al.* recently indicated that La filling combined with Sb di-vacancies can form shallow defect states near the conduction band minimum [207]. By analogy with this result, it seems likely that the defects observed here are associated with composite defects induced by the filler atoms (Ba, Sr, and Yb). The fitted values in Table 7.2 bear this out; donor charges N_D approximately three times larger than the expected filler atom charges point to such composite defects making up the donor states rather than the charges associated with the filler atoms themselves. The difference is comparable to the density of Co excess/Sb deficiency, and thus it appears that the filler atoms tie up these native defects, producing the donor states observed here.

The effective masses for all three samples are quite close to each other and in good agreement with the predicted $m_{\text{eff}} \approx 3.4\, m_e$ from modeling and experimental results for $n = 1 \times 10^{20}$ cm^{-3} as reported by Caillat *et al.* [184]. In Ref. [200], a slightly smaller $m_{\text{eff}} \approx 2.8\, m_e$ was obtained for $n = 2 \times 10^{20}$ cm^{-3}, but note that this was derived from Seebeck coefficient results assuming a degenerate limit. However, we find that all samples begin to deviate from this limit, along with a non-constant n_H, above room temperature.

As one of the most promising thermoelectric systems, a clear picture of the overall electronic structure of $CoSb_3$-based materials can give a better understanding of the transport results, which

will directly help to design high-zT thermoelectric materials. Also, since carrier donation from filler atoms is needed to optimize thermoelectric performance, a good understanding of defect states and impurity bands will be significant for thermoelectric device design. In addition, as we have shown, NMR can be a very effective tool for such analysis.

7.6 Summary

In this chapter, NMR and transport results of filled skutterudites $Ba_xYb_yCo_4Sb_{12}$ and $A_xCo_4Sb_{12}$ ($A =$ Ba, Sr) are reported to demonstrate the existence of a shallow defect level below conduction band minimum. To fit the experimental results, a simple but effective theoretical model was established by assuming the defect states to be represented by a single narrow peak in the density of states. The NMR and transport results were analyzed in a very general way allowing the Hall effect as well as Knight shift and T_1 results to be fitted numerically as the carriers slowly changed from metallic to non-degenerate situation. These fits yielded an effective mass in good agreement with predicted values and indicated that the gradual changes in Hall coefficient observed at low temperatures in filled $CoSb_3$ are associated with a defect state positioned close to the conduction band minimum. In addition, Seebeck coefficient data were also treated within the same general model and found to agree with parameters derived from the other measurements.

8. TOPOLOGICAL CHALCOGENIDE $ZrTe_5$*

8.1 Introduction

In this chapter, I describe ^{125}Te NMR measurements supported by electronic structure calculations, characterizing the 3D Dirac topological nature of $ZrTe_5$. The material was prepared and measured by myself in our lab at TAMU. The DFT calculations were done by my labmate Dr. Nader Ghassemi. The found phase transition is shown to proceed from WTI to STI with increasing temperature associated with the bulk gap closing and reopening, while direct evidence of band inversion at the topological phase transition is established based on NMR shift measurements, demonstrating a significant capability for probing quantum materials.

8.2 Sample Preparation

Figs. 8.1(a)-(b) show the $ZrTe_5$ crystal structure, which can be treated as $ZrTe_3$ chains connected by Te_2 bridging atoms. $ZrTe_5$ single crystals were prepared by chemical vapor transport (CVT). A $ZrTe_5$ precursor was prepared by reacting stoichiometric amounts of Zr (99.9%) and Te (99.999%) in evacuated ampules at 500 °C, then mixed with 5 mg/cm^3 iodine and sealed in a quartz ampule under vacuum. The ampule was held in a 530 to 470 °C gradient for one week, yielding needlelike single crystals.

8.3 Experimental and Computational Methods

Cameca SXFive microprobe measurements indicated a uniform phase $ZrTe_{5.02\pm0.02}$, equivalent within resolution to the stoichiometric composition, and larger Te content than in some other reports [208, 209]. No I or Hf was detected. Transport measurement showed a resistance anomaly at $\sim$125 K, typical for CVT samples. NMR experiments utilized a custom-built spectrometer at a fixed field $H_0 \approx 9$ T, aligning many crystals with H_0 parallel to a. Note that $H_0 \parallel a$ minimizes magnetic quantum effects [208], providing a probe of an essentially unperturbed electronic structure.

*Part of this chapter is reprinted from Ref. [96] (Y. Tian, N. Ghassemi, and J. H. Ross, Jr., "Dirac electron behavior and NMR evidence for topological band inversion in $ZrTe_5$," Phys. Rev. B, vol. 100, no. 16, p. 165149, 2019.) with permission from APS.

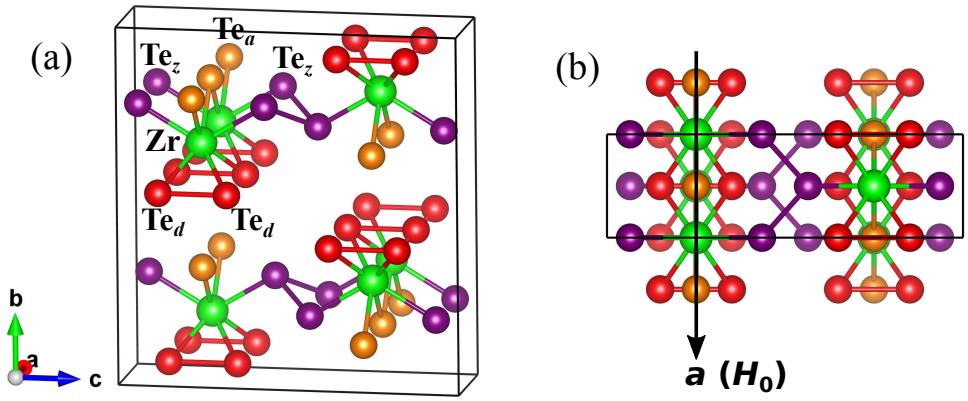

Figure 8.1: (a) Crystal structure of $ZrTe_5$. Te sites include apical (Te_a), dimer (Te_d), and zigzag (Te_z) with occupation ratio 1:2:2. (b) *a*-*c* plane view showing the long dimension of the needlelike crystals (*a*-axis) coinciding with the applied NMR field (H_0).

^{125}Te shifts were calibrated by aqueous $Te(OH)_6$ and adjusted for its $\delta = 707$ ppm paramagnetic shift to the dimethyltelluride standard [210]. Density functional theory (DFT) calculations were performed with WIEN2k [113] using Perdew, Burke, and Ernzerhof (PBE) exchange-correlation potential, with spin-orbit coupling, a *k*-point grid of $15 \times 15 \times 4$, and atom positions from experiment [211]. Calibration of calculated ^{125}Te chemical shifts was based on the computed ZnTe shift [212].

8.4 Experimental Results

8.4.1 Line shapes and shifts

Fig. 8.2(a) shows a room-temperature ^{125}Te NMR spectrum ($I = 1/2$), with peaks labeled corresponding to the three Te sites: apical (Te_a), dimer (Te_d), and zigzag (Te_z) [Fig. 8.1]. Fig. 8.2(b) displays spectra *vs* temperature. Note that the number of nuclei in the expected topological edge states is negligible compared with that of the bulk so that the spectra represent the bulk. Fig. 8.2(c) shows shifts obtained by fitting to three Gaussian peaks. Site assignments aided by DFT will be discussed below.

While the Te_d and Te_a sites show similar behavior, steadily decreasing with temperature, Te_z behaves somewhat differently, with a consistently larger line width, and about 25% smaller spectral

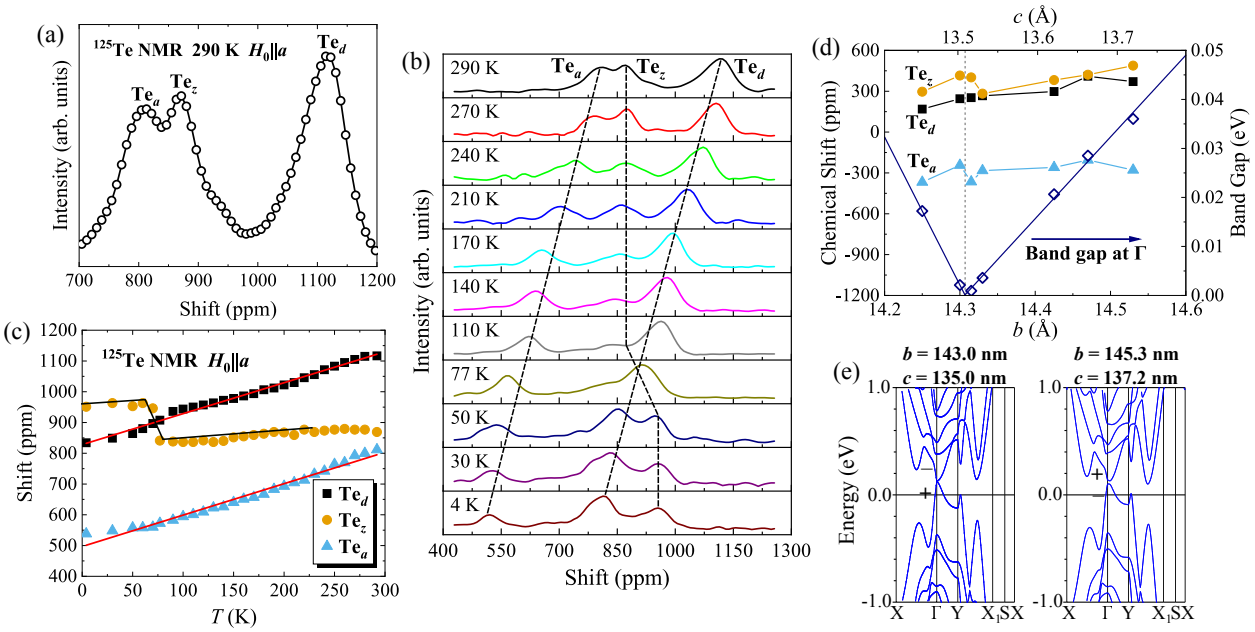

Figure 8.2: (a) Aligned crystal room-temperature ^{125}Te NMR spectrum for $ZrTe_5$. (b) Temperature dependence to 4.2 K. Dashed lines: guides to the eye. (c) Fitted shift *vs* temperature for 3 sites. (d) Calculated band gap at Γ and chemical shifts *vs* *b* and *c* crystal dimensions. Dashed line represents band inversion position. (e) Band structures calculated just below inversion point and for experimental lattice parameters.

area than expected. With the $ZrTe_3$ chain believed to act as a rigid frame [211], small separations and distortions of the layers apparently affect most strongly the zigzag sites causing the enhanced broadening.

8.4.2 Spin-lattice relaxation

Spin-lattice relaxation, measured by inversion recovery, could be well fitted to a single exponential $M(t) = (1 - Ce^{-t/T_1})M(\infty)$, giving $1/T_1T$ values shown in Fig. 8.3. The observed minimum can be regarded as indicating a density of states minimum at E_F for this temperature. In metals, $1/T_1T$ is often dominated by *s*-electron Fermi contact and proportional to $g^2(E_F)$. However, with Dirac and band-edge states in $ZrTe_5$ dominated by Te *p* states [75], core polarization and dipolar hyperfine coupling would be expected to play more important roles. In most cases, these terms cause significant site dependence. Instead, the behavior shown in Fig. 8.3 is independent of site near the minimum.

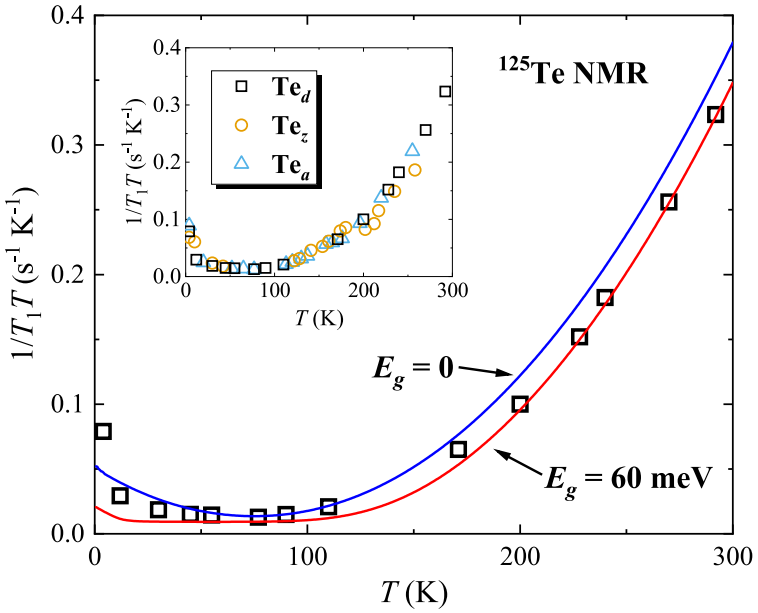

Figure 8.3: $1/T_1T$ *vs* temperature for Te$_d$ site. Upper curve: $E_g = 0$, that is, gapless Dirac semimetal in the whole temperature range, which overestimates $1/T_1T$ except near the Lifshitz T_c. Lower curve: $E_g = 60$ meV, which matches the data far from T_c. Inset: $1/T_1T$ *vs* temperature for all sites, showing similar relaxation characteristics.

8.5 Discussion

8.5.1 Relaxation in Dirac electron system

A recent model of spin-orbit-based NMR relaxation in 3D Dirac and Weyl systems accounts for this behavior very well. In this theory [213, 214], fluctuations in Dirac-type orbital currents are responsible for the relaxation. The orbital hyperfine interaction introduces a $1/k^2$ contribution to the momentum sum determining $1/T_1T$ [102, 213], thus connecting to fluctuations that are more extended in space than the typical local contributions, explaining the site-independence. The result is a quadratic $1/T_1T$ minimum *vs* chemical potential (μ) in the zero-T limit as the Dirac point is traversed. This model was also applied to TaP [102], where μ pinned to a Weyl point leads to T^2 behavior. Here I show that this applies to the analogous case of Dirac electrons with a small gap, with μ steadily advancing through the Dirac point.

For massive Dirac fermions, the orbital contribution is [214]

$$\frac{1}{T_1T} = \frac{2\pi}{3}\mu_0^2\gamma_n^2e^2c^{*4} \times \int_{-\infty}^{\infty} dE\left[-\frac{\partial f(E,\mu)}{\partial E}\right]\frac{g^2(E)}{E^2}\ln\frac{2(E^2-\Delta^2)}{\omega_0|E|}, \tag{8.1}$$

with $E = \pm\sqrt{c^{*2}k^2+\Delta^2}$. In addition, $f(E,\mu)$ is the Fermi function, and $g(E)$ is the Dirac electron density of states,

$$g(E) = \frac{|E|\sqrt{E^2-\Delta^2}}{2\pi^2c^{*3}}\theta(E^2-\Delta^2), \tag{8.2}$$

with $\theta(E^2-\Delta^2)$ a step function enforcing no states in the $E_g = 2\Delta$ gap. The result is

$$\frac{1}{T_1T} = \frac{\mu_0^2\gamma_n^2e^2k_B\beta}{6\pi^3c^{*2}\hbar^3} \times \int\limits_{|E|\geq\Delta} dE\frac{(E^2-\Delta^2)\ln[2(E^2-\Delta^2)/\hbar\omega_0|E|]}{4k_BT\cosh^2[(E-\mu)/2k_BT]}, \tag{8.3}$$

where β is an overall scale factor [102] accounting for details of the Bloch wavefunctions.

8.5.2 *T*-dependent band gap

In fitting $1/T_1T$, I assumed μ is positioned in the conduction band at low temperature, and advances through the Dirac point as T increases, consistent with the observed *n*- to *p*-type change [208,215] as well as ARPES measurements [89]. By numerically integrating Eq. (8.3), I found that a linear decrease in μ *vs* T gives results that agree with the higher-temperature data, but only with the gap set to $2\Delta \approx 60$ meV. However, close to the minimum, the smaller curvature indicates a gap approaching zero. This is illustrated in Fig. 8.3 for the Te$_d$ site with gapless and gapped ($E_g = 60$ meV) cases shown by the labeled curves, with a very small $1/T_1T = 0.009$ s^{-1} K^{-1} term added to account for other relaxation contributions. In the calculation, I replaced c^{*3} by the product of the three experimental Fermi velocities reported by Tang *et al*. [74], leading to $c^* = 2.1 \times 10^5$ m/s. The fitting at high temperatures gives $\beta = 5.6 \times 10^6$, which can be compared to $\beta = 8.6 \times 10^6$ reported for the Weyl case for TaP [102]. β and c^* appear only in the prefactor of Eq. (8.3); their variation leads to a small scaling of the overall E_g results without affecting the final results in a significant way.

Within this model, I set $\mu = \alpha(T - T_c)$ and fitted Δ *vs* T. This yielded $\alpha = -5k_B$, $T_c = 85$

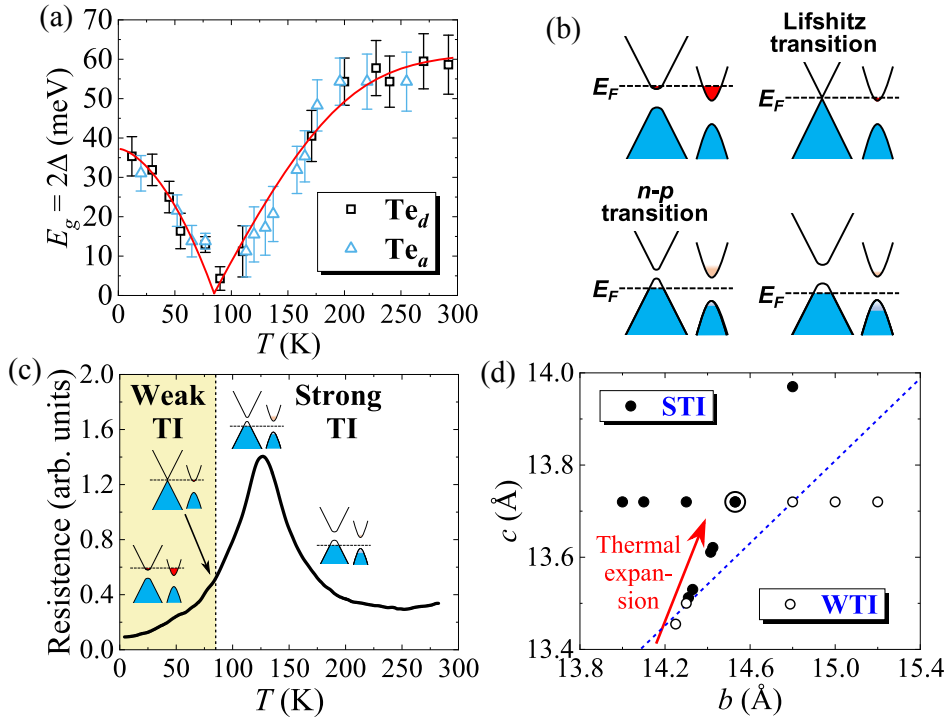

Figure 8.4: (a) Fitted band gap *vs* temperature obtained from $1/T_1T$ for Te$_d$ and Te$_a$ sites. Solid curves: guides to the eye. (b) Schematic of T-dependent chemical potential and band structure. (c) Relation between resistance and electronic structure, with WTI (shaded region) and STI as labeled. The boundary is the Dirac semimetal state. (d) Phase diagram obtained by DFT calculations. Symbols are calculated points, shaded according to band inversion. Arrow indicates experimental thermal increase of lattice parameters and boundary corresponds to the topological phase transition. Circled point: room temperature lattice parameters [211].

K, and E_g *vs* temperature shown in Fig. 8.4(a), clearly indicating a gap closing and opening. The closing point occurs at or very near T_c, where μ crosses between bands. Results for Te_d and Te_a sites are quite similar as shown in the plot. The Te_z shift crossover prevented T_1 measurement in the immediate vicinity of T_c, although its behavior away from T_c is similar to that of the other sites. These results agree well with those of Xu *et al.* [88], although I find a larger high-T gap. Also note that the fit shows that μ is positioned in the Dirac bands, rather than in the gap both above and below T_c.

For $ZrTe_5$, it is well-known that its carrier type changes from *n* to *p* type when temperature increases [208], which is also strongly related with a Lifshitz transition [216]. However, $\mu(T)$ appears to have larger T-dependence than expected for such a case with a small carrier concentration change and fixed density of states. The reason behind it is unclear, and it is possibly due to a great temperature sensitivity in Van der Waals layered structure of $ZrTe_5$.

8.5.3 Topological phase transition

There have been several recent reports [74, 83, 84, 86, 89, 217] from Berry phase and surface imaging showing that the low-T phase is a weak, rather than strong, TI. Based on these results, I can infer that the Lifshitz transition observed here corresponds to a change from WTI to STI as temperature increases. This is the reverse of what was initially proposed [77, 78], and provides a clearer picture of the topological phase transition.

DFT calculations confirm that the inversion proceeds from WTI to STI as T increases. I initially scaled only *b*, and obtained DFT results equivalent to those of Ref. [77], with a gap closing at $b = 14.8$ Å, and reopening with reversed parity at Γ. It was shown [77] that this corresponds to a change from STI to WTI with increasing *b*. Similar results were obtained in Ref. [78]. However, I note that the experimental thermal expansion [211] for *b* and *c* are essentially equal and much smaller for *a*. Thus, I examined the case of *b* and *c* scaled equally with *a* held constant. The result, shown in Fig. 8.2(d), is that the gap closes at $b = 14.31$ Å, $c = 13.51$ Å, for smaller instead of larger *b*. Fig. 8.4(d) shows schematically an inferred phase boundary connecting the two inversion points identified this way. The parity of the band edges at Γ is reversed at both inversion points.

With the STI to WTI transition already demonstrated for the horizontal path in Fig. 8.4(d), the second inversion at Γ also requires a change of the strong Z_2 index and thus transition between STI and WTI [218].

Between 293 and 10 K, *b* changes from 14.53 to 14.47 Å [211], with a corresponding reduction of *c*. This range does not include the predicted crossing, however use of other exchange potentials may lead to adjustment of the predicted crossing point [75]. In addition strongly *n*-type CVT crystals are reported to have smaller lattice constants [208] making it appear likely that thermal expansion indeed drives the topological transition illustrated in Fig. 8.4(d). This explains why the topological transition appears at higher temperatures in *n*-type materials with reduced lattice parameters. It also suggests that *p*-type crystals, reported to be semiconducting at all temperatures [208, 216], are also STI down to zero temperature.

8.5.4 Two-band model

The difference between the Lifshitz transition temperature T_c and *n-p* transition temperature T_p can be well explained by a two-band model [208, 216] as shown in Fig. 8.4(b). While the Lifshitz transition occurs when μ passes through the Dirac point, carriers are also transferred to other minima, especially the one between Y and X, which is nearly degenerate with the Dirac point [Fig. 8.2(e)]. This is illustrated in Fig. 8.4(c) along with the measured resistance anomaly: (i) Below T_c, there is *n*-type metallic behavior with μ in the Dirac and secondary conduction bands. (ii) At T_c, μ is at the Dirac point, which transits to a gapless semimetal state. With μ also crossing the secondary band edge, the carriers remain *n*-type due to states at the parabolic minimum. (iii) μ moves away from the secondary conduction band edge, giving the *n-p* transition and the resistance anomaly. (iv) Increasing temperature produces metallic *p*-type behavior.

The carriers in the secondary minima will induce NMR Knight shifts (K) through their on-site spin interactions. However, based on the observed resistivity maximum, it can be estimated [208] that our crystals have $n \approx 1 \times 10^{18}$ cm^{-3}. For such carrier densities I estimate a contribution to K which is negligible compared to the observed T-dependent shifts; see for example computed Te shifts for Bi_2Te_3 in Ref. [219]. Thus, the observed T-dependence must be caused by Knight

shifts associated with Dirac electron spins, and/or on-site chemical shifts (δ) due to the induced paramagnetic response of the valence band.

For Dirac electrons, it was recently shown [213] that a significant dipole-generated K could be expected. The limiting contribution is proportional to μ away from the Dirac point, thus linear in T for the present case, with sign changing as the Dirac point is traversed. The dipole hyperfine field includes an angle-dependence which can lead to different magnitudes on each site, however, it seems likely that the nearly equivalent linear-T behavior for the Te_d and Te_a shifts is due to the Dirac electrons, with a smaller contribution for Te_z. Since these contributions vanish at T_c where μ goes through zero, the underlying chemical shifts can be identified from the shifts at this point.

8.5.5 DFT calculation on chemical shift

DFT calculations of δ are shown in Fig. 8.2(d), *vs* changes in *b* and *c*. The shifts for Te_d and Te_z are nearly identical, while for Te_a the result is about 500 ppm more negative. This agrees with the observed shifts at T_c, except for an overall negative shift. Although exchange potentials such as mBJ are expected to better reproduce the experimental shifts as opposed to PBE [212], the relative positions are thus rather close to what is observed. The calculated change in δ *vs* lattice expansion is relatively small, indicating that Dirac electrons are the dominant source for the observed linear T dependence. However, the step-like change in Te_z shift at the inversion point is reproduced in the calculation of δ, which helps to confirm the site identification of NMR lines.

With δ associated with a local Van Vleck-type susceptibility due to partially filled Te *p* states [172], the step-like change in δ also indicates a rearrangement of filled orbitals at T_c. The proposed band inversion was originally explained [75] in terms of a change in stabilization of *p* orbitals on Te_z and Te_d sites. An associated change in orbital occupation thus will modify δ, and this demonstrates that the NMR shifts in this case provide a direct measurement of the topological inversion, and thus further confirmation of the orbital interchange involved in the $ZrTe_5$ transformation. There are few techniques providing a local measurement of atomic symmetry; thus this can be a significant capability for probing quantum materials.

8.6 Summary

In this chapter, NMR techniques combined with DFT calculations are used to explore the electronic structure and topological nature of $ZrTe_5$. Results show a temperature dependence of the band gap of $ZrTe_5$. The Dirac band gap closes and reopens at a Lifshitz transition (about 85 K) with temperature increasing, which corresponds to a topological phase transition from weak to strong topological insulator. Besides reporting the results of $ZrTe_5$, it also shows that the NMR technique such as spin-lattice relaxation results can provide a very sensitive measure of the Dirac electrons involved in this transition. DFT calculations give further details about this band inversion, providing a better understanding of the topological phase transition. The observed shift change of Te_z site at T_c give direct evidence of the band inversion of symmetry occurring at the topological phase transition point.

9. TOPOLOGICAL CHALCOGENIDE $ZrTe_2$*

9.1 Introduction

In this chapter, I have studied $ZrTe_2$ using NMR techniques combined with DFT computations, revealing its topological nature and electronic properties as a quasi-2D topological dichalcogenide. The material was prepared and measured by myself in our lab at TAMU. The DFT calculations were done by my labmate Dr. Nader Ghassemi. The measured shifts and spin-lattice relaxation rates for both $B \parallel c$ and $B \perp c$ orientations have been measured, which show that the layered dichalcogenide $ZrTe_2$ presents Dirac quasi-2D features associated with a nodal line extending in the direction perpendicular to the layers.

9.2 Sample Preparation

The $ZrTe_2$ single crystals (crystal structure shown in Fig. 9.1) were prepared using chemical vapor transport. The stoichiometric mixture of Zr and Te powder was sealed in a quartz tube with iodine being used as transport agent (2 mg/cm^3). Plate-like single crystals with metallic luster were obtained via vapor transport growth with a temperature gradient from 950 °C to 850 °C. Cameca SXFive microprobe measurements indicate a uniform phase $Zr_{0.99}Te_2$.

9.3 Experimental and Computational Methods

NMR experiments utilized a custom-built spectrometer at a fixed field $B \approx 9$ T. Many individual crystals were stacked with the c axes aligned and the sample was measured with the field parallel to c ($B \parallel c$) and in the basal plane ($B \perp c$). The a axis orientation was not identified for these crystals. ^{125}Te (nuclear spin $I = 1/2$ and gyromagnetic ratio $\gamma = -8.51 \times 10^7$ rad s^{-1} T^{-1}) shifts were calibrated by aqueous $Te(OH)_6$ and adjusted for its $\delta = 707$ ppm paramagnetic shift to the dimethyltelluride standard [210].

The band structure and density of states calculations were carried out in the framework of the

*Part of this chapter is reprinted from Ref. [220] (Y. Tian, N. Ghassemi, and J. H. Ross, Jr., "Topological nodal line in $ZrTe_2$ demonstrated by nuclear magnetic resonance," Phys. Rev. B, vol. 102, p. 165149, Oct 2020.) with permission from APS.

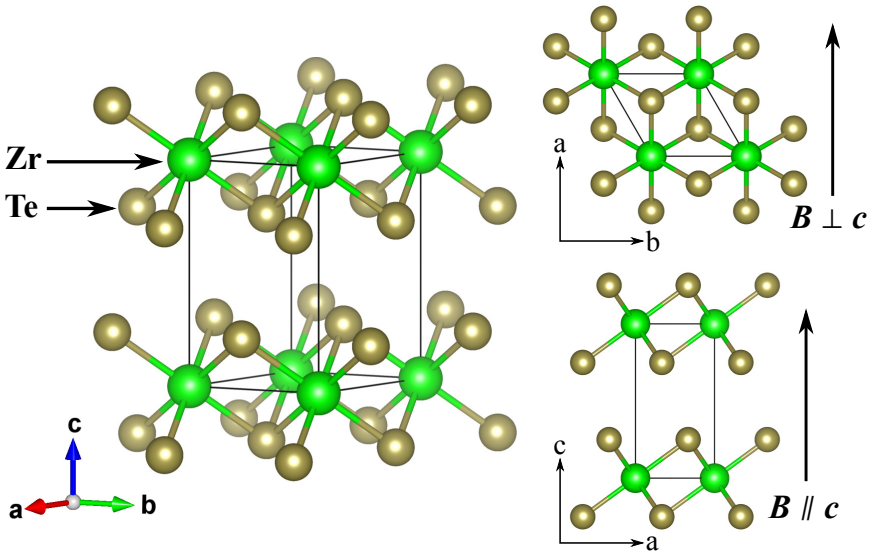

Figure 9.1: Crystal structure of 1T-$ZrTe_2$ with P-3m1 space group, showing van der Waals-bonded layered structure.

density functional theory (DFT) by employing the APW plus local orbital (APW+lo) method [221] with the PBE potential [165] as implemented in the WIEN2K code [113]. A mesh of 1000 k-points was employed in the irreducible wedge of the hexagonal Brillouin zone [see Fig. 9.4(d)] corresponding to the grids of $10 \times 10 \times 10$ in the Monkhorst-Pack [222] scheme. The cutoff parameter of $k_{\max} = 7/R_{\mathrm{MT}}$ inside the interstitial region was used for the expansions of the wave functions in terms of the plane waves.

9.4 Experimental and Computational Results

9.4.1 Shift

Consistent with the single local environment for Te in the 1T-$ZrTe_2$ structure, there is only one peak observed in the ^{125}Te spectra as shown in Fig. 9.2(a). The angular dependence of the NMR shift (with θ defined between the ab layer and the magnetic field B) is shown in Fig. 9.2(b). The room-temperature shift was fitted [red curve in Fig. 9.2(b)] to

$$K = K_{\mathrm{iso}} + \frac{3\cos^2\theta - 1}{2} \cdot \Delta K, \tag{9.1}$$

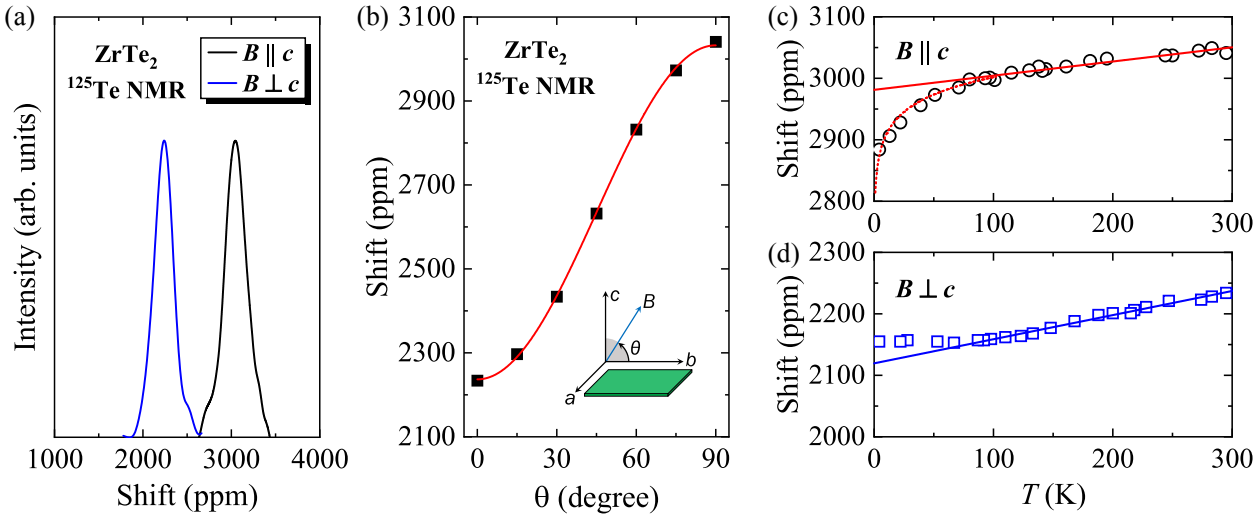

Figure 9.2: (a) ^{125}Te lineshapes of $ZrTe_2$ at room temperature. (b) Angular dependence of shift at room temperature. The red solid curve is a fit to Eq. (9.1). Shift *vs* temperature for (c) $B \parallel c$ (magnetic field perpendicular to the layers) with linear and $\ln(T)$ curves as guides to the eye and (d) $B \perp c$ (magnetic field parallel to the layers).

where $K_{\rm iso} = 2767 \pm 3$ ppm is the isotropic shift and $\Delta K = -530 \pm 4$ ppm. By symmetry, the shift will not depend on orientation in the basal plane, which is confirmed by the absence of additional inhomogeneous line broadening for this orientation [Fig. 9.2(a)]. Ref. [223] gives $\delta_{\rm iso} = 1825$ ppm with $Te(OH)_6$ as reference, which corresponds to 2532 ppm, a similar shift as reported here, considering the large width measured in Ref. [223].

Figs. 9.2(c) and 9.2(d) show the temperature dependence of the ^{125}Te shift for $B \parallel c$ and $B \perp c$ ($K_{\parallel c}$ and $K_{\perp c}$), respectively. The shifts were obtained by identifying the highest intensity position of the measured single-peak ^{125}Te spectra. Both $K_{\parallel c}$ and $K_{\perp c}$ decrease monotonically *vs* T, with $K_{\rm iso}$ corresponding to the linear fits [shown in Figs. 9.2(c) and 9.2(d)] changing by 0.34 ppm/K. At low T, $K_{\parallel c}$ shows a sharp decrease as T approaches zero, while for $K_{\perp c}$, there is a clear change in the opposite direction close to 50 K, where the shift is nearly temperature independent. These results are indicative of quasi-2D Dirac-node behavior as is discussed in Sec. 9.5.1.

The carrier concentration shown in Ref. [93] is in the order of 10^{19} cm^{-3}, which presents the fact that the large measured shifts are mostly chemical shifts due to electronic states away from the Fermi energy (ε_F); however, the temperature-dependence is dominated by Knight shifts due to

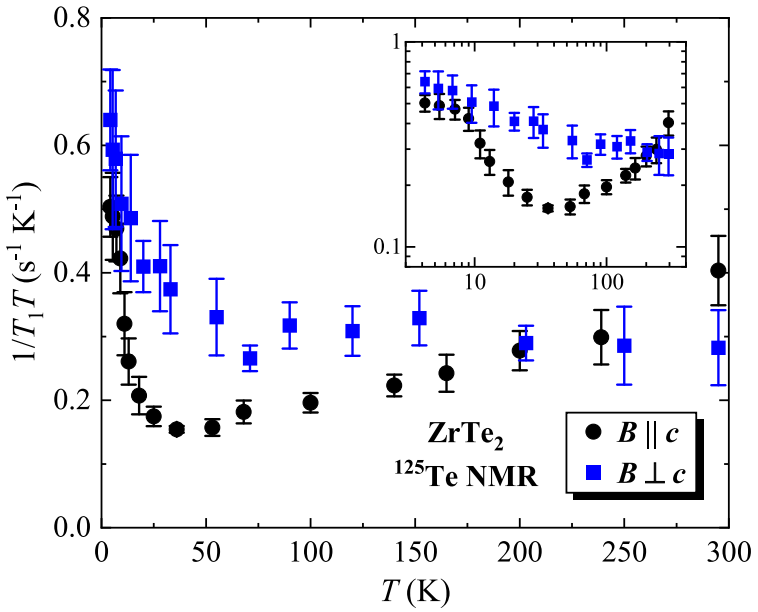

Figure 9.3: $1/T_1T$ *vs* T for both orientations $B \parallel c$ (perpendicular to the layers) and $B \perp c$ (parallel to the layers). Inset: $1/T_1T$ *vs* T in log scale.

carriers at ε_F, and for convenience I label observed shift, which is the sum of these shift terms, as K.

9.4.2 Spin-lattice relaxation

Spin-lattice relaxation results, measured by inversion recovery, could be well fitted to a single exponential $M(t) = (1 - Ce^{-t/T_1})M(\infty)$, giving $1/T_1T$ values shown in Figs. 9.3(a) and 9.3(b). The results decrease rapidly at low temperatures as T increases, especially $(1/T_1T)_{\parallel c}$, which changes rather quickly at temperatures near 15 K. Near 50 K, which is also the temperature at which $K_{\perp c}$ exhibits a change in behavior, the relaxation results also exhibit a characteristic change, with $1/T_1T$ leveling off, and $1/T_1T$ exhibiting a minimum near 40 K and then steadily increasing. In metals, $1/T_1T$ is often dominated by s-electron Fermi contact and proportional to $g^2(\varepsilon_F)$. However, similarly to $ZrTe_5$ [75] I find that the Dirac states in $ZrTe_2$ are dominated by Te p-orbitals, along with Zr d-states, as confirmed by the DFT results which are described in the next section. These produce a dominant orbital contribution to the $1/T_1T$, and I will further demonstrate that the largest term is due to the high-mobility Dirac carriers.

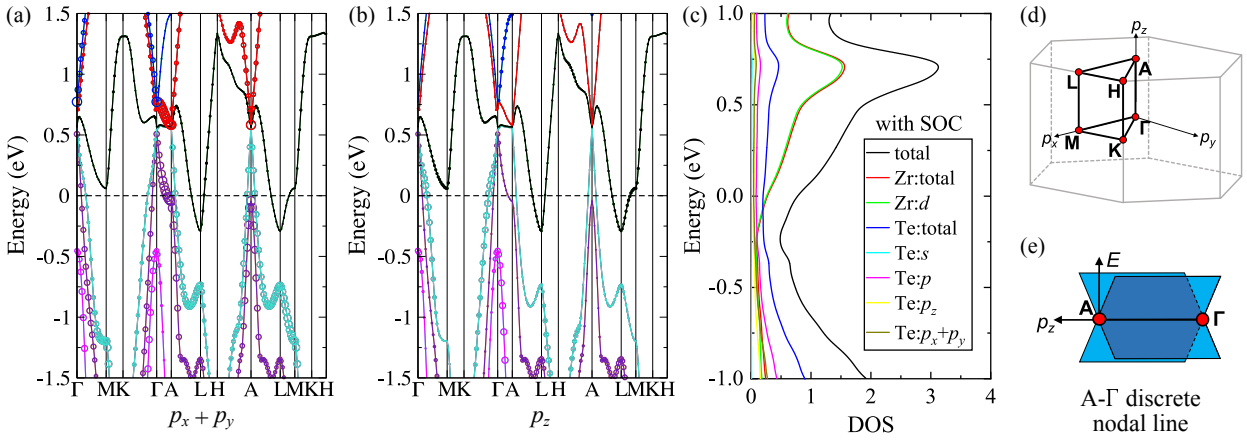

Figure 9.4: Band structures of $ZrTe_2$ with spin-orbit coupling, with superposed circles showing weights for (a) $p_x + p_y$ and (b) p_z Te orbitals. The dashed lines represent the Fermi level. The circle size represents the partial state density of Te. (c) Density of states for $ZrTe_2$. (d) 3D view of the hexagonal Brillouin zone with high-symmetry points. (e) Sketch of discrete nodal line between Γ and A.

9.4.3 DFT computations

From reports by several groups [91–93,99–101], there have been some conflicts about the topological nature of $ZrTe_2$ as detected in DFT results. Ref. [101] suggests a semimetallic state of $ZrTe_2$ without any topological nature. Ref. [93] suggests $ZrTe_2$ is a topological semimetal, consistent with its ARPES results. Both Refs. [92, 93] indicate a Dirac point at Γ with the Dirac node close to the chemical potential and an electron pocket at M in the conduction band. The lattice parameters used in Ref. [93] are about 1-2% expanded from experimental values. However, these parameters were obtained from a DFT energy optimization, and they provided an approximate match for the reported ARPES results, with the calculated Dirac node roughly 0.5 eV higher in energy than what is actually observed by ARPES, and with larger calculated overlaps of the pockets at L and M than what is observed. Ref. [101] included a correction for the van der Waals interaction, leading to a much smaller overlap at the L and M points; however, a large gap opened throughout the Brillouin zone, in seeming contradiction with magnetotransport results [224] as well as APRES results [93]. It is likely that the well-known difficulty in predicting band energies near the gap in standard GGA functionals such as PBE is responsible for the discrepancies between the calculated results and the

observation. In TMDCs specifically DFT is well-known to underestimate the band gaps [225,226]. For further investigation I used the lattice parameters of Ref. [93] ($a = 3.909$ Å and $c = 6.749$ Å) for DFT calculations, with the understanding that the ε_F position is much closer to the Dirac node than predicted.

Results of the DFT calculations, with spin-orbit coupling included, are shown in Figs. 9.4(a)-(c). The nearly-dispersionless band from Γ to A connects to Dirac-like features at Γ (as previously identified [92, 93]) and also at A, and this band is doubly degenerate except for a gap of about 20 meV very close to Γ, identified [93] as associated with a band inversion. The mapping in reciprocal space, and a schematic of the nodal line between Γ and A, are demonstrated in Figs. 9.4(d) and 9.4(e). Note that this differs from the "nodal loop" pictured in Fig. 1.3; the closed-loop Dirac node is sometimes also called a nodal line. Here the nodal line is straight and extends across the Brillouin zone. Also note that the partial DOS results show that Te p-orbitals mostly locate at these Dirac bands away from the node while Zr d-orbitals dominate at the node itself, and the Zr orbitals dominate the electron pockets at L and M. There is also a separate high-dispersion band crossing Γ just below the node energy.

As an estimate of the Fermi velocity for the Dirac nodal line, I analyzed the linear slope in the Γ-M and A-L directions leading up to the nodal line according to $\varepsilon = \hbar v_F k$, and obtained 6.9 and 6.5×10^5 m/s. Based on these values, which are typical for Dirac semimetals [72], I will use the mean value, 6.7×10^5 m/s, for further analysis of the Dirac-carrier behavior. A similar value was estimated for the monolayer case [92]. The extra pockets at L and M contain ordinary electrons, and the existence of both Dirac and ordinary electrons at ε_F leads to additional complexity in this case, although experimental indications [92, 93] point to a much smaller overlap between the M pocket and the Dirac valence band than what is calculated. With the $\sqrt{\varepsilon}$ type density of states near ε_F dominated by the M pocket I fitted to $g(\varepsilon) = \sqrt{(2\varepsilon(m^*)^3)}/(\pi^2\hbar^3)$ and obtained an estimate of $m^* = 1.7\, m_e$ for this pocket. In the model discussed in Sec. 9.5.1, the position of Fermi level is near the edge of this pocket, and very close to the nodal line.

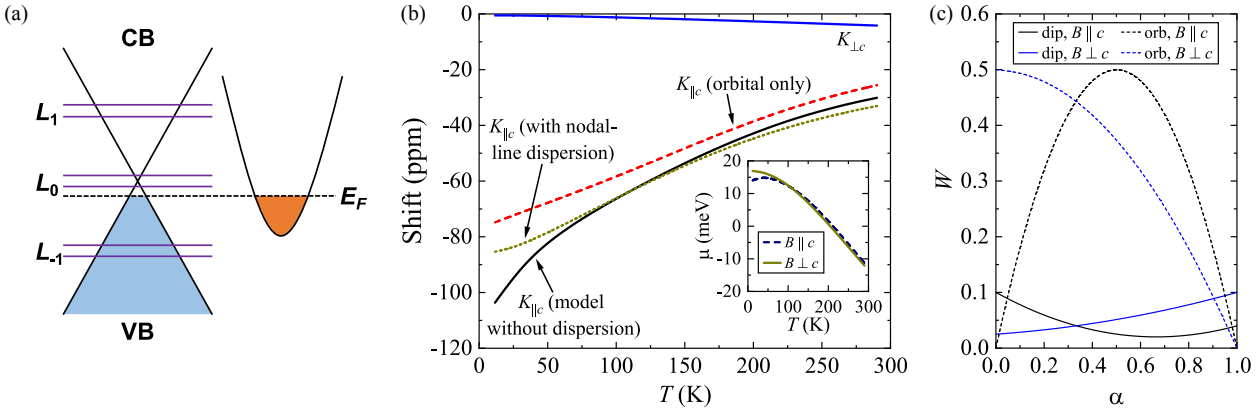

Figure 9.5: (a) Sketch of Dirac band and electron pocket. (b) Simulated shifts for both orientations. Inset: chemical potential *vs* T. (c) $W = 1/2T_1$ is the dipolar and orbital relaxation rates divided by $2\pi(\gamma_e\gamma_n\hbar^{3/2})^2 g^2(\varepsilon_F)k_BT\langle r^{-3}\rangle^2$. α is the mixture of orbitals $(p_x + p_y)$ *vs* p_z.

9.5 Discussion and Analysis

9.5.1 Knight shift

As shown in Figs. 9.2(c) and 9.2(d), there is an obvious difference between the measured shifts of $B \parallel c$ and $B \perp c$ orientations, especially at low temperatures. The observed low-T divergence for $K_{\parallel c}$ follows approximately a $\ln(T)$ curve, characteristic of the divergent orbital susceptibility for Dirac semimetals [102,214], although the absence of the corresponding behavior for $K_{\perp c}$ points to a quasi-2D Dirac semimetal rather than 3D point-node behavior.

To analyze this situation, first I note that the shifts will be largely due to the dominant p-electrons for Te in $ZrTe_2$, contributing a combination of core polarization and spin-dipolar shifts, which are due to electron spin mechanisms, as well as orbital shifts, with the latter likely dominated by the large bulk orbital response of the Dirac electrons rather than due to local orbitals. The core polarization mechanism normally contributes an isotropic shift (the same sign for both orientations) and the spin-dipolar, anisotropic shift [second term in Eq. (9.1)]. However, the absence of divergent behavior for $B \perp c$ points to a different physical mechanism for the two orientations rather than shift anisotropy, and thus, I analyze the $B \parallel c$ divergence in terms of the spin response of quasi-2D Dirac electrons due to the separation of Landau levels with $B \parallel c$, plus an orbital shift dominated

by quasi-2D orbital currents confined to the basal plane.

For quantitative comparison, first I consider the case of a 3D point node. The Knight shift due to the orbital interaction in a 3D massless Dirac electron case can be expressed as [214],

$$K = K_0 - \left[\frac{\mu_0 v_F e^2}{6\pi^2\hbar} \ln\left(\frac{W}{\max\{k_B T, |\mu|\}}\right)\right](1 - N_D), \tag{9.2}$$

where K_0 is a T-independent term, μ is the chemical potential measured from the Dirac node, W is a bandwidth cutoff and N_D is demagnetizing factor. N_D can be significant for the orbital hyperfine contribution of extended Dirac carriers, and in fact in the pure 2D limit the shift due to this mechanism will vanish [227]. Note this is the low field case. For v_F, I used $v_F = 6.7 \times 10^5$ m/s from the DFT results (Sec. 9.4.3). Considering the demagnetizing effect, the overall sample size (around $2 \times 2 \times 0.5$ mm^3) implies a demagnetizing factor of approximately $N_D = 0.8$ for such a bulk-susceptibility contribution for the $B \parallel c$ orientation. Using these values, and assuming that $k_B T$ dominates in the logarithm of Eq. (9.2), I obtain a difference in shift of less than 1 ppm between the temperatures 10 K and 100 K, much less than what is observed. Or, if changes in μ are on the order of $k_B T$, the results will be similarly small.

9.5.2 Quasi-2D model for Knight shift

As alternative I consider the shift due to the diamagnetic currents of a Dirac nodal line oriented along the c direction. In this quasi-2D case, currents are confined to the basal plane, and the diamagnetic response is equivalent to that of a 2D Dirac gas, for which I follow the treatment used for graphene [228]. Also note that the effect vanishes for $B \perp c$, due to the absence of high mobility circulating currents perpendicular to the plane. For $ZrTe_2$ I modeled this system as including a quasi-2D Dirac line, with the addition of a normal electron pocket crossing the node energy ($\varepsilon_{\mathrm{node}}$), as indicated by DFT calculations and by ARPES measurements [93].

First, I calculate the chemical potential (μ). For the normal electron pocket I assumed an effective mass $m^*/m_e = 1$, close to the estimate for the pocket at M in DFT calculations (Sec. 9.4.3). Also for the perpendicular Fermi velocity I used the result obtained from DFT, $v_\perp = 6.7 \times 10^5$

m/s, which in the 9 T NMR field perpendicular to the layers gives Landau-level energies $\varepsilon_{\rm LL}(N) = \pm\sqrt{(2e\hbar v_\perp^2 B|N|)} = \pm 73\sqrt{(|N|)}$ meV, and a volume density of carriers per spin level $n_{\rm LL} = B/(\Phi_0 c) = 3.3 \times 10^{18}$ cm^{-3}, where $\Phi_0 = 4.14 \times 10^{-15}$ T m^2 is the magnetic flux quantum. The gyromagnetic ratio is not known for these carriers, so I assumed $g = 2$. Also I assumed that a fixed density of carriers $n_{\rm total} = 10^{19}$ cm^{-3} estimated from ARPES results [93] is divided between these band features. To solve for the chemical potential I specified,

$$n_{\rm total} = \int_0^\infty f(\varepsilon,\mu) g_{\rm CB}(\varepsilon) d\varepsilon + \sum_{s=-1/2}^{1/2} \sum_{N=-\infty}^{\infty} n_{\rm LL} f(\varepsilon_N,\mu) - n_{\rm LL} - \sum_{s=-1/2}^{1/2} \sum_{N=-\infty}^{-1} n_{\rm LL}, \qquad (9.3)$$

where $g_{\rm CB}(\varepsilon) = \sqrt{(2\varepsilon m^{*3})}/(\pi^2\hbar^3)$ is the density of states in the normal-carrier pocket with its minimum set to $\varepsilon = 0$, $\varepsilon_N = \varepsilon_{\rm node} + \mu_B g B s + \varepsilon_{\rm LL}(N)$ represents the Landau level energies, and $f(\varepsilon,\mu) = 1/[1 + e^{(\varepsilon-\mu)/k_B T}]$ is the Fermi function. The extra term $n_{\rm LL}$ comes about because the lower $N = 0$ level is derived from the hole states, and I apply level quantization only to the Dirac states for which the large v_F pushes these states into the quantum limit. In the finite sums, I chose a very large cutoff for which the sums are numerically well-converged. In the $B \perp c$ case for which the Landau levels collapse, I replaced the sum over Landau levels in Eq. (9.3) with an integral over the 2D Dirac density of states $g_D(\varepsilon) = |\varepsilon - \varepsilon_{\rm node} \pm \mu_B g B s|/[\pi c(\hbar v_\perp)^2]$ per spin, also normalized for hole states similarly to the last term in Eq. (9.3). Solving for $\mu(T)$, I obtained the results shown in the inset of Fig. 9.5(b), for the case $\varepsilon_{\rm node} = 12$ meV. Because of the significant carrier density $n_{\rm LL}$ at each Landau level energy including $N = 0$, the $B \parallel c$ field tends to pull μ into $\varepsilon_{\rm node}$ at low temperature [229], as can be seen from the results shown in the inset of Fig. 9.5(b). Recently anomalous magnetotransport effects were also identified in a layered Dirac material due to field-induced alignment of the chemical potential [230].

I next calculate the diamagnetic susceptibility, $\chi = \mu_0 \partial M/\partial B$, and its contribution to the NMR shift, $K = \chi(1 - N_D)$. The magnetization for $B \parallel c$ is $M = -(1/V)\partial\Omega/\partial B$ [228] with the

grand potential volume density given by

$$\Omega/V = -k_B T n_{\rm LL} \sum_{N=-m}^{m} \ln[1 + e^{(\varepsilon_N - \mu)/k_B T}], \tag{9.4}$$

with m a numerical cutoff for the sum. For numerical calculation of the B derivative, I adopted the method described in Ref. [228] to normalize for the B-dependence caused by the numerical cutoff m. Using the $\mu(T)$ results shown in the inset of Fig. 9.5(b), I thus arrived at an estimation of χ for the $B \parallel c$ case. For the $B \perp c$ case, the diamagnetic contribution is zero since there is no splitting into Landau levels. Using the demagnetizing factor $N_D = 0.8$ estimated for our sample for $B \parallel c$, I arrived at the bulk-diamagnetic contribution to $K_{\parallel c}$ shown by the dashed curve in the main plot of Fig. 9.5(b). Note that in the B-derivative of Ω/V I included changes in $n_{\rm LL}$ and $\varepsilon_{\rm LL}(N)$, but not in the numerical solutions $\mu(T)$. The difference should be small, since for most of the temperature range the CB pocket determines the position of μ, while at low temperatures the results have the linear-T behavior equivalent to the case that μ is fixed at $\varepsilon_{\rm node}$ [228], due to the pulling effect of the magnetic field.

To calculate the spin contribution to the shift, I first calculated the Dirac-electron spin density as

$$n_{\rm spin} = \sum_{s=-1/2}^{1/2} 2s \sum_{N=-\infty}^{\infty} n_{\rm LL} f(\varepsilon_N, \mu), \tag{9.5}$$

both for $B \parallel c$ and $B \perp c$ using the corresponding $\mu(T)$ values shown in the inset of Fig. 9.5(b). Assuming the core-polarization hyperfine contribution dominates for the Te p-electrons participating in the Dirac node, I used the estimated [137] hyperfine field $B_{\rm cp}^{\rm HF} = -15$ T in calculating the spin shift as $K_{\rm spin} = n_{\rm spin}(B_{\rm cp}^{\rm HF}/9\ {\rm T})(V_{\rm cell}/2)$, with 9 T the applied NMR field and the sample volume per Te atom given by $V_{\rm cell}/2 = 50$ Å^3. The results were added to the calculated T-dependent diamagnetic orbital shift, giving the spin+orbital result plotted in Fig. 9.5(b) (lowest curve). The results are comparable to the observed shift behavior and have the same general temperature dependence. Since there is considerable likelihood that g differs from 2 [231–234], I did not attempt a quantitative fitting; however, it appears that this model correctly captures the low-T behavior,

and that a combination of spin susceptibility and orbital diamagnetism, both strongly enhanced in the quantum limit for the $B \parallel c$ orientation, are responsible for the observations.

Comparing to the 3D case discussed earlier [Eq. (9.2)], I can thus understand the enhanced effect for the quasi-2D case as due to two effects. First, the lack of Landau level dispersion in 2D means that the density of states is changed considerably by the field, which allows for a large spin polarization since a large number of states is concentrated at discrete energies. Secondly, this concentration of states in energy also enhances the diamagnetic response obtained from Eq. (9.4). Also note that the estimated $\mu(T)$ obtained from Eq. (9.3) [Inset of Fig. 9.5(b)], should be little changed in the 3D case because of the large role of $g_{\mathrm{CB}}(E)$, and indeed these changes in $\mu(T)$ are on order of $k_B T$, confirming the estimate in Sec. 9.5.1 of the small expected shift in that case.

Note that in the DFT results (Fig. 9.4), a small dispersion appears in the nodal line, with the changes covering a range of approximately 20 meV between Γ and A. To model the effect of this behavior, I added a simple linear dispersion to the $\varepsilon_{\mathrm{node}}$ position. This was done by modifying the sum over Landau level numbers N in Eqs. (9.3)-(9.5), replacing the summands having fixed $\varepsilon_{\mathrm{node}}$ by an integrated square distribution covering a range $\varepsilon_{\mathrm{node}} \pm 10$ meV, and repeating the numerical calculations described above with otherwise identical parameters. This yielded the spin+orbital shift result shown in the dotted curve in Fig. 9.5(b): the main effect is a softening of the spin contribution as T approaches zero; however, the calculated magnitude is similar to that of the completely dispersionless case.

9.5.3 Relaxation mechanisms

The low-T $1/T_1$ results exhibit an anisotropy and temperature dependence which does not match the corresponding behavior of the measured shifts. Thus, I expect the T_1 behavior is not a result of a Korringa-type spin contribution [172] which would be expected in that case. However, in contrast to the spin contribution, the orbital shift and T_1 are not governed by a Korringa relation [102], and the behavior in the low-T limit matches what is predicted [214, 235] for the quasi-2D orbital case due to a mechanism governed by high-mobility carriers which I denote here as the extended orbital mechanism, since carriers far from the nucleus dominate this process. For the

quasi-2D free-electron gas (i.e., metallic layers where the electrons behave as a 2D free-electron gas), Lee and Nagaosa obtained the relaxation rates due to this mechanism when the magnetic field is applied parallel and perpendicular to the layers [235], which corresponds to a ratio between $(1/T_1T)_{\|c}$ and $(1/T_1T)_{\perp c}$ of 2:3. As shown in Fig. 9.3, excluding a T-independent background, the low-T $(1/T_1T)_{\|c}$ and $(1/T_1T)_{\perp c}$ reaches a ratio close to 2:3. Thus, the low-T behavior can be modeled using the extended orbital scenario.

For a quasi-2D Dirac system, the extended orbital contribution can be expressed as [214]

$$\left(\frac{1}{T_1T}\right)_{\perp c} = \frac{3}{2}\left(\frac{1}{T_1T}\right)_{\|c} = \frac{\mu_0^2\gamma_n^2e^2k_B}{(4\pi)^2}\int_{|E|>\Delta} dE\left[-\frac{\partial f(\varepsilon)}{\partial\varepsilon}\right]\frac{\sqrt{\varepsilon^2-\Delta^2}}{\hbar^2cv_F}\ln\frac{2(\varepsilon^2-\Delta^2)}{\hbar\omega_0|\varepsilon|}, \quad (9.6)$$

with $\varepsilon = \pm\sqrt{{v_F}^2k^2+\Delta^2}$ and c the distance between nearest neighbor layers. In addition, $f(\varepsilon)$ is the Fermi function and $E_g = 2\Delta$ is the gap. In the low-T limit assuming Δ is small, this readily evaluates to $\frac{(\mu_0\gamma_ne)^2}{(4\pi)^2}\frac{k_B\mu}{\hbar^2cv_F}\ln(\frac{2\mu}{\hbar\omega_0})$. Comparing to the result [214] for a 3D point node in the same limits, $\frac{8\pi}{3}\frac{(\mu_0\gamma_ne)^2}{(4\pi)^2}\frac{k_B\mu^2}{\hbar^3v_F^2}\ln(\frac{2\mu}{\hbar\omega_0})$, $1/T_1T$ for the quasi-2D case is the same as the 3D case multiplied by a factor $\frac{3}{8\pi}\frac{\hbar v_F}{\mu c}$. Taking $\mu = 10$ meV, $v_F = 0.67\times10^6$ m/s, and $c = 6.7$ Å for $ZrTe_2$, this is a factor of 7, with the quasi-2D situation enhanced essentially because of the increased phase space for the scattering phenomena leading to Eq. (9.6), which can include events with Δk covering the entire Brillouin zone in the direction perpendicular to the layers. With the low-T $(1/T_1T)_{\perp c}$ larger by a factor of about 10 as compared to that of the comparable point-node material $ZrTe_5$ [96], this indeed makes it plausible that the extended-orbital mechanism for high-mobility Dirac electrons is the dominant mechanism at low temperatures. In the low-T limit, the ratio $(1/T_1T)_{\perp c}/(1/T_1T)_{\|c}$ is smaller than the expected 3/2 given by this model; however, note that Eq. (9.6) was derived in the low-field limit, and it seems possible that such effects might renormalize the $(1/T_1T)_{\|c}$ results. In addition, while the normal-electron pocket at M is strongly dominated by Zr *d*-orbitals, a nonzero contribution due to Te states might also lead to a slowly varying background contribution to $1/T_1T$.

As shown in Fig. 9.5(b), I determined that Dirac spins can give a considerable contribution to Knight shift due to core polarization combined with Landau level splitting for $B \parallel c$. However,

I expect the core polarization mechanism to give a rather negligible contribution to $1/T_1T$. This can be seen from the Korringa relation [137] which can provide an approximate upper limit for the spin $1/T_1T$. For ^{125}Te, the Korringa relation will be, $(1/T_1T)_{\rm spin} = K^2_{\rm spin}/[2.6 \times 10^{-6}\ ({\rm s\,K})^{-1}]$, and with $|K_{\rm spin}|$ at low temperatures determined to be somewhat less than 100 ppm, choosing 100 ppm yields a limiting value $(1/T_1T)_{\rm spin} = 4 \times 10^{-3}\ ({\rm s\,K})^{-1}$. This is considerably smaller than what is observed. Note also that in the low-T limit where the Dirac spins are heavily polarized, the probability of spin-flip scattering can be reduced, further limiting $1/T_1T$. However, the extended orbital $1/T_1T$ due to high-mobility electrons is not connected to the shift via a Korringa relation, and from these considerations I determine that the spin-lattice relaxation rate of $ZrTe_2$ is dominated by this orbital contribution. These results will extend across the whole temperature range.

As the temperature increases past 10 K, $(1/T_1T)_{\|c}$ drops rather suddenly, reaching a minimum at about 40 K. This also coincides with a reported drop in the Dirac-carrier mobility, before the high-T regime sets in with different behavior [224]. I believe that the change in $(1/T_1T)_{\|c}$ can be understood in terms of carrier scattering effectively reducing the dimensionality of the relaxation mechanism. Ref. [156] shows that the orbital $1/T_1T$ process due to high-mobility electrons, which relies upon a logarithmic divergence in the hyperfine coupling mechanism at large distances, will begin to cut off at a distance corresponding to the mean free path (ℓ) as the scattering rate increases, so that $1/T_1T$ becomes proportional to $\ln(\ell)$. With little or no dispersion for the nodal-line carriers in the direction perpendicular to the layers, the mean free path will certainly be highly anisotropic. Once this length becomes considerably reduced, $1/T_1T$ will go over to the 2D case, for which the extended orbital $(1/T_1T)_{\perp c}$ is unchanged but $(1/T_1T)_{\|c}$ in this mechanism vanishes [214, 227]. This is not to say that the layers become completely decoupled; a large reduction in mean free path is sufficient for this change to occur.

Above the minimum, $(1/T_1T)_{\|c}$ again starts to increase. As seen in the inset of Fig. 9.5(b), the increase *vs* T is also accompanied by a drop in chemical potential to maintain charge balance given the large $g_{\rm CB}(\varepsilon)$ contribution. As shown in Figs. 9.4(a) and (b), there is a split-off band at Γ just below the Dirac node, which is more strongly dominated by Te p-electrons. As μ decreases,

holes will begin to appear in these states, with a significant effect on the ^{125}Te NMR because of their orbital weight. Aside from the $1/T_1T$ changes, there is also a change of character for the T-dependence of K, with a small increase in shift appearing for $B \perp c$. This behavior matches the observed change in magnetotransport behavior at these temperatures [224], which I believe is a Lifshitz transition corresponding to the chemical potential meeting this split-off band edge. To understand the increase in $(1/T_1T)_{\|c}$ at high temperatures, I show in the Appendix that in addition to the extended orbital contribution, there is local orbital contribution [156] to $1/T_1T$, which does not rely on logarithmic divergence at extended distances which will be larger for the $B \parallel c$ orientation as long as the Te p_z contribution exceeds the Te p_x and p_y contributions [Fig. 9.5(c)], which seems to be the case here. Therefore, the high-temperature behavior can be understood in terms of an enhanced local-orbital contribution of $1/T_1T$, dominated by the split-off band which comes into play at higher temperatures, while the extended orbital contribution decreases as a consequence of the large decrease in carrier mobility.

9.6 Summary

In this chapter, mainly NMR techniques were used to investigate the electronic and topological properties of $ZrTe_2$. The topological nature of transition metal dichalcogenide $ZrTe_2$ is revealed here as a quasi-2D Dirac semimetal with a nodal line between Γ and A. For magnetic fields perpendicular to the $ZrTe_2$ layers, the measured shift can be well-modeled by a combination of orbital shift and spin shift due to high mobility Dirac carriers. I also show that the low-temperature behavior of the spin-lattice relaxation rate can be explained through a quasi-2D Dirac electron model. In the intermediate temperature range, an increase in scattering of the Dirac carriers is applied to interpret the observed fast drop of the spin-lattice relaxation rate for the $B \parallel c$ orientation. With temperature further increasing, the local orbital contribution starts to dominate the spin-lattice relaxation rate with the significant contribution of a split-off band.

10. SUMMARY AND CONCLUSIONS

This dissertation describes studies of several materials which are of considerable current interest. For this work, NMR studies have been used as the primary experimental tool, combined with a number of additional experimental and computational techniques, as a highly sensitive way to investigate the electronic behavior of these systems, providing for example a better understanding of the band crossing behavior in topological chalcogenides, and the response of charge carriers near the band edge in advanced thermoelectric materials. These studies may be used to design improved materials for important practical applications such as enhanced thermoelectric cooling or new quantum electronic devices.

The first studied family of thermoelectric materials is half-Heusler. I have applied various techniques, mainly NMR spectroscopy including ^{93}Nb, ^{59}Co and ^{121}Sb measurements, with the support of magnetic, specific heat, Mössbauer measurements and DFT calculations. For pure NbFeSb sample, the NMR shift and T_1 results are consistent with heavily doped *p*-type behavior at low temperatures. Below 200 K, NbFeSb shows a Korringa-type NMR response, and a Kondo-related behavior below 80 K due to the interaction of carriers and local moments. Above 280 K, the enhanced Knight shift and T_1^{-1} indicate increased carrier density across a very small gap of about 0.03 eV, which is associated with an empty impurity band due to acceptor states located a small distance above the valence band maximum, with native *p*-type doping giving the low-temperature metallic behavior.

For NbFeSb-based Ti-substituted $Nb_{1-x}Ti_xFeSb$ samples, the measured spin-lattice relaxation results are well-modeled in terms of an orbital contribution in good agreement with DFT calculations for NbFeSb. With increasing *x*, a deviation from the expected behavior was observed, which is due to resonant valence band levels without contributing to transport results. NMR shift *vs* *x* are also well-explained by a model combining carrier-concentration-dependent Knight shift and composition-dependent chemical shift. The T-dependence of the satellite peak in the unsubstituted NbFeSb Mössbauer spectrum provides a direct measure of charging of acceptor states in an im-

purity band located around 30 meV above valence band edge, which is consistent with previously measured NMR results.

Besides NbFeSb series, I have also investigated other unsubstituted half-Heusler samples (ZrCoSb, NbCoSn, and TaFeSb) using NMR as a local probe combined with DFT calculations. For ZrCoSb, both ^{59}Co and ^{121}Sb shift and spin-lattice relaxation measurements show consistent results indicating the excitation of carriers and the existence of impurity band right below the conduction band. For NbCoSn and TaFeSb, both show Curie-Weiss-like behavior revealing paramagnetic-type defects. The constant spin-lattice relaxation rates represent the partial Fermi-level DOS of the probed site, indicating the metallic behavior across the measured temperature range. The paramagnetic shifts can be understood as degenerate *d* bands splitting and mixing in the conduction and valence bands. The observed trends of chemical shift *vs* electronegativity and lattice constant can be connected to variations in the *d*-electron hybridization in half-Heuslers. The DFT computed results give an overall reasonable prediction of NMR chemical shifts for half-Heusler materials. The largest shifts are observed to exceed what is predicted, and I discuss a likely mechanism due to electron-electron enhanced Van Vleck susceptibility.

The other thermoelectric family studied here is skutterudite. ^{59}Co NMR and transport results of filled skutterudites $Ba_xYb_yCo_4Sb_{12}$ and $A_xCo_4Sb_{12}$ (A = Ba, Sr) demonstrate the existence of a shallow defect level below conduction band minimum. The NMR and transport results were analyzed in a very general way allowing the Hall effect as well as Knight shift and T_1 results to be fitted numerically as the carriers slowly changed from metallic to non-degenerate situation. These fits yield an effective mass in good agreement with predicted values and indicate that the gradual changes in Hall coefficient observed at low temperatures in filled $CoSb_3$ are associated with a defect state positioned close to the conduction band minimum. Additionally, the measured Seebeck coefficient data were also treated within the same general model and found to reasonably agree with parameters derived from the other measurements.

Two topological chalcogenides included in this dissertation are $ZrTe_5$ and $ZrTe_2$. NMR is shown to be an effective technique to reveal useful information, such as topological and electronic

properties about topological materials. For the first topological chalcogenide material $ZrTe_5$, its electronic structure and topological nature were investigated using ^{125}Te NMR technique combined with DFT calculations. Results for the $B \parallel a$ orientation show that the Dirac band gap closes and reopens at a Lifshitz transition with temperature increasing, which corresponds to a topological phase transition from weak to strong topological insulator. I also show that the NMR T_1 results provide a very sensitive measure of the Dirac electrons involved in this transition. DFT calculations give further details about the band inversion, providing a better understanding of the topological phase transition. The observed shift change of Te_z site at T_c give direct evidence of the band inversion of symmetry occurring at the topological phase transition point.

For transition-metal dichalcogenide $ZrTe_2$, the topological nature of transition metal dichalcogenide $ZrTe_2$ is revealed here as a quasi-2D Dirac semimetal with a nodal line between Γ and A. For magnetic fields perpendicular to the $ZrTe_2$ layers, the measured shift can be well-modeled by a combination of orbital shift and spin shift due to high mobility Dirac carriers. At low temperatures, the measured spin-lattice relaxation rates can be explained through a quasi-2D Dirac electron model. In the intermediate temperature range, the observed fast drop of the spin-lattice relaxation rate for the $B \parallel c$ orientation is shown to correspond to an increase in scattering of the Dirac carriers. With temperature further increasing, the local orbital contribution starts to dominate the spin-lattice relaxation rate with the significant contribution of a split-off band.

REFERENCES

[1] M. A. Kouacou, J. Pierre, and R. V. Skolozdra, "Semiconductor-metal transition and the onset of itinerant ferromagnetism in the Heusler phases TiCoSn-TiCoSb," *J. Phys. Condens. Matter*, vol. 7, p. 7373, 1995.

[2] J. Pierre, R. V. Skolozdra, J. Tobola, S. Kaprzyk, C. Hordequin, M. A. Kouacou, I. Karla, R. Currat, and E. Lelievre-Berna, "Properties on request in semi-Heusler phases," *J. Alloys Compd.*, vol. 262, pp. 101–107, 1997.

[3] J. Tobola, J. Pierre, S. Kaprzyk, R. V. Skolozdra, and M. A. Kouacou, "Crossover from semiconductor to magnetic metal in semi-Heusler phases as a function of valence electron concentration," *J. Phys. Condens. Matter*, vol. 10, p. 1013, 1998.

[4] F. G. Aliev, N. B. Brandt, V. V. Moshchalkov, V. V. Kozyrkov, R. V. Skolozdra, and A. I. Belogorokhov, "Gap at the Fermi level in the intermetallic vacancy system RBiSn (R = Ti, Zr, Hf)," *Z. Phys.*, vol. 75, pp. 167–171, 1989.

[5] F. G. Aliev, V. V. l. Kozyrkov, V. V. Moshchalkov, R. V. Scolozdra, and K. Durczewski, "Narrow band in the intermetallic compounds MNiSn (M = Ti, Zr, Hf)," *Z. Phys.*, vol. 80, pp. 353–357, 1990.

[6] D. P. Young, P. Khalifah, R. J. Cava, and A. P. Ramirez, "Thermoelectric properties of pure and doped FeMSb (M = V, Nb)," *J. Appl. Phys.*, vol. 87, pp. 317–321, 2000.

[7] H. C. Kandpal, C. Felser, and R. Seshadri, "Covalent bonding and the nature of band gaps in some half-Heusler compounds," *J. Phys. D.*, vol. 39, p. 776, 2006.

[8] T. Graf, C. Felser, and S. S. P. Parkin, "Simple rules for the understanding of Heusler compounds," *Prog. Solid State Chem.*, vol. 39, pp. 1–50, 2011.

[9] H. Hohl, A. P. Ramirez, C. Goldmann, G. Ernst, B. Wölfing, and E. Bucher, "Efficient dopants for ZrNiSn-based thermoelectric materials," *J. Phys. Condens. Matter*, vol. 11,

p. 1697, 1999.

[10] C. Shi, X. Xi, Z. Hou, X. Zhang, G. Xu, E. Liu, W. Wang, W. Wang, J. Chen, and G. Wu, "NMR investigation of atomic and electronic structures of half-Heusler topologically nontrivial semimetals," *Phys. Status Solidi*, vol. 252, pp. 357–360, 2015.

[11] B. Nowak and D. Kaczorowski, "NMR as a probe of band inversion in topologically nontrivial half-Heusler compounds," *J. Phys. Chem. C*, vol. 118, no. 31, pp. 18021–18026, 2014.

[12] X. Zhang, Z. Hou, Y. Wang, G. Xu, C. Shi, E. Liu, X. Xi, W. Wang, G. Wu, and X.-x. Zhang, "NMR evidence for the topologically nontrivial nature in a family of half-Heusler compounds," *Sci. Rep.*, vol. 6, p. 23172, 2016.

[13] Y. Tian, A. A. Sirusi, S. Ballikaya, N. Ghassemi, C. Uher, and J. H. Ross, Jr., "Charge-carrier behavior in Ba-, Sr-and Yb-filled $CoSb_3$: NMR and transport studies," *Phys. Rev. B*, vol. 99, p. 125109, 2019.

[14] N. Ghassemi, X. Lu, Y. Tian, E. Conant, Y. Yan, X. Zhou, and J. H. Ross, Jr., "Structure change and rattling dynamics in $Cu_{12}Sb_4S_{13}$ tetrahedrite: an NMR Study," *ACS Appl. Mater. Interfaces*, vol. 10, pp. 36010–36017, 2018.

[15] Y. Tian, H. Zhu, W. Ren, N. Ghassemi, E. Conant, Z. Wang, Z. Ren, and J. H. Ross, Jr., "Native defects and impurity band behavior in half-Heusler thermoelectric NbFeSb," *Phys. Chem. Chem. Phys.*, vol. 20, pp. 21960–21967, 2018.

[16] B. Nowak, O. Pavlosiuk, and D. Kaczorowski, "Band inversion in topologically nontrivial half-Heusler bismuthides: ^{209}Bi NMR study," *J. Phys. Chem. C*, vol. 119, no. 5, pp. 2770–2774, 2015.

[17] B. Nowak and D. Kaczorowski, "^{209}Bi NMR in topologically trivial and nontrivial half-Heusler bismuthides," *J. Phys. Chem. C*, vol. 120, no. 38, pp. 21797–21801, 2016.

[18] A. Grykałowska, K. Wochowski, and B. Nowak, "Semi-Heusler-type intermetallics MPtSn (M = Ti, Zr, Hf, Th): a magnetic susceptibility and NMR study," *Intermetallics*, vol. 13, no. 7, pp. 756–763, 2005.

[19] H. Nishihara, T. Kanomata, Y. Furutani, T. Igarashi, K. Koyama, and T. Goto, "NMR properties of half-Heusler CoVSb," *Phys. Status Solidi C*, vol. 3, no. 8, pp. 2779–2782, 2006.

[20] V. Ksenofontov, G. Melnyk, M. Wojcik, S. Wurmehl, K. Kroth, S. Reiman, P. Blaha, and C. Felser, "Structure and properties of CoMnSb in the context of half-metallic ferromagnetism," *Phys. Rev. B*, vol. 74, no. 13, p. 134426, 2006.

[21] T. Harmening, H. Eckert, and R. Pöttgen, "Defects in half-Heusler type antimonides ScTSb (T = Ni, Pd, Pt)," *Solid State Sci.*, vol. 11, no. 4, pp. 900–906, 2009.

[22] C.-S. Lue, C. F. Chen, F.-K. Chiang, and M.-W. Chu, "Annealing effect on the reduction of Fermi-level density of states in CoTiSb: NMR evidence," *Phys. Rev. B*, vol. 80, p. 174202, 2009.

[23] B. Nowak and D. Kaczorowski, "Nonmetallic behaviour in half-Heusler phases YPdSb, YPtSb and LuPtSb," *Intermetallics*, vol. 40, pp. 28–35, 2013.

[24] Y. Tian, N. Ghassemi, W. Ren, H. Zhu, S. Li, Q. Zhang, Z. Wang, Z. Ren, and J. H. Ross, Jr., "Half-Heusler thermoelectric materials: NMR studies," *J. Appl. Phys.*, vol. 128, p. 055106, 2020.

[25] T. Koyama, M. Abe, T. Mito, K.-i. Ueda, T. Kohara, and H. S. Suzuki, "NMR studies of half-Heusler type compounds YbPtSb and LuPtSb," *J. Phys. Soc. Jpn.*, vol. 80, no. Suppl. A, p. SA097, 2011.

[26] C. Lue, Y. Oner, D. Naugle, and J. H. Ross, "Magnetism of new semi-Heusler compounds FeVSn and CoVSn," *IEEE Trans. Magn.*, vol. 37, no. 4, pp. 2138–2140, 2001.

[27] A. Grykałowska and B. Nowak, "Nuclear spin-lattice relaxation in narrow gap semiconductors TiPtSn and ZrPtSn," *Intermetallics*, vol. 15, no. 11, pp. 1479–1482, 2007.

[28] G. Mamniashvili, T. Gegechkori, and T. Gavasheli, "On the ^{55}Mn NMR Echo Enhancement in Half-Metallic Heusler Compound NiMnSb in Applied Magnetic Fields," *J. Supercond. Nov. Magn.*, vol. 30, no. 10, pp. 2981–2984, 2017.

[29] R. He, D. Kraemer, J. Mao, L. Zeng, Q. Jie, Y. Lan, C. Li, J. Shuai, H. S. Kim, Y. Liu, *et al.*, "Achieving high power factor and output power density in *p*-type half-Heuslers $Nb_{1-x}Ti_xFeSb$," *Proc. Natl. Acad. Sci. U.S.A.*, vol. 113, pp. 13576–13581, 2016.

[30] W. Ren, H. Zhu, Q. Zhu, U. Saparamadu, R. He, Z. Liu, J. Mao, C. Wang, K. Nielsch, Z. Wang, *et al.*, "Ultrahigh Power Factor in Thermoelectric System $Nb_{0.95}M_{0.05}FeSb$ (M = Hf, Zr, and Ti)," *Adv. Sci.*, vol. 5, p. 1800278, 2018.

[31] J. Yu, C. Fu, Y. Liu, K. Xia, U. Aydemir, T. C. Chasapis, G. J. Snyder, X. Zhao, and T. Zhu, "Unique Role of Refractory Ta Alloying in Enhancing the Figure of Merit of NbFeSb Thermoelectric Materials," *Adv. Energy Mater.*, vol. 8, p. 1701313, 2018.

[32] C. Fu, S. Bai, Y. Liu, Y. Tang, L. Chen, X. Zhao, and T. Zhu, "Realizing high figure of merit in heavy-band *p*-type half-Heusler thermoelectric materials," *Nat. Commun.*, vol. 6, p. 8144, 2015.

[33] G. Rogl, P. Sauerschnig, Z. Rykavets, V. Romaka, P. Heinrich, B. Hinterleitner, A. Grytsiv, E. Bauer, and P. Rogl, "(V, Nb)-doped half Heusler alloys based on {Ti, Zr, Hf}NiSn with high ZT," *Acta Mater.*, vol. 131, pp. 336–348, 2017.

[34] H. Zhu, R. He, J. Mao, Q. Zhu, C. Li, J. Sun, W. Ren, Y. Wang, Z. Liu, Z. Tang, *et al.*, "Discovery of ZrCoBi based half Heuslers with high thermoelectric conversion efficiency," *Nat. Commun.*, vol. 9, p. 2497, 2018.

[35] H. Zhu, J. Mao, Y. Li, J. Sun, Y. Wang, Q. Zhu, G. Li, Q. Song, J. Zhou, Y. Fu, *et al.*, "Discovery of TaFeSb-based half-Heuslers with high thermoelectric performance," *Nat. Commun.*, vol. 10, p. 270, 2019.

[36] L. Chen, X. Zeng, T. M. Tritt, and S. J. Poon, "Half-Heusler alloys for efficient thermoelectric power conversion," *J. Electron. Mater.*, vol. 45, pp. 5554–5560, 2016.

[37] C. Uher, J. Yang, S. Hu, D. T. Morelli, and G. P. Meisner, "Transport properties of pure and doped MNiSn (M = Zr, Hf)," *Phys. Rev. B*, vol. 59, p. 8615, 1999.

[38] M. Wambach, R. Stern, S. Bhattacharya, P. Ziolkowski, E. Müller, G. K. Madsen, and A. Ludwig, "Unraveling Self-Doping Effects in Thermoelectric TiNiSn Half-Heusler Compounds by Combined Theory and High-Throughput Experiments," *Adv. Electron. Mater.*, vol. 2, p. 21500208, 2016.

[39] G. J. Snyder and E. S. Toberer, "Complex thermoelectric materials," *Nat. Mater.*, vol. 7, p. 105, 2008.

[40] R. He, H. S. Kim, Y. Lan, D. Wang, S. Chen, and Z. Ren, "Investigating the thermoelectric properties of p-type half-Heusler $Hf_x(ZrTi)_{1-x}CoSb_{0.8}Sn_{0.2}$ by reducing Hf concentration for power generation," *RSC Adv.*, vol. 4, pp. 64711–64716, 2014.

[41] S. Ballikaya, G. Wang, K. Sun, and C. Uher, "Thermoelectric properties of triple-filled $Ba_xYb_yIn_zCo_4Sb_{12}$ skutterudites," *J. Electron. Mater.*, vol. 40, no. 5, pp. 570–576, 2011.

[42] G. P. Meisner, "Superconductivity and magnetic order in ternary rare earth transition metal phosphides," *Physica B & C*, vol. 108B, no. 1-3, pp. 763–764, 1981.

[43] A. Leithe-Jasper, W. Schnelle, H. Rosner, M. Baenitz, A. Rabis, A. A. Gippius, E. N. Morozova, H. Borrmann, U. Burkhardt, R. Ramlau, *et al.*, "Weak itinerant ferromagnetism and electronic and crystal structures of alkali-metal iron antimonides: $NaFe_4Sb_{12}$ and KFe_4Sb_{12}," *Phys. Rev. B*, vol. 70, no. 21, p. 214418, 2004.

[44] C. Sekine, T. Uchiumi, I. Shirotani, and T. Yagi, "Metal-insulator transition in $PrRu_4P_{12}$ with skutterudite structure," *Phys. Rev. Lett.*, vol. 79, no. 17, p. 3218, 1997.

[45] M. S. Torikachvili, J. W. Chen, Y. Dalichaouch, R. P. Guertin, M. W. McElfresh, C. Rossel, M. B. Maple, and G. P. Meisner, "Low-temperature properties of rare-earth and actinide iron phosphide compounds MFe_4P_{12} (M = La, Pr, Nd, and Th)," *Phys. Rev. B*, vol. 36, no. 16, p. 8660, 1987.

[46] H. Luo, J. W. Krizan, L. Muechler, N. Haldolaarachchige, T. Klimczuk, W. Xie, M. K. Fuccillo, C. Felser, and R. J. Cava, "A large family of filled skutterudites stabilized by electron count," *Nat. Commun.*, vol. 6, p. 6489, 2015.

[47] A. A. Sirusi and J. H. Ross, Jr., "Recent NMR Studies of Thermoelectric Materials," *Annu. Rep. NMR Spectrosc.*, vol. 92, pp. 137–198, 2017.

[48] G. A. Slack, "New materials and performance limits for thermoelectric cooling," in *CRC Handbook of Thermoelectrics* (D. M. Rowe, ed.), CRC Press, Boca Raton, 1995.

[49] D. T. Morelli and G. P. Meisner, "Low temperature properties of the filled skutterudite $CeFe_4Sb_{12}$," *J. Appl. Phys.*, vol. 77, no. 8, pp. 3777–3781, 1995.

[50] S. Lee, K. H. Lee, Y.-M. Kim, H. S. Kim, G. J. Snyder, S. Baik, and S. W. Kim, "Simple and efficient synthesis of nanograin structured single phase filled skutterudite for high thermoelectric performance," *Acta Mater.*, vol. 142, pp. 8–17, 2018.

[51] M. Benyahia, V. Ohorodniichuk, E. Leroy, A. Dauscher, B. Lenoir, and E. Alleno, "High thermoelectric figure of merit in mesostructured $In_{0.25}Co_4Sb_{12}$ *n*-type skutterudite," *J. Alloys Compd.*, vol. 735, pp. 1096–1104, 2018.

[52] C. Chen, L. Zhang, J. Li, F. Yu, D. Yu, Y. Tian, and B. Xu, "Enhanced thermoelectric performance of lanthanum filled $CoSb_3$ synthesized under high pressure," *J. Alloys Compd.*, vol. 699, pp. 751–755, 2017.

[53] G. Rogl, A. Grytsiv, K. Yubuta, S. Puchegger, E. Bauer, C. Raju, R. Mallik, and P. Rogl, "In-doped multifilled *n*-type skutterudites with $ZT = 1.8$," *Acta Mater.*, vol. 95, pp. 201–211, 2015.

[54] G. Li, U. Aydemir, M. Wood, W. A. Goddard III, P. Zhai, Q. Zhang, and G. J. Snyder, "Defect-Controlled Electronic Structure and Phase Stability in Thermoelectric Skutterudite $CoSb_3$," *Chem. Mater.*, vol. 29, no. 9, pp. 3999–4007, 2017.

[55] P. R. Realyvázquez-Guevara, F. J. Rivera-Gómez, A. Faudoa-Arzate, M. E. Botello-Zubiate, R. J. Sáenz-Hernández, C. R. Santillán-Rodríguez, and J. A. Matutes-Aquino, "Effect of

Native Defects on Transport Properties in Non-Stoichiometric $CoSb_3$," *Materials*, vol. 10, no. 3, p. 287, 2017.

[56] G. Li, S. Bajaj, U. Aydemir, S. Hao, H. Xiao, W. A. Goddard III, P. Zhai, Q. Zhang, and G. J. Snyder, "*P*-type Co interstitial defects in thermoelectric skutterudite $CoSb_3$ due to the breakage of Sb_4-rings," *Chem. Mater.*, vol. 28, no. 7, pp. 2172–2179, 2016.

[57] L. Xi, Y. Qiu, S. Zheng, X. Shi, J. Yang, L. Chen, D. J. Singh, J. Yang, and W. Zhang, "Complex doping of group 13 elements In and Ga in caged skutterudite $CoSb_3$," *Acta Mater.*, vol. 85, pp. 112–121, 2015.

[58] C.-H. Park and Y.-S. Kim, "Atomic and electronic structures of Co-related point defects in $CoSb_3$," *J. Electron. Mater.*, vol. 40, no. 5, pp. 962–966, 2011.

[59] C.-H. Park and Y.-S. Kim, "Ab initio study of native point-defects in $CoSb_3$: Understanding off-stoichiometric doping properties," *Phys. Rev. B*, vol. 81, no. 8, p. 085206, 2010.

[60] B. A. Volkov and O. A. Pankratov, "Two-dimensional massless electrons in an inverted contact," *JETP Lett.*, vol. 42, no. 49, p. 178, 1985.

[61] O. A. Pankratov, S. V. Pakhomov, and B. A. Volkov, "Supersymmetry in heterojunctions: Band-inverting contact on the basis of $Pb_{1-x}Sn_xTe$ and $Hg_{1-x}Cd_xTe$," *Solid State Commun.*, vol. 61, no. 2, pp. 93–96, 1987.

[62] C. L. Kane and E. J. Mele, "Z_2 topological order and the quantum spin Hall effect," *Phys. Rev. Lett.*, vol. 95, no. 14, p. 146802, 2005.

[63] B. A. Bernevig and S.-C. Zhang, "Quantum spin Hall effect," *Phys. Rev. Lett.*, vol. 96, no. 10, p. 106802, 2006.

[64] J. E. Moore and L. Balents, "Topological invariants of time-reversal-invariant band structures," *Phys. Rev. B*, vol. 75, no. 12, p. 121306, 2007.

[65] J. M. Kosterlitz and D. J. Thouless, "Ordering, metastability and phase transitions in two-dimensional systems," *J. Phys. C*, vol. 6, no. 7, p. 1181, 1973.

[66] L. Fu, "Topological crystalline insulators," *Phys. Rev. Lett.*, vol. 106, no. 10, p. 106802, 2011.

[67] P. A. M. Dirac, *The principles of quantum mechanics*. No. 27, Oxford university press, 1981.

[68] Z. Wang, Y. Sun, X.-Q. Chen, C. Franchini, G. Xu, H. Weng, X. Dai, and Z. Fang, "Dirac semimetal and topological phase transitions in A_3Bi (A = Na, K, Rb)," *Phys. Rev. B*, vol. 85, no. 19, p. 195320, 2012.

[69] Z. Wang, H. Weng, Q. Wu, X. Dai, and Z. Fang, "Three-dimensional Dirac semimetal and quantum transport in Cd_3As_2," *Phys. Rev. B*, vol. 88, no. 12, p. 125427, 2013.

[70] Z. K. Liu, B. Zhou, Y. Zhang, Z. J. Wang, H. M. Weng, D. Prabhakaran, S.-K. Mo, Z. X. Shen, Z. Fang, X. Dai, *et al.*, "Discovery of a three-dimensional topological Dirac semimetal, Na_3Bi," *Science*, vol. 343, no. 6173, pp. 864–867, 2014.

[71] Z. K. Liu, J. Jiang, B. Zhou, Z. J. Wang, Y. Zhang, H. M. Weng, D. Prabhakaran, S. K. Mo, H. Peng, P. Dudin, *et al.*, "A stable three-dimensional topological Dirac semimetal Cd_3As_2," *Nat. Mater.*, vol. 13, no. 7, pp. 677–681, 2014.

[72] N. P. Armitage, E. J. Mele, and A. Vishwanath, "Weyl and Dirac semimetals in three-dimensional solids," *Rev. Mod. Phys.*, vol. 90, no. 1, p. 015001, 2018.

[73] Q. Li, D. E. Kharzeev, C. Zhang, Y. Huang, I. Pletikosić, A. V. Fedorov, R. D. Zhong, J. A. Schneeloch, G. D. Gu, and T. Valla, "Chiral magnetic effect in $ZrTe_5$," *Nat. Phys.*, vol. 12, p. 550, 2016.

[74] F. Tang, Y. Ren, P. Wang, R. Zhong, J. Schneeloch, S. A. Yang, K. Yang, P. A. Lee, G. Gu, Z. Qiao, *et al.*, "Three-dimensional quantum Hall effect and metal-insulator transition in $ZrTe_5$," *Nature*, vol. 569, pp. 537–541, 2019.

[75] H. Weng, X. Dai, and Z. Fang, "Transition-Metal Pentatelluride $ZrTe_5$ and $HfTe_5$: A Paradigm for Large-Gap Quantum Spin Hall Insulators," *Phys. Rev. X*, vol. 4, p. 011002, 2014.

[76] S. R. Lee, P. A. Sharma, A. L. Lima-Sharma, W. Pan, and T. M. Nenoff, "Topological quantum materials for realizing Majorana quasiparticles," *Chem. Mater.*, vol. 31, pp. 26–51, 2018.

[77] G. Manzoni, L. Gragnaniello, G. Autès, T. Kuhn, A. Sterzi, F. Cilento, M. Zacchigna, V. Enenkel, I. Vobornik, L. Barba, *et al.*, "Evidence for a Strong Topological Insulator Phase in $ZrTe_5$," *Phys. Rev. Lett.*, vol. 117, p. 237601, 2016.

[78] Z. Fan, Q.-F. Liang, Y. B. Chen, S.-H. Yao, and J. Zhou, "Transition between strong and weak topological insulator in $ZrTe_5$ and $HfTe_5$," *Sci. Rep.*, vol. 7, p. 45667, 2017.

[79] L. Shen, M. X. Wang, S. C. Sun, J. Jiang, X. Xu, T. Zhang, Q. H. Zhang, Y. Y. Lv, S. H. Yao, Y. B. Chen, *et al.*, "Spectroscopic evidence for the gapless electronic structure in bulk $ZrTe_5$," *J. Electron Spectrosc. Relat. Phenom.*, vol. 219, pp. 45–52, 2017.

[80] R. Y. Chen, S. J. Zhang, J. A. Schneeloch, C. Zhang, Q. Li, G. D. Gu, and N. L. Wang, "Optical spectroscopy study of the three-dimensional Dirac semimetal $ZrTe_5$," *Phys. Rev. B*, vol. 92, p. 075107, 2015.

[81] R. Y. Chen, Z. G. Chen, X.-Y. Song, J. A. Schneeloch, G. D. Gu, F. Wang, and N. L. Wang, "Magnetoinfrared Spectroscopy of Landau Levels and Zeeman Splitting of Three-Dimensional Massless Dirac Fermions in $ZrTe_5$," *Phys. Rev. Lett.*, vol. 115, p. 176404, 2015.

[82] G. Zheng, J. Lu, X. Zhu, W. Ning, Y. Han, H. Zhang, J. Zhang, C. Xi, J. Yang, H. Du, *et al.*, "Transport evidence for the three-dimensional Dirac semimetal phase in $ZrTe_5$," *Phys. Rev. B*, vol. 93, p. 115414, 2016.

[83] L. Moreschini, J. C. Johannsen, H. Berger, J. Denlinger, C. Jozwiak, E. Rotenberg, K. S. Kim, A. Bostwick, and M. Grioni, "Nature and topology of the low-energy states in $ZrTe_5$," *Phys. Rev. B*, vol. 94, p. 081101(R), 2016.

[84] X.-B. Li, W.-K. Huang, Y.-Y. Lv, K.-W. Zhang, C.-L. Yang, B.-B. Zhang, Y. B. Chen, S.-H. Yao, J. Zhou, M.-H. Lu, *et al.*, "Experimental Observation of Topological Edge States at the

Surface Step Edge of the Topological Insulator $ZrTe_5$," *Phys. Rev. Lett.*, vol. 116, p. 176803, 2016.

[85] R. Wu, J.-Z. Ma, S.-M. Nie, L.-X. Zhao, X. Huang, J.-X. Yin, B.-B. Fu, P. Richard, G.-F. Chen, Z. Fang, *et al.*, "Evidence for Topological Edge States in a Large Energy Gap near the Step Edges on the Surface of $ZrTe_5$," *Phys. Rev. X*, vol. 6, p. 021017, 2016.

[86] Y.-Y. Lv, B.-B. Zhang, X. Li, K.-W. Zhang, X.-B. Li, S.-H. Yao, Y. B. Chen, J. Zhou, S.-T. Zhang, M.-H. Lu, *et al.*, "Shubnikov-de Haas oscillations in bulk $ZrTe_5$ single crystals: Evidence for a weak topological insulator," *Phys. Rev. B*, vol. 97, p. 115137, 2018.

[87] G. Manzoni, A. Crepaldi, G. Autès, A. Sterzi, F. Cilento, A. Akrap, I. Vobornik, L. Gragnaniello, P. Bugnon, M. Fonin, *et al.*, "Temperature dependent non-monotonic bands shift in $ZrTe_5$," *J. Electron Spectrosc. Relat. Phenom.*, vol. 219, pp. 9–15, 2017.

[88] B. Xu, L. X. Zhao, P. Marsik, E. Sheveleva, F. Lyzwa, Y. M. Dai, G. F. Chen, X. G. Qiu, and C. Bernhard, "Temperature-Driven Topological Phase Transition and Intermediate Dirac Semimetal Phase in $ZrTe_5$," *Phys. Rev. Lett.*, vol. 121, p. 187401, 2018.

[89] Y. Zhang, C. Wang, L. Yu, G. Liu, A. Liang, J. Huang, S. Nie, X. Sun, Y. Zhang, B. Shen, *et al.*, "Electronic evidence of temperature-induced Lifshitz transition and topological nature in $ZrTe_5$," *Nat. Commun.*, vol. 8, p. 15512, 2017.

[90] S. Manzeli, D. Ovchinnikov, D. Pasquier, O. V. Yazyev, and A. Kis, "2D transition metal dichalcogenides," *Nat. Rev. Mater.*, vol. 2, p. 17033, 2017.

[91] A. J. S. Machado, N. P. Baptista, B. S. de Lima, N. Chaia, T. W. Grant, L. E. Corrêa, S. T. Renosto, A. C. Scaramussa, R. F. Jardim, M. S. Torikachvili, J. A. Aguiar, O. C. Cigarroa, L. T. F. Eleno, and Z. Fisk, "Evidence for topological behavior in superconducting Cu_xZrTe_{2-y}," *Phys. Rev. B*, vol. 95, p. 144505, 2017.

[92] P. Tsipas, D. Tsoutsou, S. Fragkos, R. Sant, C. Alvarez, H. Okuno, G. Renaud, R. Alcotte, T. Baron, and A. Dimoulas, "Massless dirac fermions in $ZrTe_2$ semimetal grown on InAs(111) by van der Waals epitaxy," *ACS Nano*, vol. 12, pp. 1696–1703, 2018.

[93] I. Kar, J. Chatterjee, L. Harnagea, Y. Kushnirenko, A. V. Fedorov, D. Shrivastava, B. Büchner, P. Mahadevan, and S. Thirupathaiah, "Metal-chalcogen bond-length induced electronic phase transition from semiconductor to topological semimetal in ZrX_2 (X = Se and Te)," *Phys. Rev. B*, vol. 101, p. 165122, 2020.

[94] W. Zhang, P. Wang, B. Skinner, R. Bi, V. Kozii, C.-W. Cho, R. Zhong, J. Schneeloch, D. Yu, G. Gu, *et al.*, "Observation of a thermoelectric Hall plateau in the extreme quantum limit," *Nat. Commun.*, vol. 11, no. 1, p. 1046, 2020.

[95] C. Vaswani, L.-L. Wang, D. H. Mudiyanselage, Q. Li, P. M. Lozano, G. D. Gu, D. Cheng, B. Song, L. Luo, R. H. J. Kim, *et al.*, "Light-Driven Raman Coherence as a Nonthermal Route to Ultrafast Topology Switching in a Dirac Semimetal," *Phys. Rev. X*, vol. 10, no. 2, p. 021013, 2020.

[96] Y. Tian, N. Ghassemi, and J. H. Ross, Jr., "Dirac electron behavior and NMR evidence for topological band inversion in $ZrTe_5$," *Phys. Rev. B*, vol. 100, p. 165149, 2019.

[97] S. Takahashi, T. Sambongi, J. W. Brill, and W. Roark, "Transport and elastic anomalies in $ZrTe_3$," *Solid State Commun.*, vol. 49, pp. 1031–1034, 1984.

[98] Z. Zhu, G. W. Winkler, Q. S. Wu, J. Li, and A. A. Soluyanov, "Triple point topological metals," *Phys. Rev. X*, vol. 6, p. 031003, 2016.

[99] A. H. Reshak and S. Auluck, "Theoretical investigation of the electronic and optical properties of ZrX_2 (X = S, Se and Te)," *Physica B*, vol. 353, pp. 230–237, 2004.

[100] H. Guo, N. Lu, L. Wang, X. Wu, and X. C. Zeng, "Tuning electronic and magnetic properties of early transition-metal dichalcogenides via tensile strain," *J. Phys. Chem. C*, vol. 118, pp. 7242–7249, 2014.

[101] Z. Muhammad, B. Zhang, H. Lv, H. Shan, Z. u. Rehman, S. Chen, Z. Sun, X. Wu, A. Zhao, and L. Song, "A Transition from Semimetal to Semiconductor in $ZrTe_2$ Induced by Se Substitution," *ACS Nano*, vol. 14, pp. 835–841, 2019.

[102] Z. Okvátovity, H. Yasuoka, M. Baenitz, F. Simon, and B. Dóra, "Nuclear spin-lattice relaxation time in TaP and the Knight shift of Weyl semimetals," *Phys. Rev. B*, vol. 99, p. 115107, 2019.

[103] C. G. Wang, Y. Honjo, L. X. Zhao, G. F. Chen, K. Matano, R. Zhou, and G.-q. Zheng, "Landau diamagnetism and Weyl-fermion excitations in TaAs revealed by ^{75}As NMR and NQR," *Phys. Rev. B*, vol. 101, no. 24, p. 241110, 2020.

[104] M. Hirata, K. Ishikawa, G. Matsuno, A. Kobayashi, K. Miyagawa, M. Tamura, C. Berthier, and K. Kanoda, "Anomalous spin correlations and excitonic instability of interacting 2D Weyl fermions," *Science*, vol. 358, no. 6369, pp. 1403–1406, 2017.

[105] D. Koumoulis, T. C. Chasapis, R. E. Taylor, M. P. Lake, D. King, N. N. Jarenwattananon, G. A. Fiete, M. G. Kanatzidis, and L.-S. Bouchard, "NMR probe of metallic states in nanoscale topological insulators," *Phys. Rev. Lett.*, vol. 110, no. 2, p. 026602, 2013.

[106] W. Papawassiliou, A. Jaworski, A. J. Pell, J. H. Jang, Y. Kim, S.-C. Lee, H. J. Kim, Y. Alwahedi, S. Alhassan, A. Subrati, *et al.*, "Resolving Dirac electrons with broadband high-resolution NMR," *Nat. Commun.*, vol. 11, no. 1, p. 1285, 2020.

[107] I. I. Rabi, J. R. Zacharias, S. Millman, and P. Kusch, "A New Method of Measuring Nuclear Magnetic Moment," *Phys. Rev.*, vol. 53, pp. 318–318, 1938.

[108] F. Bloch, W. W. Hansen, and M. Packard, "Nuclear Induction," *Phys. Rev.*, vol. 69, pp. 127–127, 1946.

[109] E. M. Purcell, H. C. Torrey, and R. V. Pound, "Resonance Absorption by Nuclear Magnetic Moments in a Solid," *Phys. Rev.*, vol. 69, pp. 37–38, 1946.

[110] E. R. Andrew, A. Bradbury, and R. G. Eades, "Nuclear Magnetic Resonance Spectra from a Crystal rotated at High Speed," *Nature*, vol. 182, no. 4650, p. 1659, 1958.

[111] I. J. Lowe, "Free induction decays of rotating solids," *Phys. Rev. Lett.*, vol. 2, no. 7, p. 285, 1959.

[112] B. H. Toby and R. B. Von Dreele, "*GSAS-II*: the genesis of a modern open-source all purpose crystallography software package," *J. Appl. Crystallogr.*, vol. 46, pp. 544–549, 2013.

[113] P. Blaha, K. Schwarz, F. Tran, R. Laskowski, G. K. H. Madsen, and L. D. Marks, "WIEN2k: An APW+lo program for calculating the properties of solids," *J. Chem. Phys.*, vol. 152, p. 074101, 2020.

[114] A. Kokalj, "XCrySDen—a new program for displaying crystalline structures and electron densities," *J. Mol. Graph. Model.*, vol. 17, pp. 176–179, 1999.

[115] K. Momma and F. Izumi, "*VESTA* 3 for three-dimensional visualization of crystal, volumetric and morphology data," *J. Appl. Crystallogr.*, vol. 44, pp. 1272–1276, 2011.

[116] C. B. H. Evers, C. G. Richter, K. Hartjes, and W. Jeitschko, "Ternary transition metal antimonides and bismuthides with MgAgAs-type and filled NiAs-type structure," *J. Alloys Compd.*, vol. 252, pp. 93–97, 1997.

[117] G. Melnyk, E. Bauer, P. Rogl, R. Skolozdra, and E. Seidl, "Thermoelectric properties of ternary transition metal antimonides," *J. Alloys Compd.*, vol. 296, pp. 235–242, 2000.

[118] A. Tavassoli, F. Failamani, A. Grytsiv, G. Rogl, P. Heinrich, H. Müller, E. Bauer, M. Zehetbauer, and P. Rogl, "On the Half-Heusler compounds $Nb_{1-x}\{Ti, Zr, Hf\}_x$FeSb: Phase relations, thermoelectric properties at low and high temperature, and mechanical properties," *Acta Mater.*, vol. 135, pp. 263–276, 2017.

[119] W. Li, G. Yang, and J. Zhang, "Optimization of the thermoelectric properties of FeNbSb-based half-Heusler materials," *J. Phys. D*, vol. 49, p. 195601, 2016.

[120] A. Roy, J. W. Bennett, K. M. Rabe, and D. Vanderbilt, "Half-Heusler semiconductors as piezoelectrics," *Phys. Rev. Lett.*, vol. 109, p. 037602, 2012.

[121] N. F. Mott, *Metal-Insulator Transitions*. Taylor & Francis, London, 1990.

[122] J. Mason, "NMR spectroscopy of the early transition metals," *Polyhedron*, vol. 8, pp. 1657–1668, 1989.

[123] A. Grykałowska and B. Nowak, "High-resolution solid-state ^{119}Sn and ^{195}Pt NMR studies of MPtSn semiconductors (M = Ti, Zr, Hf, Th)," *Solid State Nucl. Magn. Reson.*, vol. 27, pp. 223–227, 2005.

[124] D. Li, H. Zhao, S. Li, B. Wei, J. Shuai, C. Shi, X. Xi, P. Sun, S. Meng, L. Gu, *et al.*, "Atomic Disorders Induced by Silver and Magnesium Ion Migrations Favor High Thermoelectric Performance in α-MgAgSb-Based Materials," *Adv. Funct. Mater.*, vol. 25, pp. 6478–6488, 2015.

[125] S. Z. Ageev and B. C. Sanctuary, "Analytical solutions for spin 7/2 line intensities in solid state NMR," *Mol. Phys.*, vol. 84, pp. 835–844, 1995.

[126] R. E. Walstedt and L. R. Walker, "Nuclear-resonance line shapes due to magnetic impurities in metals," *Phys. Rev. B*, vol. 9, p. 4857, 1974.

[127] C. S. Lue, J. H. Ross, Jr., K. D. D. Rathnayaka, D. G. Naugle, S. Y. Wu, and W.-H. Li, "Superparamagnetism and magnetic defects in Fe_2VAl and Fe_2VGa," *J. Phys. Condens. Matter*, vol. 13, p. 1585, 2001.

[128] C. S. Lue, Y. Li, J. H. Ross, Jr., and G. M. Irwin, "NMR and Mössbauer study of spin dynamics and electronic structure of $Fe_{2+x}V_{1-x}Al$ and Fe_2VGa," *Phys. Rev. B*, vol. 67, p. 224425, 2003.

[129] D. Tse and S. R. Hartmann, "Nuclear spin-lattice relaxation via paramagnetic centers without spin diffusion," *Phys. Rev. Lett.*, vol. 21, p. 511, 1968.

[130] J. V. Kranendonk and M. B. Walker, "Theory of spin–lattice relaxation in anharmonic crystals," *Can. J. Phys.*, vol. 46.

[131] R. Dupree, D. J. Kirby, and W. W. Warren Jr, "Melting-induced electron localization: ^{133}Cs NMR study of solid and liquid CsAu," *Phys. Rev. B*, vol. 31, p. 5597, 1985.

[132] T. Fang, S. Zheng, H. Chen, H. Cheng, L. Wang, and P. Zhang, "Electronic structure and thermoelectric properties of *p*-type half-Heusler compound NbFeSb: a first-principles study," *RSC Adv.*, vol. 6, pp. 10507–10512, 2016.

[133] A. J. Hong, L. Li, R. He, J. J. Gong, Z. B. Yan, K. F. Wang, J.-M. Liu, and Z. F. Ren, "Full-scale computation for all the thermoelectric property parameters of half-Heusler compounds," *Sci. Rep.*, vol. 6, p. 22778, 2016.

[134] O. M. Abid, S. Menouer, A. Yakoubi, H. Khachai, S. B. Omran, G. Murtaza, D. Prakash, R. Khenata, and K. D. Verma, "Structural, electronic, elastic, thermoelectric and thermodynamic properties of the NbMSb half heusler (M = Fe, Ru, Os) compounds with first principle calculations," *Superlattices Microstruct.*, vol. 93, pp. 171–185, 2016.

[135] C. S. Lue, J. H. Ross, Jr., C. F. Chang, and H. D. Yang, "Field-dependent specific heat in Fe_2VAl and the question of possible 3*d* heavy fermion behavior," *Phys. Rev. B*, vol. 60, p. R13941, 1999.

[136] C. Çoban, K. Çolakoğlu, and Y. Ö. Çiftçi, "First principles study of the structural, mechanical, phonon, optical, and thermodynamic properties of half-Heusler (HH) compound NbFeSb," *Phys. Scr.*, vol. 90, p. 095701, 2015.

[137] G. C. Carter, L. H. Bennett, and D. J. Kahan, *Metallic shifts in NMR: a review of the theory and comprehensive critical data compilation of metallic materials*. Pergamon, New York, 1977.

[138] Y. Yafet and V. Jaccarino, "Nuclear spin relaxation in transition metals; core polarization," *Phys. Rev.*, vol. 133, p. A1630, 1964.

[139] N. W. Ashcroft and N. D. Mermin, *Solid state physics*. Holt, Rinehart, and Winston, New York, 1976.

[140] S. E. Fuller, E. M. Meintjes, and W. W. Warren Jr., "Impurity NMR study of the acceptor band in Si(B)," *Phys. Rev. Lett.*, vol. 76, p. 2806, 1996.

[141] P. Sun, B. Wei, J. Zhang, J. M. Tomczak, A. Strydom, M. Søndergaard, B. B. Iversen, and F. Steglich, "Large Seebeck effect by charge-mobility engineering," *Nat. Commun.*, vol. 6, p. 7475, 2015.

[142] D. L. Cox, N. E. Bickers, and J. W. Wilkins, "Dynamic magnetic susceptibilities of valence-fluctuation Ce compounds," *J. Appl. Phys.*, vol. 57, pp. 3166–3168, 1985.

[143] A. P. Dioguardi, P. Guzman, P. F. S. Rosa, N. J. Ghimire, S. Eley, S. E. Brown, J. D. Thompson, E. D. Bauer, and F. Ronning, "Nuclear magnetic resonance investigation of the heavy fermion system $Ce_2CoAl_7Ge_4$," *Phys. Rev. B*, vol. 96, p. 245132, 2017.

[144] Y. G. Yu, X. Zhang, and A. Zunger, "Natural off-stoichiometry causes carrier doping in half-Heusler filled tetrahedral structures," *Phys. Rev. B*, vol. 95, p. 085201, 2017.

[145] Y. Tian, F. G. Vagizov, N. Ghassemi, W. Ren, H. Zhu, Z. Wang, Z. Ren, and J. H. Ross, Jr., "Defect charging and resonant levels in half-Heusler $Nb_{1-x}Ti_xFeSb$," *Mater. Today Phys.*, vol. 16, p. 100278, 2021.

[146] E. Papulovskiy, A. A. Shubin, V. V. Terskikh, C. J. Pickard, and O. B. Lapina, "Theoretical and experimental insights into applicability of solid-state ^{93}Nb NMR in catalysis," *Phys. Chem. Chem. Phys.*, vol. 15, pp. 5115–5131, 2013.

[147] K. Beshah, D. Zamir, P. Becla, P. A. Wolff, and R. G. Griffin, "Te and Cd nuclear-magnetic-resonance study of local structure and bonding in $Cd_{1-x}Zn_xTe$," *Phys. Rev. B*, vol. 36, p. 6420, 1987.

[148] D. Hobbis, R. P. Hermann, H. Wang, D. S. Parker, T. Pandey, J. Martin, K. Page, and G. S. Nolas, "Structural, Chemical, Electrical, and Thermal Properties of *n*-Type NbFeSb," *Inorg. Chem.*, vol. 58, pp. 1826–1833, 2019.

[149] J. Toboła, L. Jodin, P. Pecheur, H. Scherrer, G. Venturini, B. Malaman, and S. Kaprzyk, "Composition-induced metal-semiconductor-metal crossover in half-Heusler $Fe_{1-x}Ni_xTiSb$," *Phys. Rev. B*, vol. 64, p. 155103, 2001.

[150] A. Tavassoli, A. Grytsiv, G. Rogl, V. V. Romaka, H. Michor, M. Reissner, E. Bauer, M. Zehetbauer, and P. Rogl, "The half Heusler system $Ti_{1+x}Fe_{1.33-x}Sb$-TiCoSb with Sb/Sn substitution: phase relations, crystal structures and thermoelectric properties," *Dalton Trans.*, vol. 47, pp. 879–897, 2018.

[151] A. Gerard and F. Grandjean, "Mössbauer spectra in the presence of a fluctuating electric field gradient-applications to the cases of semi-metallic compounds," *J. Phys. Chem. Solids*, vol. 36, pp. 1365–1370, 1975.

[152] G. Amthauer, W. Lottermoser, G. Redhammer, and G. Tippelt, "Mössbauer studies of selected synthetic silicates," *Hyperfine Interact.*, vol. 113, pp. 219–248, 1998.

[153] S. Ghose, K. Tsukimura, and D. M. Hatch, "Phase transitions in ilvaite, a mixed-valence iron silicate," *Phys. Chem. Miner.*, vol. 16, pp. 483–496, 1989.

[154] L. Jodin, J. Tobola, P. Pecheur, H. Scherrer, and S. Kaprzyk, "Effect of substitutions and defects in half-Heusler FeVSb studied by electron transport measurements and KKR-CPA electronic structure calculations," *Phys. Rev. B*, vol. 70, p. 184207, 2004.

[155] Y. Obata, "Nuclear magnetic relaxation in transition metals," *J. Phys. Soc. Jpn.*, vol. 18, pp. 1020–1024, 1963.

[156] A. Knigavko, B. Mitrović, and K. V. Samokhin, "Divergence of the orbital nuclear magnetic relaxation rate in metals," *Phys. Rev. B*, vol. 75, p. 134506, 2007.

[157] A. K. Koh and D. J. Miller, "Hyperfine coupling constants and atomic parameters for electron paramagnetic resonance data," *At. Data Nucl. Data Tables*, vol. 33, pp. 235–253, 1985.

[158] J. P. Heremans, B. Wiendlocha, and A. M. Chamoire, "Resonant levels in bulk thermoelectric semiconductors," *Energy Environ. Sci.*, vol. 5, pp. 5510–5530, 2012.

[159] M. Udagawa and Y. Yanase, "Interplay of spin-orbit interaction and electron correlation on the Van Vleck susceptibility in transition metal compounds," *J. Phys. Soc. Jpn.*, vol. 79, p. 123601, 2010.

[160] H. Kontani and K. Yamada, "Electronic state and magnetic susceptibility in orbitally degenerate ($J = 5/2$) periodic Anderson model," *J. Phys. Soc. Jpn.*, vol. 66, pp. 2232–2235, 1997.

[161] R. He, H. Zhu, J. Sun, J. Mao, H. Reith, S. Chen, G. Schierning, K. Nielsch, and Z. Ren, "Improved thermoelectric performance of *n*-type half-Heusler $MCo_{1-x}Ni_xSb$ (M = Hf, Zr)," *Mater. Today Phys.*, vol. 1, pp. 24–30, 2017.

[162] S. Li, H. Zhu, J. Mao, Z. Feng, X. Li, C. Chen, F. Cao, X. Liu, D. J. Singh, Z. Ren, *et al.*, "*n*-type TaCoSn-based half-Heuslers as promising thermoelectric materials," *ACS Appl. Mater. Interfaces*, vol. 11, pp. 41321–41329, 2019.

[163] R. Marazza, R. Ferro, and G. Rambaldi, "Some phases in ternary alloys of titanium, zirconium, and hafnium, with a MgAgAs or $AlCu_2Mn$ type structure," *J. Less Common Met.*, vol. 39, pp. 341–345, 1975.

[164] M. L. C. Buffon, G. Laurita, N. Verma, L. Lamontagne, L. Ghadbeigi, D. L. Lloyd, T. D. Sparks, T. M. Pollock, and R. Seshadri, "Enhancement of thermoelectric properties in the Nb-Co-Sn half-Heusler/Heusler system through spontaneous inclusion of a coherent second phase," *J. Appl. Phys.*, vol. 120, p. 075104, 2016.

[165] J. P. Perdew, K. Burke, and M. Ernzerhof, "Generalized gradient approximation made simple," *Phys. Rev. Lett.*, vol. 77, p. 3865, 1996.

[166] N. Bloembergen, "Nuclear magnetic relaxation in semiconductors," *Physica*, vol. 20, pp. 1130–1133, 1954.

[167] J. Chi, Y. Li, F. G. Vagizov, V. Goruganti, and J. H. Ross, Jr., "NMR and Mössbauer study of spin-glass behavior in $FeAl_2$," *Phys. Rev. B*, vol. 71.

[168] C. Ding, C. Qin, H. Man, T. Imai, and F. L. Ning, "NMR investigation of the diluted magnetic semiconductor $Li(Zn_{1-x}Mn_x)P$ ($x = 0.1$)," *Phys. Rev. B*, vol. 88, p. 041108, 2013.

[169] M.-S. Lee, F. P. Poudeu, and S. D. Mahanti, "Electronic structure and thermoelectric properties of Sb-based semiconducting half-Heusler compounds," *Phys. Rev. B*, vol. 83, p. 085204, 2011.

[170] M. Zahedifar and P. Kratzer, "Band structure and thermoelectric properties of half-Heusler semiconductors from many-body perturbation theory," *Phys. Rev. B*, vol. 97, p. 035204, 2018.

[171] H. Takashima, M. Hada, and H. Nakatsuji, "Theoretical study on metal NMR chemical shifts. Arsenic and antimony compounds," *J. Phys. Chem.*, vol. 99, pp. 7951–7957, 1995.

[172] C. P. Slichter, *Principles of magnetic resonance*. Springer, New York, 1990.

[173] H. Kontani and K. Yamada, "Magnetic susceptibility of the orbitally degenerate ($J = 5/2$) periodic Anderson model-analysis on the basis of the Fermi liquid theory," *J. Phys. Soc. Jpn.*, vol. 65, pp. 172–188, 1996.

[174] H. Kontani, M. Miyazawa, and K. Yamada, "Theory of anomalous Hall effect in a heavy fermion system with a strong anisotropic crystal field," *J. Phys. Soc. Jpn.*, vol. 66, pp. 2252–2255, 1997.

[175] S. Dupke, H. Eckert, F. Winter, and R. Pöttgen, "A systematic solid state NMR spectroscopic study of the equiatomic lithium half-Heusler phases LiTX(T = Mg, Zn, Cd; X = P, As, Sb, Bi)," *J. Solid State Chem.*, vol. 42, pp. 57–64, 2014.

[176] G. A. Naydenov, P. J. Hasnip, V. K. Lazarov, and M. I. J. Probert, "Huge power factor in *p*-type half-Heusler alloys NbFeSb and TaFeSb," *J. Phys. Mater.*, vol. 2, p. 035002, 2019.

[177] J.-L. Mi, M. Christensen, E. Nishibori, and B. B. Iversen, "Multitemperature crystal structures and physical properties of the partially filled thermoelectric skutterudites MCo_4Sb_{12} (M = La, Ce, Nd, Sm, Yb, and Eu)," *Phys. Rev. B*, vol. 84, no. 6, p. 064114, 2011.

[178] T. F. Kemp and M. E. Smith, "QuadFit - A new cross-platform computer program for simulation of NMR line shapes from solids with distributions of interaction parameters," *Solid State Nucl. Mag.*, vol. 35, no. 4, pp. 243–252, 2009.

[179] C. S. Lue, Y. T. Lin, and C. N. Kuo, "NMR investigation of the skutterudite compound $CoSb_3$," *Phys. Rev. B*, vol. 75, no. 7, p. 075113, 2007.

[180] C. S. Lue and S. C. Chen, "Evolution of the electronic structure in partially filled skutterudites: $Ca_xCo_4Sb_{12}$ studied using NMR," *Phys. Rev. B*, vol. 79, no. 12, p. 125108, 2009.

[181] C. S. Lue, S. M. Huang, C. N. Kuo, F.-T. Huang, and M.-W. Chu, "Effect of partial La filling on the local electronic properties of $La_xCo_4Sb_{12}$ studied using ^{59}Co NMR," *New J. Phys*, vol. 10, no. 8, p. 083029, 2008.

[182] K. Magishi, T. Kusaka, A. Hisada, T. Saito, K. Koyama, H. Sugawara, Y. Sekihara, K. Tanaka, H. Aoki, and H. Sato, "NMR/NQR Study of Filled Skutterudite $La_{0.5}Co_4Sb_{12}$," *JPS Conf. Proc.*, vol. 3, p. 011064, 2014.

[183] G. S. Nolas, G. A. Slack, T. Caillat, and G. P. Meisner, "Raman scattering study of antimony-based skutterudites," *J. Appl. Phys.*, vol. 79, no. 5, pp. 2622–2626, 1996.

[184] T. Caillat, A. Borshchevsky, and J.-P. Fleurial, "Properties of single crystalline semiconducting $CoSb_3$," *J. Appl. Phys.*, vol. 80, no. 8, pp. 4442–4449, 1996.

[185] D. Wee, B. Kozinsky, N. Marzari, and M. Fornari, "Effects of filling in $CoSb_3$: Local structure, band gap, and phonons from first principles," *Phys. Rev. B*, vol. 81, no. 4, p. 045204, 2010.

[186] J. O. Sofo and G. D. Mahan, "Electronic structure of $CoSb_3$: A narrow-band-gap semiconductor," *Phys. Rev. B*, vol. 58, no. 23, p. 15620, 1998.

[187] I. Lefebvre-Devos, M. Lassalle, X. Wallart, J. Olivier-Fourcade, L. Monconduit, and J. C. Jumas, "Bonding in skutterudites: Combined experimental and theoretical characterization of $CoSb_3$," *Phys. Rev. B*, vol. 63, no. 12, p. 125110, 2001.

[188] H. J. Goldsmid and J. W. Sharp, "Estimation of the thermal band gap of a semiconductor from Seebeck measurements," *J. Electron. Mater.*, vol. 28, no. 7, pp. 869–872, 1999.

[189] M. Puyet, B. Lenoir, A. Dauscher, P. Pécheur, C. Bellouard, J. Tobola, and J. Hejtmanek, "Electronic, transport, and magnetic properties of $Ca_xCo_4Sb_{12}$ partially filled skutterudites," *Phys. Rev. B*, vol. 73, no. 3, p. 035126, 2006.

[190] A. Narath, *Hyperfine Interactions*. Academic Press, New York, 1967.

[191] R. E. Walstedt, *The NMR Probe of High-T_c Materials and Correlated Electron Systems*. Springer, New York, 2018.

[192] J. F. Janak, "Calculated hyperfine fields and their pressure derivatives in Fe, Co, and Ni," *Phys. Rev. B*, vol. 20, no. 5, p. 2206, 1979.

[193] Y. Fu, D. J. Singh, W. Li, and L. Zhang, "Intrinsic ultralow lattice thermal conductivity of the unfilled skutterudite $FeSb_3$," *Phys. Rev. B*, vol. 94, no. 7, p. 075122, 2016.

[194] X. Zheng, S. Y. Rodriguez, and J. H. Ross, Jr., "NMR relaxation and rattling phonons in the type-I $Ba_8Ga_{16}Sn_{30}$ clathrate," *Phys. Rev. B*, vol. 84, no. 2, p. 024303, 2011.

[195] E. M. Meintjes, J. Danielson, and W. W. Warren Jr, "Temperature-dependent NMR study of the impurity state in heavily doped Si:P," *Phys. Rev. B*, vol. 71, no. 3, p. 035114, 2005.

[196] G. D. Mahan, "Figure of merit for thermoelectrics," *J. Appl. Phys.*, vol. 65, no. 4, pp. 1578–1583, 1989.

[197] E. Arushanov, M. Respaud, H. Rakoto, J. M. Broto, and T. Caillat, "Shubnikov-de Haas oscillations in $CoSb_3$ single crystals," *Phys. Rev. B*, vol. 61, no. 7, p. 4672, 2000.

[198] W. W. Warren Jr, "Nuclear Magnetic Resonance and Relaxation in the "Liquid Semiconductors" In_2Te_3, Ga_2Te_3, and Sb_2Te_3," *Phys. Rev. B*, vol. 3, no. 11, p. 3708, 1971.

[199] M. A. Paalanen, A. E. Ruckenstein, and G. A. Thomas, "Spins in Si:P close to the metal-insulator transition," *Phys. Rev. Lett.*, vol. 54, no. 12, p. 1295, 1985.

[200] Y. Tang, Z. M. Gibbs, L. A. Agapito, G. Li, H.-S. Kim, M. B. Nardelli, S. Curtarolo, and G. J. Snyder, "Convergence of multi-valley bands as the electronic origin of high thermoelectric performance in $CoSb_3$ skutterudites," *Nat. Mater.*, vol. 14, no. 12, p. 1223, 2015.

[201] H. Wang, Y. Pei, A. D. LaLonde, and G. J. Snyder, "Material design considerations based on thermoelectric quality factor," in *Thermoelectric Nanomaterials* (K. Koumoto and T. Mori, eds.), Springer, New York, 2013.

[202] J. Nagao, M. Ferhat, H. Anno, K. Matsubara, E. Hatta, and K. Mukasa, "Electron tunneling experiments on skutterudite $Co_{1-x}Fe_xSb_3$ semiconductors," *Appl. Phys. Lett.*, vol. 76, no. 23, pp. 3436–3438, 2000.

[203] J. W. Sharp, E. C. Jones, R. K. Williams, P. M. Martin, and B. C. Sales, "Thermoelectric properties of $CoSb_3$ and related alloys," *J. Appl. Phys.*, vol. 78, no. 2, pp. 1013–1018, 1995.

[204] D. Mandrus, A. Migliori, T. W. Darling, M. F. Hundley, E. J. Peterson, and J. D. Thompson, "Electronic transport in lightly doped $CoSb_3$," *Phys. Rev. B*, vol. 52, no. 7, p. 4926, 1995.

[205] Y. Kajikawa, "Effects of impurity-band conduction on thermoelectric properties of lightly doped *p*-type $CoSb_3$," *J. Appl. Phys.*, vol. 116, no. 15, p. 153710, 2014.

[206] B. Khan, H. A. R. Aliabad, S. Jalali-Asadabadi, I. Khan, and I. Ahmad, "Electronic band structures of binary skutterudites," *J. Alloys Compd.*, vol. 647, pp. 364–369, 2015.

[207] C. Hu, X. Zeng, Y. Liu, M. Zhou, H. Zhao, T. M. Tritt, J. He, J. Jakowski, P. R. Kent, J. Huang, *et al.*, "Effects of partial La filling and Sb vacancy defects on $CoSb_3$ skutterudites," *Phys. Rev. B*, vol. 95, no. 16, p. 165204, 2017.

[208] P. Shahi, D. J. Singh, J. P. Sun, L. X. Zhao, G. F. Chen, Y. Y. Lv, J. Li, J.-Q. Yan, D. G. Mandrus, and J.-G. Cheng, "Bipolar Conduction as the Possible Origin of the Electronic Transition in Pentatellurides: Metallic vs Semiconducting Behavior," *Phys. Rev. X*, vol. 8, p. 021055, 2018.

[209] P. Li, C. H. Zhang, J. W. Zhang, Y. Wen, and X. X. Zhang, "Giant planar Hall effect in the Dirac semimetal $ZrTe_{5-\delta}$," *Phys. Rev. B*, vol. 98, p. 121108(R), 2018.

[210] M. Inamo, "^{125}Te NMR Evidence for the Existence of Trinuclear Tellurate Ion in Aqueous Solution," *Chem. Lett.*, vol. 25, pp. 17–18, 1996.

[211] H. Fjellvåg and A. Kjekshus, "Structural properties of $ZrTe_5$ and $HfTe_5$ as seen by powder diffraction," *Solid State Commun.*, vol. 60, pp. 91–93, 1986.

[212] A. A. Sirusi, S. Ballikaya, J.-H. Chen, C. Uher, and J. H. Ross Jr., "Band Ordering and Dynamics of $Cu_{2-x}Te$ and $Cu_{1.98}Ag_{0.2}Te$," *J. Phys. Chem. C*, vol. 120, pp. 14549–14555, 2016.

[213] Z. Okvátovity, F. Simon, and B. Dóra, "Anomalous hyperfine coupling and nuclear magnetic relaxation in Weyl semimetals," *Phys. Rev. B*, vol. 94, p. 245141, 2016.

[214] H. Maebashi, T. Hirosawa, M. Ogata, and H. Fukuyama, "Nuclear magnetic relaxation and Knight shift due to orbital interaction in Dirac electron systems," *J. Phys. Chem. Solids*, vol. 128, pp. 138–143, 2019.

[215] S. A. Miller, I. Witting, U. Aydemir, L. Peng, A. J. E. Rettie, P. Gorai, D. Y. Chung, M. G. Kanatzidis, M. Grayson, V. Stevanović, *et al.*, "Polycrystalline $ZrTe_5$ Parametrized as a Narrow-Band-Gap Semiconductor for Thermoelectric Performance," *Phys. Rev. Appl.*, vol. 9, p. 014025, 2018.

[216] H. Chi, C. Zhang, G. Gu, D. E. Kharzeev, X. Dai, and Q. Li, "Lifshitz transition mediated electronic transport anomaly in bulk $ZrTe_5$," *New J. Phys.*, vol. 19, p. 015005, 2017.

[217] X. Yuan, C. Zhang, Y. Liu, A. Narayan, C. Song, S. Shen, X. Sui, J. Xu, H. Yu, Z. An, *et al.*, "Observation of quasi-two-dimensional Dirac fermions in $ZrTe_5$," *NPG Asia Mater.*, vol. 8, p. e325, 2016.

[218] L. Fu, C. L. Kane, and E. J. Mele, "Topological insulators in three dimensions," *Phys. Rev. Lett.*, vol. 98, p. 106803, 2007.

[219] S. Boutin, J. Ramírez-Ruiz, and I. Garate, "Tight-binding theory of NMR shifts in topological insulators Bi_2Se_3 and Bi_2Te_3," *Phys. Rev. B*, vol. 94, p. 115204, 2016.

[220] Y. Tian, N. Ghassemi, and J. H. Ross, Jr., "Topological nodal line in $ZrTe_2$ demonstrated by nuclear magnetic resonance," *Phys. Rev. B*, vol. 102, p. 165149, 2020.

[221] G. K. H. Madsen, P. Blaha, K. Schwarz, E. Sjöstedt, and L. Nordström, "Efficient linearization of the augmented plane-wave method," *Phys. Rev. B*, vol. 64, p. 195134, 2001.

[222] H. J. Monkhorst and J. D. Pack, "Special points for Brillouin-zone integrations," *Phys. Rev. B*, vol. 13, p. 5188, 1976.

[223] I. Orion, J. Rocha, S. Jobic, V. Abadie, R. Brec, C. Fernandez, and J.-P. Amoureux, "Solid-state tellurium-125 nuclear magnetic resonance studies of transition-metal ditellurides," *Dalton Trans.*, vol. 20, pp. 3741–3748, 1997.

[224] H. Wang, C. H. Chan, C. H. Suen, S. P. Lau, and J.-Y. Dai, "Magnetotransport Properties of Layered Topological Material $ZrTe_2$ Thin Film," *ACS Nano*, vol. 13, pp. 6008–6016, 2019.

[225] T. Cheiwchanchamnangij and W. R. Lambrecht, "Quasiparticle band structure calculation of monolayer, bilayer, and bulk MoS_2," *Phys. Rev. B*, vol. 85, p. 205302, 2012.

[226] N. A. Pike, A. Dewandre, B. Van Troeye, X. Gonze, and M. J. Verstraete, "Vibrational and dielectric properties of the bulk transition metal dichalcogenides," *Phys. Rev. Mater.*, vol. 2, p. 063608, 2018.

[227] B. Dóra and F. Simon, "Unusual hyperfine interaction of Dirac electrons and NMR spectroscopy in graphene," *Phys. Rev. Lett.*, vol. 102, p. 197602, 2009.

[228] Z. Li, L. Chen, S. Meng, L. Guo, J. Huang, Y. Liu, W. Wang, and X. Chen, "Field and temperature dependence of intrinsic diamagnetism in graphene: Theory and experiment," *Phys. Rev. B*, vol. 91, p. 094429, 2015.

[229] G. P. Mikitik and Y. V. Sharlai, "Crossing points of nodal lines in topological semimetals and the Fermi surface of ZrSiS," *Phys. Rev. B*, vol. 101, p. 205111, 2020.

[230] S. Xu, C. Bao, P.-J. Guo, Y.-Y. Wang, Q.-H. Yu, L.-L. Sun, Y. Su, K. Liu, Z.-Y. Lu, S. Zhou, *et al.*, "Interlayer quantum transport in Dirac semimetal $BaGa_2$," *Nat. Commun.*, vol. 11, pp. 1–8, 2020.

[231] S. Jeon, B. B. Zhou, A. Gyenis, B. E. Feldman, I. Kimchi, A. C. Potter, Q. D. Gibson, R. J. Cava, A. Vishwanath, and A. Yazdani, "Landau quantization and quasiparticle interference in the three-dimensional Dirac semimetal Cd_3As_2," *Nat. Mater.*, vol. 13, pp. 851–856, 2014.

[232] Y.-S. Fu, T. Hanaguri, K. Igarashi, M. Kawamura, M. S. Bahramy, and T. Sasagawa, "Observation of Zeeman effect in topological surface state with distinct material dependence," *Nat. Commun.*, vol. 7, pp. 1–6, 2016.

[233] Y. Liu, X. Yuan, C. Zhang, Z. Jin, A. Narayan, C. Luo, Z. Chen, L. Yang, J. Zou, X. Wu, *et al.*, "Zeeman splitting and dynamical mass generation in Dirac semimetal $ZrTe_5$," *Nat. Commun.*, vol. 7, pp. 1–9, 2016.

[234] J. Hu, Z. Tang, J. Liu, Y. Zhu, J. Wei, and Z. Mao, "Nearly massless Dirac fermions and strong Zeeman splitting in the nodal-line semimetal ZrSiS probed by de Haas-van Alphen quantum oscillations," *Phys. Rev. B*, vol. 96, p. 045127, 2017.

[235] P. Lee and N. Nagaosa, "Relaxation of nuclear spin due to long-range orbital currents," *Phys. Rev. B*, vol. 43, p. 1223, 1991.

[236] J. Yang, G. P. Meisner, D. T. Morelli, and C. Uher, "Iron valence in skutterudites: transport and magnetic properties of $Co_{1-x}Fe_xSb_3$," *Phys. Rev. B*, vol. 63, no. 1, p. 014410, 2000.

[237] Y. Chen, Y. Kawamura, J. Hayashi, K. Takeda, and C. Sekine, "The structural, transport, and magnetic properties of Yb-filled skutterudites $Yb_yFe_xCo_{4-x}Sb_{12}$ synthesized under high pressure," *J. Appl. Phys.*, vol. 120, no. 23, p. 235105, 2016.

[238] H. Li, C. Y. Wu, and J. C. Ho, "Calorimetric study of the antiferromagnetic transition in ytterbium sesquioxide," *Phys. Rev. B*, vol. 49, no. 2, p. 1447, 1994.

[239] D. J. Garcia, F. A. Garcia, J. G. S. Duque, P. G. Pagliuso, C. Rettori, P. Schlottmann, M. S. Torikachvili, and S. B. Oseroff, "Direct determination of the crystal field parameters of Dy, Er, and Yb impurities in the skutterudite compound $CeFe_4P_{12}$ by electron spin resonance," *Phys. Rev. B*, vol. 78, no. 17, p. 174428, 2008.

APPENDIX A

STRETCHED-EXPONENTIAL SPIN-LATTICE RELAXATION ANALYSIS

This work includes an analysis of the stretched-exponential NMR T_1 behavior due to paramagnetic impurities combined with a single-exponential relaxation process. A full description of this analysis procedure is as follows:

Tse and Hartmann [129] originally demonstrated that dilute paramagnetic impurities could produce a relaxation function of the form $S(t) = S_0 \exp[-(t/\tau_1)^{1/2}]$, a result which is valid in the long-time limit. This behavior is due to an inhomogeneous distribution of fluctuating fields due to random positioning of paramagnetic defects. A given nucleus thus undergoes statistical behavior corresponding locally to ordinary exponential relaxation. This superposition of nuclear responses can be written,

$$S(t) = S_0 \exp[-(t/\tau_1)^{1/2}] = S_0 \sum_i c_i \exp[-t/(T_{1s})_i], \tag{A.1}$$

where the c_i are a set of weighting factors corresponding to the distribution of exponential relaxation times $(T_{1s})_i$, and the summation in Eq. (A.1). represents a discrete approximation to the continuous inhomogeneous distribution.

We examine the situation where this is combined with a second uniform relaxation process due to metallic electrons, which alone would produce a relaxation function $S(t) = S_0 \exp[-(t/T_{1,\exp})]$. Since for locally exponential processes the rates will add, we obtain the combined relaxation function,

$$S(t) = S_0 \exp[-(t/T_{1,\exp})] \sum_i c_i \exp[-t/(T_{1s})_i]. \tag{A.2}$$

To obtain the parameters for the summation in Eq. (A.1), we chose seven $(T_{1s})_i$ values which were initially logarithmically distributed over 4 orders of magnitude, and fitted to the stretched exponential $\exp[-(t/\tau_1)^{1/2}]$ by performed a least squares minimization of the parameters $(T_{1s})_i$ and c_i, the result being a sum of exponentials with single effective parameter τ_1 which could be

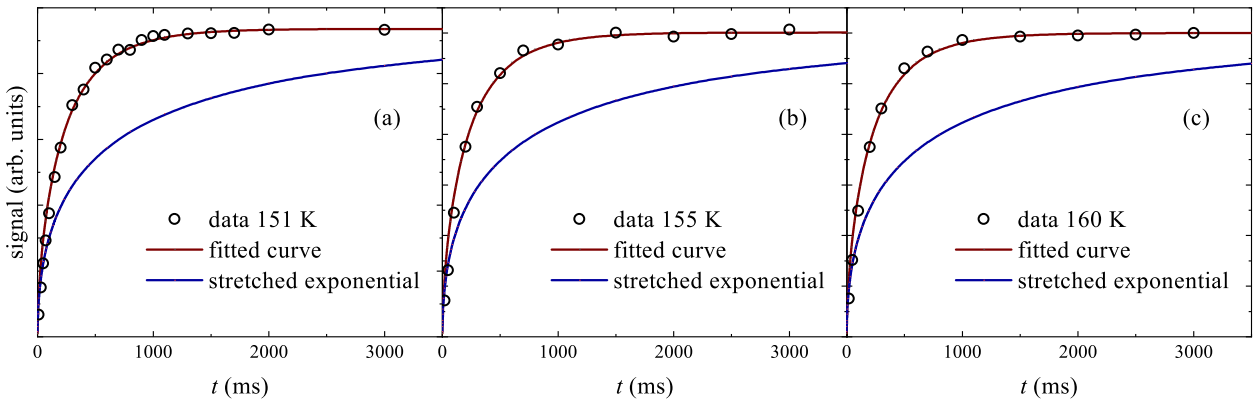

Figure A.1: Saturation-recovery plots for three temperatures, (a) 151 K, (b) 155 K, and (c) 160 K, with fitted curves described in text. Stretched exponentials alone (fitted curves with $\exp[-(t/T_{1,\mathrm{exp}})]$ removed) are also shown for comparison.

varied by scaling all $(T_{1s})_i$ values by an identical factor.

Results of the fitting process are shown in Fig. A.1, for the three temperatures near the observed relaxation peak. As explained in the main text, we obtained τ_1 from the paramagnetic impurity density and moment determined in this work, using Eq. 4.3 in Chapter 4, which contains the function $[\omega\tau_c/(1+\omega^2\tau_c^2)]^{1/2} \equiv F(\omega,\tau_c)$, containing τ_c which is the spin-lattice relaxation time for the local moment. Since the temperature dependence of τ_c is not known, $F(\omega,\tau_c)$ cannot be in general be evaluated except at its maximum point $(\omega = \tau_c^{-1})$ where $F(\omega,\tau_c) = 2^{-1/2}$. Therefore, the fitting process was carried out for temperatures only at the apparent peak of the exponential-fitted NMR relaxation rate *vs* temperature. With τ_1 fixed the fitting to $[S_0 - S(t)]$ involved two parameters, S_0 and $T_{1,\mathrm{exp}}$, for each temperature. Since the stretched-exponential recovery function is not valid at very short times during the initial recovery process, the fitting was limited for these curves to $t \geq 200$ ms, for which $S(t)/S_0 < 0.5$.

APPENDIX B

MAGNETIC MEASUREMENTS OF SKUTTERUDITES

The DC susceptibility as a function of temperature, $\chi(T)$, was obtained at a fixed magnetic field of 1000 Oe using a Quantum Design SQUID magnetometer. The data from 2 K to 300 K for samples Ba(0.1)Yb(0.2) and Ba(0.2) is shown in Figs. B.1a and B.1b.

It has been shown previously that pure skutterudite $CoSb_3$ is diamagnetic [49, 236], therefore the magnetization can be analyzed in terms of paramagnetic filler atoms or defects in a diamagnetic host. For the case of Yb filler atoms, recent work [237] reveals that Yb atoms exist in the $4f^{13}$ state (Yb^{3+}) in concentrated $Yb_xCo_4Sb_{12}$, for x as large as 0.2, and exhibit paramagnetic behavior with no ordering detected down to helium temperature.

We thus fit the high-T Ba(0.1)Yb(0.2) data from 150 K to 300 K to a Curie-Weiss function according to the standard relationship,

$$\chi(T) = \frac{C_{\rm CW}}{T + \Theta_{\rm CW}} + \chi_0, \tag{B.1}$$

with fitting results $C_{\rm CW} = 0.427$ K emu mol^{-1}, $\Theta_{\rm CW} = 45$ K and $\chi_0 = -2.4 \times 10^{-4}$ emu mol^{-1}, calibrated per mole of $Ba_xYb_yCo_4Sb_{12}$ formula units. The Curie constant can also be defined by

$$C_{\rm CW} = N_A c \frac{p_{\rm eff}^2 \mu_B^2}{3k_B}, \tag{B.2}$$

where N_A is Avogadro constant, c is the concentration of magnetic ions per formula unit and $p_{\rm eff}$ is the effective moment. Assuming the paramagnetic response to be due to Yb^{3+} ions, and using the known theoretical effective moment $p_{\rm eff} = g\sqrt{J(J+1)} = 4.54\,\mu_B$ with $g = 8/7$ and $J = 7/2$, the corresponding paramagnetic defect concentration is $c = 0.164$ per formula unit. This is larger than the fitted $x = 0.067$ measured Yb filler-atom concentration, with the difference likely due to the combined influence of paramagnetic shallow defect states as well as Yb_2O_3 due to a

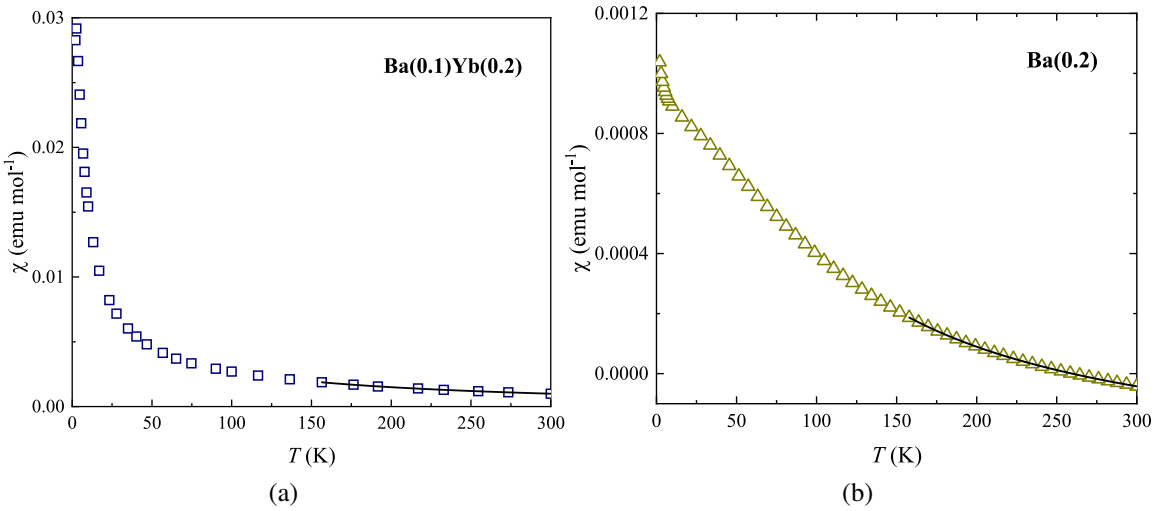

Figure B.1: DC susceptibility measured from 2 K to 300 K in a magnetic field of 1000 Oe for (a) Ba(0.1)Yb(0.2) and (b) Ba(0.2). Symbols: measured data. Solid curves: Curie-Weiss fits.

portion of the unreacted Yb source material remaining in the sample [41]. The presence of this small secondary phase is indicated by the small maximum found near 2.3 K which is the known antiferromagnetic transition temperature of Yb_2O_3 [238]. This separate phase will have very little influence on the ^{59}Co NMR results. Note also that the fitted $\Theta_{\rm CW}$ at high temperature includes typically a significant contribution due to crystal fields experienced by the Yb^{3+} ions [239].

Fig. B.1b shows that there is a smaller magnetic contribution in sample Ba(0.2). We can also fit the high-T data from 150 K to 300 K to a Curie-Weiss law [Eq. (B.1)] with $C_{\rm CW} = 0.091$ K emu mol^{-1}, $\Theta_{\rm CW} = 31$ K and $\chi_0 = -3.2 \times 10^{-4}$ emu mol^{-1}. Assuming the paramagnetic defects have spin 1/2, Eq. (B.2) leads to a paramagnetic defect concentration $\sim$0.22 per formula unit. This can be attributed to the shallow defect states as discussed in the main text. As a volume density this defect concentration would correspond to a shallow defect concentration $\sim 5.8 \times 10^{20}$ cm^{-3}, which is in good agreement with the density of occupied shallow defects ($n_D = N_D - n_{\rm CB}$) obtained in the analysis. The small upturn at low temperature could be due to a small amount of surface states or other impurity states. The background diamagnetism is consistent with the range [49] of -1.6×10^{-4} to -3.6×10^{-4} emu/mol found for $CoSb_3$ single crystals with various

carrier concentrations.

APPENDIX C

SPIN-LATTICE RELAXATION DUE TO ORBITAL AND DIPOLAR INTERACTIONS

The local orbital contribution to $1/T_1T$ is the mechanism typically associated with orbital hyperfine coupling in normal metals. As opposed to the extended-orbital mechanism [156, 235], the local contribution is expected to be limited to orbitals belonging to the atom containing the nucleus being measured. Following the treatment of Obata [155], here we extend the calculation of $1/T_1T$ to *p*-electrons in the tetragonal symmetry corresponding to the 3-fold uniaxial symmetry for Te sites in $ZrTe_2$ (Chapter 9).

In the tight-binding approximation, the Bloch eigenfunctions are built up from localized atomic functions. For *p*-electrons, there are three independent orbital functions p_x, p_y and p_z. With magnetic field B along a certain direction, in our case x and z, here are the mixed wavefunctions for uniaxial symmetry (omitting the product spin states):

$$\Psi = \begin{cases} \alpha^{1/2} p_z + (1-\alpha)^{1/2} \dfrac{1}{\sqrt{2}}(p_x + p_y), & B \parallel c \\ \alpha^{1/2} p_y + (1-\alpha)^{1/2} \dfrac{1}{\sqrt{2}}(p_z + p_x), & B \perp c \end{cases} \tag{C.1}$$

where α is a parameter specifying the relative amount of E symmetry (p_x and p_y) *vs* A_1 symmetry (p_z) for magnetic field along z (similarly for $B \perp c$ with Ψ rotating correspondingly). For $B \parallel c$, when $\alpha = 0$, the wavefunction contains only p_x and p_y. With $\alpha = 1$, only p_z remains. For both dipolar interaction and orbital interaction contributions, we can thus determine the expressions of the corresponding spin-lattice relaxation rates, starting with a golden-rule relation, for which $1/T_1 = 2W = 4\pi/\hbar k_B T \langle|\Psi|\mathcal{H}|\Psi\rangle|^2 g^2(\varepsilon_F)$, where $\mathcal{H}$ is the orbital or dipolar hyperfine interaction Hamiltonian [155], both of which are proportional to $1/r^3$ allowing the relative magnitudes to be readily compared. Also $g(\varepsilon_F)$ denotes the partial density of states at ε_F for the Te *p*-orbitals, which are assumed to appear in the relevant band according to the amplitudes given in Eq. (C.1).

We obtain the following for the case for dipolar interaction:

$$\begin{aligned} W_{\rm dip} =& \frac{4\pi}{5} C \Bigg(\left| \int_0^{2\pi} \int_0^{\pi} \Psi\Psi^* \frac{1}{2} Y_2^0 \sin\theta d\theta d\phi \right|^2 + \left| \int_0^{2\pi} \int_0^{\pi} \Psi\Psi^* \frac{\sqrt{3}}{2} Y_2^{-1} \sin\theta d\theta d\phi \right|^2 \\ & + \left| \int_0^{2\pi} \int_0^{\pi} \Psi\Psi^* \sqrt{\frac{3}{2}} Y_2^{-2} \sin\theta d\theta d\phi \right|^2 \Bigg) \\ =& \begin{cases} \dfrac{C}{50}(9\alpha^2 - 12\alpha + 5) & (B \parallel c) \\ \dfrac{C}{200}(9\alpha^2 + 6\alpha + 5) & (B \perp c), \end{cases} \end{aligned} \tag{C.2}$$

where Ψ is the wavefunction from Eq. (C.1). Here $C = 2\pi(\gamma_e\gamma_n\hbar^{3/2})^2 g^2(\varepsilon_F) k_B T \langle r^{-3}\rangle^2$, where $\langle r^{-3}\rangle$ comes from the radial parts of the integrations which are not displayed in Eq. (C.2). The integrals can be analytically evaluated giving the results also shown in Eq. (C.2). For the case of the orbital interaction, the corresponding relations are

$$W_{\rm orb} = \frac{C}{2} |\langle\Psi| l^{-1} |\Psi\rangle|^2 = \begin{cases} 2C\alpha(1-\alpha) & (B \parallel c) \\ \dfrac{C}{2}(1-\alpha^2) & (B \perp c). \end{cases} \tag{C.3}$$

These results are shown in Fig. 9.5(c) in the main text. As anticipated [155] the orbital term dominates in almost all cases. Also there is a crossing of terms at $\alpha = 1/3$ which represents an equal mixture of orbitals, as expected since such a mixture becomes isotropic. When α is larger than 1/3, the local orbital contribution for $B \parallel c$ exceeds that for $B \perp c$.